

MEASURING EVAPORATION RATE CONSTANTS OF HIGHLY VOLATILE
COMPOUNDS AND INVESTIGATING THE EFFECT OF INTERFACE ON A KINETIC
MODEL APPLIED TO FORENSIC FIRE DEBRIS

By

Amanda L. Burkhart

A DISSERTATION

Submitted to
Michigan State University
in partial fulfillment of the requirements
for the degree of

Chemistry – Doctor of Philosophy

2021

ABSTRACT

MEASURING EVAPORATION RATE CONSTANTS OF HIGHLY VOLATILE COMPOUNDS AND INVESTIGATING THE EFFECT OF INTERFACE ON A KINETIC MODEL APPLIED TO FORENSIC FIRE DEBRIS

By

Amanda L. Burkhart

A kinetic model was previously developed in our laboratory to predict evaporation of compounds as a function of gas chromatographic retention index (I^T). Evaporation rate constants were experimentally determined for compounds in the range $I^T = 800 - 1400$ to define the initial model. While the predictive accuracy was demonstrated, broader application of the model, especially for forensic fire debris applications, requires extension of the I^T range to include more volatile compounds. However, such extension requires experimental determination of rate constants, which is challenging due to the explosive hazard and rapid evaporation of volatile compounds.

In this work, rate constants of highly volatile compounds were experimentally determined and used to extend the kinetic model to predict evaporation. Prior to experimental evaporations, theoretical calculations were performed to optimize experimental parameters and to ensure that the vapor generated remained below the lower flammability limit for each compound. Compounds were then experimentally evaporated at three different temperatures (10, 20, and 30 °C) and analyzed by gas chromatography-mass spectrometry. The evaporation rate constants for each compound, corrected for condensation, were determined by regression to a first-order rate equation. These rate constants were combined with previously collected data to extend the kinetic model at each temperature. Comparison of predicted and experimentally determined chromatograms of an evaporated validation mixture indicated good model performance, with

correlation coefficients ranging from 0.955 – 0.997 and mean absolute percent errors in predicting abundance ranging from 0 – 35%.

The kinetic model was originally developed by measuring rate constants of compounds evaporating from water, due to the environmental applications. For the refinement of the model using volatile compounds, evaporations were conducted directly from the surface of a glass dish. In addition to these two substrates, many more surfaces are present in a setting where an intentional fire may originate. The second study presented here investigated the effect of interface on the evaporation rate constants of compounds commonly found in ignitable liquids. Compounds from three homologous series (normal alkanes, alkylbenzenes, and alkyl cyclohexanes) were evaporated from a glass dish, water, cotton fabric, and polyester fabric.

Rate constants were determined for the experimental evaporation of these compounds from each interface and class- and substrate-specific models were developed. For all compounds, evaporation was slowest from the glass dish compared to the other substrates, indicating a difference in the chemical interactions between the hydrocarbons and interface or a physical difference, such as porosity or spreading of the liquid. For the remaining three interfaces, rate constants for each compound were similar, although the kinetics were consistently slower from the polyester fabric compared to the cotton fabric. Overall, the models were comparable to both each other as well as the original class-specific models suggesting an applicability of the model across several different substrates without the need for further refinement.

ACKNOWLEDGMENTS

I would like to first thank my advisor, Dr. Ruth Smith for guidance and continuous support. Without her, I would not have been able to continue on after completing my master's degree to pursue a Ph.D. She always believed in me and has inspired me to become an educator so that I can have the same impact on future students that she had on me. I would also like to thank Dr. Victoria McGuffin who served as almost a second advisor to me. She has provided knowledge, expertise, and encouraging words over the years and has pushed me to be a better scientist. Finally, I would like to acknowledge Dr. Gary Blanchard and Dr. Greg Swain for serving on my committee and challenging me to ask the tough questions.

In addition to the personal support that I received on this project, I would also like to acknowledge the National Institute of Justice for supporting this research through grant number 2018-DU-BX-0225. The points of view in this dissertation are those of the author and do not necessarily represent the official position or policies of the U.S. Department of Justice.

Outside of the academic support I have had through the years, I have also had an outpouring of love and support from my friends, family, and research group. A special thank you to Briana Capistran who was always there to help with experiments and challenge me intellectually. I would also not have gotten through graduate school without all of the moral support from my present and past group members, including Hannah Clause, Otyllia Abraham, Amber Gerheart, Isaac Willis, Andrew Wendel, Andrew Sacha, William Shirley, and Julia Angst.

Last, but certainly not least, I would like to extend a huge thank you to my family. My husband, Todd Burkhart, listened to my practices, complaints, and stresses over the years and

always knew what to say to make things feel more manageable. Graduate school became a lot easier when Todd's family became my home away from home in East Lansing. Special thanks to Beverly Stephens and Mark and Sandra Burkhart for the support over the last few years. Finally, I cannot put into the words the gratitude I have for my parents, Jeff and Theresa Setser, and my sister and brother-in-law, Olivia and Joseph Meyer. Even before I moved to Michigan, you all instilled in me the faith that I could do anything that I set my mind to. Every time I doubted myself, it was the love and support of family that kept me going and I will forever be trying to make you proud.

TABLE OF CONTENTS

LIST OF TABLES	viii
LIST OF FIGURES	xii
I. Introduction	1
1.1 Forensic Fire Debris Analysis	1
1.2 Theory of Evaporation	4
1.3 Modeling Evaporation using Vapor Pressure.....	5
1.4 Kinetic Model based on Gas Chromatographic Retention Index.....	7
1.4.1 Development of a Variable-Temperature Model.....	13
1.5 Effect of Interface on Evaporation	15
1.6 Objectives and Aims	19
REFERENCES	22
II. Theoretical Calculations of Vapor Load	26
2.1 Introduction	26
2.2 Theoretical Calculations of Vapor Load for Normal Alkanes	27
2.3 Theoretical Calculations of Vapor Load for Selected Volatile Compounds.....	34
2.4 Conclusions	37
APPENDIX.....	38
REFERENCES	49
III. Measuring Evaporation Rate Constants of Highly Volatile Compounds for Kinetic Models	51
3.1 Introduction	51
3.2 Materials and Methods	52
3.2.1 Standard Preparation.....	52
3.2.2 Experimental Evaporations.....	53
3.2.3 Gas Chromatography-Mass Spectrometry Analysis.....	54
3.2.4 Retention Index Calculations.....	55
3.2.5 Data Analysis.....	55
3.3 Results	57
3.3.1 Refinement and Validation of the Fixed-Temperature Model at 10 °C	57
3.3.2 Correcting Rate Constants for Condensation	69
3.3.3 Refinement and Validation of the Fixed-Temperature Models at 20 and 30 °C.....	77
3.3.4 Comparison to the Original Fixed-Temperature Kinetic Models.....	82
3.3.5 Refinement and Validation of the Variable-Temperature Model.....	89
3.4 Conclusions	91
APPENDIX.....	94
REFERENCES	107
IV. Effect of Interface Chemistry on the Evaporation Rate Constants of Different Compound Classes in Diesel Fuel	109
4.1 Introduction	109

4.2 Materials and Methods	112
4.2.1 Sample Collection.....	112
4.2.2 Attenuated Total Reflectance-Fourier Transform Infrared (ATR-FTIR) Spectroscopy	112
4.2.3 Experimental Evaporation	113
4.2.4 Gas Chromatography-Mass Spectrometry Analysis.....	114
4.2.5 Data Analysis.....	114
4.3 Results	115
4.3.1 ATR-FTIR Spectroscopy.....	115
4.3.2 Development of Substrate-Specific Models based on n-Alkanes	117
4.3.3 Development of Substrate-Specific Models based on Alkylbenzenes	123
4.3.4 Development of Substrate-Specific Models based on Alkyl Cyclohexanes	128
4.4 Conclusions	134
APPENDIX.....	135
REFERENCES	137
V. Conclusions and Future Work.....	139
5.1 Conclusions	139
5.2 Future Work	141
REFERENCES	143

LIST OF TABLES

Table 1.1. ASTM Classification of Ignitable Liquids [7].....	2
Table 2.1. Maximum Calculated Vapor Load for <i>n</i> -Alkanes	33
Table A2.1: Maximum vapor load (% v/v) and time of occurrence predicted for <i>n</i> -butane as a function of temperature, flow rate, volume, and number of dishes.	39
Table A2.2. Maximum vapor load (% v/v) and time of occurrence predicted for <i>n</i> -pentane as a function of temperature, flow rate, volume, and number of dishes.	41
Table A2.3. Maximum vapor load (% v/v) and time of occurrence predicted for <i>n</i> -hexane as a function of temperature, flow rate, volume, and number of dishes.	43
Table A2.4. Maximum vapor load (% v/v) and time of occurrence predicted for <i>n</i> -heptane as a function of temperature, flow rate, volume, and number of dishes.	45
Table A2.5. Maximum vapor load (% v/v) and time of occurrence predicted for <i>n</i> -octane as a function of temperature, flow rate, volume, and number of dishes.	47
Table 3.1. Evaporation Rate Constants for Selected Compounds at 10 °C	61
Table 3.2. Error in Prediction of Chromatograms for Refined Model at 10 °C	65
Table 3.3. Predictive Accuracy of the Refined Model at 10 °C for Individual Compounds in the Validation Mixture.....	68
Table 3.4. Comparison of Uncorrected and Corrected Evaporation Rate Constants for Compounds at 10 °C	73
Table 3.5. Comparison of Uncorrected and Corrected Models for Error in Prediction of Chromatograms at 10 °C.....	74
Table 3.6. Predictive Accuracy of the Corrected Model at 10 °C for Individual Compounds in the Validation Mixture.....	77
Table 3.7. Corrected Evaporation Rate Constants for the Fixed Temperature Models at 20 and 30 °C	78
Table 3.8. Predictive Accuracy of the Corrected Models at 20 and 30 °C	80
Table 3.9. Predictive Accuracy of the Corrected Model at 20 °C for Individual Compounds in the Validation Mixture.....	81

Table 3.10. Predictive Accuracy of the Corrected Model at 30 °C for Individual Compounds in the Validation Mixture.....	82
Table 3.11. Comparison of the Original Model to the Refined Corrected Model at 10 °C.....	83
Table 3.12. Comparison of the Predicted Accuracy of the Original Model <i>versus</i> the Refined Corrected Model at 10 °C with $F_{Total} = 0.54$	83
Table 3.13. Comparison of the Predicted Accuracy of the Original Model <i>versus</i> the Refined Corrected Model at 10 °C with $F_{Total} = 0.65$	83
Table 3.14. Comparison of the Predicted Accuracy of the Original Model <i>versus</i> the Refined Corrected Model at 10 °C with $F_{Total} = 0.82$	84
Table 3.15. Comparison of the Original Model to the Refined Corrected Model at 20 °C.....	86
Table 3.16. Comparison of the Original Model to the Refined Corrected Model at 30 °C.....	88
Table 3.17. Comparison of the Original Variable-Temperature Model to the Refined Corrected Model at 10 °C.....	90
Table 3.18. Comparison of the Original Variable-Temperature Model to the Refined Corrected Model at 20 °C.....	90
Table 3.19. Comparison of the Original Variable-Temperature Model to the Refined Corrected Model at 30 °C.....	90
Table A3.1. Comparison of the Predicted Accuracy of the Original Model <i>versus</i> the Refined Corrected Model at 20 °C with $F_{Total} = 0.36$	95
Table A3.2. Comparison of the Predicted Accuracy of the Original Model <i>versus</i> the Refined Corrected Model at 20 °C with $F_{Total} = 0.42$	95
Table A3.3. Comparison of the Predicted Accuracy of the Original Model <i>versus</i> the Refined Corrected Model at 20 °C with $F_{Total} = 0.53$	96
Table A3.4. Comparison of the Predicted Accuracy of the Original Model <i>versus</i> the Refined Corrected Model at 20 °C with $F_{Total} = 0.66$	96
Table A3.5. Comparison of the Predicted Accuracy of the Original Model <i>versus</i> the Refined Corrected Model at 20 °C with $F_{Total} = 0.81$	97
Table A3.6. Comparison of the Predicted Accuracy of the Original Model <i>versus</i> the Refined Corrected Model at 30 °C with $F_{Total} = 0.25$	97

Table A3.7. Comparison of the Predicted Accuracy of the Original Model <i>versus</i> the Refined Corrected Model at 30 °C with $F_{Total} = 0.36$	98
Table A3.8. Comparison of the Predicted Accuracy of the Original Model <i>versus</i> the Refined Corrected Model at 30 °C with $F_{Total} = 0.55$	98
Table A3.9. Comparison of the Predicted Accuracy of the Original Model <i>versus</i> the Refined Corrected Model at 30 °C with $F_{Total} = 0.69$	99
Table A3.10. Comparison of the Predicted Accuracy of the Original Model <i>versus</i> the Refined Corrected Model at 30 °C with $F_{Total} = 0.83$	99
Table A3.11. Comparison of the Predicted Accuracy of the Original Variable-Temperature Model <i>versus</i> the Refined Corrected Model at 10 °C with $F_{Total} = 0.54$	100
Table A3.12. Comparison of the Predicted Accuracy of the Original Variable-Temperature Model <i>versus</i> the Refined Corrected Model at 10 °C with $F_{Total} = 0.65$	100
Table A3.13. Comparison of the Predicted Accuracy of the Original Variable-Temperature Model <i>versus</i> the Refined Corrected Model at 10 °C with $F_{Total} = 0.82$	101
Table A3.14. Comparison of the Predicted Accuracy of the Original Variable-Temperature Model <i>versus</i> the Refined Corrected Model at 20 °C with $F_{Total} = 0.36$	101
Table A3.15. Comparison of the Predicted Accuracy of the Original Variable-Temperature Model <i>versus</i> the Refined Corrected Model at 20 °C with $F_{Total} = 0.42$	102
Table A3.16. Comparison of the Predicted Accuracy of the Original Variable-Temperature Model <i>versus</i> the Refined Corrected Model at 20 °C with $F_{Total} = 0.53$	102
Table A3.17. Comparison of the Predicted Accuracy of the Original Variable-Temperature Model <i>versus</i> the Refined Corrected Model at 20 °C with $F_{Total} = 0.66$	103
Table A3.18. Comparison of the Predicted Accuracy of the Original Variable-Temperature Model <i>versus</i> the Refined Corrected Model at 20 °C with $F_{Total} = 0.81$	103
Table A3.19. Comparison of the Predicted Accuracy of the Original Variable-Temperature Model <i>versus</i> the Refined Corrected Model at 30 °C with $F_{Total} = 0.25$	104
Table A3.20. Comparison of the Predicted Accuracy of the Original Variable-Temperature Model <i>versus</i> the Refined Corrected Model at 30 °C with $F_{Total} = 0.36$	104
Table A3.21. Comparison of the Predicted Accuracy of the Original Variable-Temperature Model <i>versus</i> the Refined Corrected Model at 30 °C with $F_{Total} = 0.55$	105

Table A3.22. Comparison of the Predicted Accuracy of the Original Variable-Temperature Model <i>versus</i> the Refined Corrected Model at 30 °C with $F_{Total} = 0.69$	105
Table A3.23. Comparison of the Predicted Accuracy of the Original Variable-Temperature Model <i>versus</i> the Refined Corrected Model at 30 °C with $F_{Total} = 0.83$	106
Table 4.1. Comparison of the Evaporation Rate Constants of the Normal Alkanes from Various Interfaces at 20 °C	119
Table 4.2. Comparison of the Linear Regression Models for each Interface for the <i>n</i> -Alkanes at 20°C. For each model, the slope (<i>m</i>), intercept (<i>b</i>), and coefficient of determination (R^2) are shown.	122
Table 4.3. Comparison of the Evaporation Rate Constants of the Alkylbenzenes from Various Interfaces at 20 °C	125
Table 4.4. Comparison of the Linear Regression Models for each Interface for the Alkylbenzenes at 20 °C. For each model, the slope (<i>m</i>), intercept (<i>b</i>), and coefficient of determination (R^2) are shown.	127
Table 4.5. Comparison of the Evaporation Rate Constants of the Alkyl Cyclohexanes from Various Interfaces at 20 °C	130
Table 4.6. Comparison of the Linear Regression Models for each Interface for the Alkyl Cyclohexanes at 20 °C. For each model, the slope (<i>m</i>), intercept (<i>b</i>), and coefficient of determination (R^2) are shown.....	133

LIST OF FIGURES

Figure 1.1. Total ion chromatogram for gasoline at (A) 0% evaporated (unevaporated), (B) 50% evaporated, (C) 75% evaporated, and (D) 89% evaporated by mass with characteristic peaks for heptane (1), toluene (2), octane (3), C ₂ -alkylbenzenes (4-6), and C ₃ -alkylbenzenes (7-13) [8]	3
Figure 1.2. Schematic of the evaporation chamber used by McIlroy <i>et al.</i> for experimental evaporations of diesel [21].....	8
Figure 1.3. Total ion chromatograms of diesel evaporated to 0, 7, 30, and 300 h and the resultant decay curve for octane where the rate constant (<i>k</i>) is represented in red [21]	9
Figure 1.4. Fraction remaining curves corresponding to a total fraction remaining of 0.7, 0.5, 0.3, and 0.1 [22]	11
Figure 1.5. Chromatogram of unevaporated torch fuel multiplied by a F_{Total} curve of 0.3 to yield a predicted chromatogram of 70% evaporated torch fuel [22].....	11
Figure 1.6. Chromatogram of gasoline in range I^T 400 – 800. Compounds identified as (1) methylbutane, (2) <i>n</i> -pentane, (3) methylbutene, (4) dichloroethylene, (5) methylpentane isomer, (6) methylpentane isomer, (7) <i>n</i> -hexane, (8) methylcyclopentane, (9) benzene, (10) cyclohexane, (11) dimethylpentane, (12) methylhexane, (13) cyclohexene, (14) dimethylcyclopentane, (15) tetramethylbutane, (16) <i>n</i> -heptane, and (17) toluene [23]	12
Figure 1.7. Chromatogram of unevaporated diesel (black) and diesel evaporated for 300 h at 5°C (purple), 10°C (blue), 20°C (green), 30°C (yellow), and 35°C (red) [24].....	13
Figure 2.1. Vapor load calculations for the normal alkanes at 40 °C with a volume of 0.10 mL shown in (A) mL, (B) % v/v, and (C) % v/v when incorporating flow rate (30 mL/min)	29
Figure 2.2. Theoretical vapor load for 12 compounds, calculated at 10 °C in (A) mL, (B) % v/v incorporating a flow rate of 60 mL/min, and (C) % v/v incorporating a flow rate of 60 mL/min and dish removal throughout evaporation.....	35
Figure 3.1. Normalized abundances of (A) <i>n</i> -pentane, (B) <i>n</i> -hexane, (C) <i>n</i> -heptane, and (D) <i>n</i> -octane as a function of evaporation time. Linear regression equations: <i>n</i> -pentane: $C_t = 0.155 * \exp(-4.602 * t)$, $R^2 = 0.8793$; <i>n</i> -hexane: $C_t = 0.354 * \exp(-1.674 * t)$, $R^2 = 0.9485$; <i>n</i> -heptane: $C_t = 0.389 * \exp(-0.323 * t)$, $R^2 = 0.9437$; <i>n</i> -octane: $C_t = 0.611 * \exp(-0.0861 * t)$, $R^2 = 0.9250$..	59
Figure 3.2. Natural logarithm of the evaporation rate constant (<i>k</i>) versus retention index (I^T) for previously collected data ($I^T = 800 - 1200$) [2] combined with rate constants for 12 additional volatile compounds ($I^T = 500 - 800$) at 10 °C. Linear regression equation: $y = -0.0112 x + 6.93$ ($R^2 = 0.9889$).....	63

Figure 3.3. Experimental (black) <i>versus</i> predicted (red) chromatograms using the refined model (Eq. 3.6) for the validation mixture evaporated to (A) $F_{Total} = 0.54$, (B) $F_{Total} = 0.65$, and (C) $F_{Total} = 0.82$ at 10 °C	66
Figure 3.4. (A) Uncorrected decay curve, (B) Reverse curve, and (C) Corrected decay curve for <i>n</i> -octane ($I^T = 800$). Regression equations: Uncorrected: $C_t = 0.611 * \exp(-0.0861 * t)$, $R^2 = 0.9250$, Corrected: $C_t = 0.585 * \exp(-0.172 * t)$, $R^2 = 0.9652$	71
Figure 3.5. Natural logarithm of the evaporation rate constant (k) <i>versus</i> retention index (I^T) for previously collected data ($I^T = 800 - 1200$) [2] combined with rate constants for 12 additional volatile compounds ($I^T = 500 - 800$) at 10 °C. Linear regression equations:	75
Uncorrected: $y = -0.0112 x + 6.93$ ($R^2 = 0.9889$), Corrected: $y = -0.0122 x + 8.07$ ($R^2 = 0.9844$).	75
Figure 3.6. Natural logarithm of the corrected evaporation rate constant (k) <i>versus</i> retention index (I^T) for 12 volatile compounds ($I^T = 500 - 800$) with previously collected data ($I^T = 800 - 1200$) [1,2] at 10, 20, and 30 °C.....	78
Figure 4.1. Predicted chemistry of the four interfaces under investigation: (A) silica structure at surface of glass petri dishes, (B) water, (C) cellulose present in cotton fabric, and (D) poly(ethylene terephthalate) structure of polyester fabric	110
Figure 4.2. ATR-FTIR spectrum for cotton fabric	116
Figure 4.3. ATR-FTIR spectrum for polyester fabric.....	116
Figure 4.4. Representative decay curves for <i>n</i> -decane from (A) glass dish, (B) water, (C) cotton fabric, and (D) polyester fabric at 20 °C	118
Figure 4.5. Interface-specific models for the <i>n</i> -alkanes at 20 °C. Linear regression shown in Table 4.2.	122
Figure 4.6. Representative decay curves for butylbenzene from (A) glass dish, (B) water, (C) cotton fabric, and (D) polyester fabric at 20 °C	124
Figure 4.7. Interface-specific models for the alkylbenzenes at 20 °C. Linear regression shown in Table 4.4.	127
Figure 4.8. Representative decay curves for butylcyclohexane from (A) glass dish, (B) water, (C) cotton fabric, and (D) polyester fabric at 20 °C	129
Figure 4.9. Interface-specific models for the alkyl cyclohexanes at 20 °C. Linear regression shown in Table 4.6.	133
Figure A4.1. Reference ATR-FTIR spectrum for cotton [8].....	136

Figure A4.2. Reference ATR-FTIR spectrum for poly(ethylene terephthalate) [8] 136

I. Introduction

1.1 Forensic Fire Debris Analysis

According to the 2018 report by the National Fire Protection Association, over 22,000 fire-related incidents were reported that caused 643 civilian deaths and over \$882 million in direct property damage [1]. Additionally, the Federal Bureau of Investigation's Uniform Crime Reporting (UCR) Program indicated that arson incidents increased 19.2% in the first six months of 2020 compared to the first six months of 2019 [2]. One of the most useful ways to deem a fire as intentional is through the identification of an ignitable liquid which is often used as an accelerant to increase the speed and spread of a fire. Investigators collect fire debris into metal cans or glass jars where various ASTM methods to extract ignitable liquids from the debris can be employed, such as passive-headspace concentration, dynamic-headspace concentration, solvent extraction, and solid-phase microextraction [3-6]. The extract is analyzed by gas chromatography-mass spectrometry (GC-MS) to identify the presence of any ignitable liquid present such as gasoline or diesel, again following procedures recommended by ASTM [7]. Liquids are classified based on the chemical composition and carbon range (Table 1.1).

Table 1.1. ASTM Classification of Ignitable Liquids [7]

Class	Composition	Light (C₄ – C₉)	Medium (C₈ – C₁₃)	Heavy (C₈ – C₂₀₊)
Gasoline	C ₃ – C ₄ alkylbenzenes, Aliphatic compounds	Typically ranged from C ₈ – C ₁₂		
Petroleum Distillates	n-Alkanes in a Gaussian distribution	Petroleum ether, cigarette lighter fluids, camping fuels	Charcoal starters, paint thinners, mineral spirits	Kerosene, diesel fuel, lamp oils
Isoparaffinic Products	Branched alkanes	Aviation gasolines, lighter fluids	Copier toners, solvent cleaners, lamp oils	Spot cleaners
Aromatic Products	Aromatic compounds	Automotive parts cleaners, lacquer thinners	Brush cleaners, specialty cleaning solvents	Adhesives
Naphthenic- Paraffinic Products	Branched and cyclic alkanes	Cyclohexane- based solvents	Lamp oils, mineral spirits	Lamp oils
N-Alkanes Products	n-Alkanes		Candle oils, wax cleaners	Candle oils

Gasoline is one of the most common accelerants and thus, forensic identification is based on the presence of alkanes and alkylbenzenes in a pattern similar to that observed in reference gasoline samples. Figure 1.1A shows a typical chromatogram of unevaporated gasoline with characteristic peaks identified.

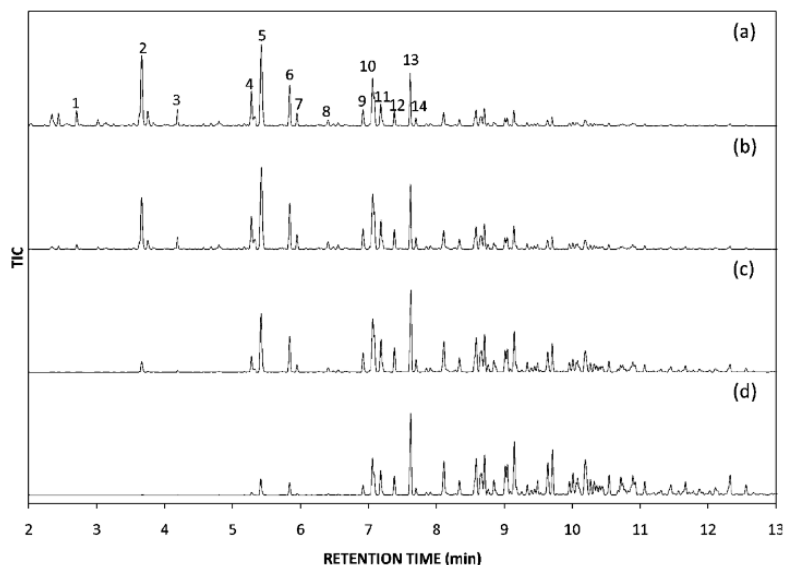


Figure 1.1. Total ion chromatogram for gasoline at (A) 0% evaporated (unevaporated), (B) 50% evaporated, (C) 75% evaporated, and (D) 89% evaporated by mass with characteristic peaks for heptane (1), toluene (2), octane (3), C₂-alkylbenzenes (4-6), and C₃-alkylbenzenes (7-13) [8]

One of the major challenges encountered in identifying volatile ignitable liquids, including gasoline, is the extent of evaporation that occurs due to the high volatility of the liquid. In the heat of the fire, the more volatile compounds undergo evaporation, changing the chemical composition of the evaporated liquid compared to the unevaporated liquid. Representative chromatograms of gasoline evaporated by mass to three different levels are shown in Figure 1.1B – D, for comparison with the chromatogram of the unevaporated gasoline (Figure 1.1A). As the extent of evaporation increases, the abundance of the more volatile compounds (*e.g.*, heptane and toluene) decreases and the chromatogram is dominated by the less volatile compounds in gasoline (*e.g.*, the C₃-alkylbenzenes) [8]. In fire debris, ignitable liquids will almost always be evaporated to some extent, necessitating a reference library of chromatograms for different liquids at different evaporation levels to aid in identification. However, experimental evaporations are time consuming and can vary depending on experimental conditions such as agitation, temperature, and evaporation vessel. As such, modeling the evaporation of liquids has

become an area of extensive research. Developing predictive models, however, requires an understanding of the evaporation process on a fundamental level as well as the molecular interactions involved.

1.2 Theory of Evaporation

Evaporation is the process by which a molecule undergoes a phase change from the liquid state to the gaseous state. For this to occur, the kinetic energy of the molecule must be greater than the intermolecular forces keeping that molecule in the liquid state [9]. In a neat liquid, the rate of evaporation is constant over time and the intermolecular forces between the solute molecules are easily predicted. For example, while the neat liquids of *n*-alkanes and aromatic compounds contain dispersion and induction forces, the aromatic compound is more polarizable and exhibits stronger intermolecular forces. The strength of molecular interactions can be evaluated based on the range over which the forces are exhibited.

Dispersion forces occur when a temporary dipole in one molecule interacts with an induced dipole in another molecule. These forces occur over only a short range, of about three angstroms (\AA) or less. The interaction energy is dependent on the polarizability and ionization energy of the molecule as well as the distance between the molecules [10]. In the case of a neat *n*-alkane, the ionization energy decreases with an increase in size. Therefore, the intermolecular forces become stronger for *n*-alkanes of larger carbon number and evaporation is slower. Dipole forces occur when a molecule with a permanent dipole interacts either with a temporary induced dipole or another permanent dipole. Similar to dispersion forces, dipole-dipole interactions occur over a short range ($> 3 \text{\AA}$) with a 64-fold decrease in the interaction if the distance is doubled [10]. Hydrogen bonding, which consists of both electrostatic and covalent interactions, also

occurs over a short range but decreases only proportionally to the distance due to the strength of the interaction.

Unlike neat liquids, the evaporation rate of mixtures is not constant with time. Molecular interactions occurring in mixtures are different than those exhibited in a neat liquid, which can lead to possible changes in the boiling points or rate constants of compounds when in a mixture [11-12]. According to Raoult's law, the vapor pressure of a pure liquid is proportional to the mole fraction of the liquid in a mixture [9]. As the mixture evaporates, the composition changes and, thus, so does the total equilibrium vapor pressure. In addition to the change in vapor pressure, the viscosity and density increase during evaporation, causing changes in the diffusion coefficients. Many predictive models have been developed that utilize the correlation between vapor pressure and evaporation rate. However, the effect of complex mixtures on the chemistry of evaporation of individual components is not well known or understood.

1.3 Modeling Evaporation using Vapor Pressure

While predicting the evaporation of complex mixtures is critical for forensic fire debris analysis, evaporation is also important in other areas of forensic science and environmental science [13-17]. Jackson and coworkers developed a semi-empirical thermodynamic model to predict evaporation of simulated gasoline mixtures, containing seven and nine components [18-19]. The vapor pressures of each compound were calculated using Antoine coefficients and the partial and total pressures were determined using Raoult's law and Dalton's law, respectively. The predictions were performed in an iterative manner, where the total volume was reduced mathematically, and the pressures were recalculated to determine the mole fraction at a given evaporation level. The mole fraction for each compound was then compared to the relative peak area in a chromatogram of the experimentally evaporated mixture. The model accurately

predicted fractional composition of the evaporated mixtures at elevated temperatures up to 210 °C.

Despite the documented success of this model, thermodynamic approaches assume that the system is fully closed and, without further correction, that the volume of vapor is equal to the volume of liquid [20]. However, for many environmental and forensic applications, evaporation from open, rather than closed, systems is more reasonable. As such, kinetic approaches have been described to model evaporation from open systems based on evaporation rate constants.

Regnier and Scott exploited vapor pressure in a kinetic model that could be used to predict the evaporation of diesel, specifically for oil spill applications [13]. The evaporation rate constants (k) of normal alkanes were determined based on the fraction remaining of each normal alkane as a function of both time (up to ~167 h) and temperature (5 – 30 °C). The natural logarithm of the rate constant was then plotted against the natural logarithm of the vapor pressure for a particular alkane, such that the regression equation could predict rate constant based on the known vapor pressure. Butler *et al.* similarly related evaporation rate constant to vapor pressure; however, the predictive nature was extended to other compound classes in diesel, assuming that the vapor pressure of the compound was related exponentially to the normal alkane with the same number of carbons [14]. While both of these works demonstrate the ability to create a predictive model for evaporation, each model was based on individual compounds rather than the bulk fuel and required that the identity of those compounds be known. This is not practical for a forensic laboratory, where the identity of the ignitable liquid in fire debris is unknown and the liquid contains hundreds of compounds.

Okamoto *et al.* more recently applied the relationship of vapor pressure to evaporation rate constants with a more forensic focus, intending to identify the fire hazard of vapors

following a spill [16-17]. Rather than individual compounds, the model predicted the evaporation of bulk fluids of gasoline and mixtures of gasoline and kerosene. Although the model accounted for bulk fuels, the vapor pressures of individual compounds were still needed and, as such, were measured experimentally at various temperatures (10 – 40 °C). Again, this is impractical for forensic fire debris applications.

1.4 Kinetic Model based on Gas Chromatographic Retention Index

To overcome the need to know the identity of compounds, McIlroy *et al.* developed a kinetic model to predict evaporation rate constant as a function of gas chromatographic retention index (I^T) and temperature [21]. Retention index normalizes the retention time of any given compound to that of the normal alkanes eluting before and after such that a scale is developed relative to the normal alkanes. Using a nonpolar stationary phase (100% dimethylpolysiloxane), the interactions of the analyte and the stationary phase are based solely on boiling point, allowing retention index to be used to determine evaporation rate constant, negating the need to know the identity of the compound. The kinetic-based model was developed by experimentally evaporating a thin layer of diesel atop water in a petri dish in an evaporation chamber with controlled temperature and humidity (Figure 1.2). The evaporation chamber contained a flow of fresh air that was sparged through water to maintain a high humidity. A peristaltic pump pulled the evaporated compounds out of the chamber and through a carbon trap on which the vapors were adsorbed. The fresh air was then recirculated through the chamber.

At various time points throughout the 300-h evaporation, the petri dishes were removed and the remaining diesel was extracted using dichloromethane (CH_2Cl_2). The diluted extracts were then analyzed by GC-MS and the chromatographic abundances were normalized to *n*-

heneicosane (C_{21}), a low volatility alkane that was unaffected by evaporation during the 300-h time period.

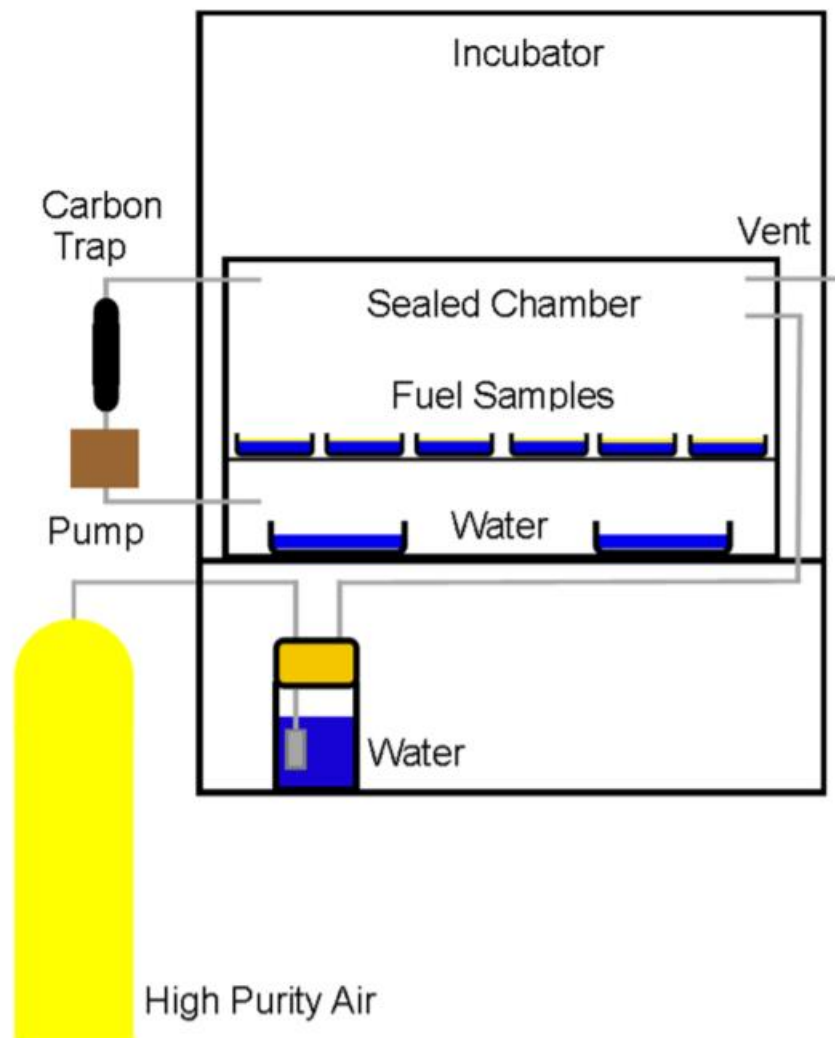


Figure 1.2. Schematic of the evaporation chamber used by McIlroy *et al.* for experimental evaporations of diesel [21]

The normalized abundances of 51 – 78 compounds (I^T ranging from 800 to 1400) from different compound classes in diesel (*e.g.*, normal alkanes, branched alkanes, alkyl aromatics, *etc.*) were then plotted as a function of evaporation time to generate decay curves. The data were fit to a first-order kinetic equation represented by Eq. 1.1, where C_t is the concentration of a compound at a given time point, C_0 is the concentration at time zero, k is the evaporation rate constant, and t is time. Concentration is directly proportional to abundance in chromatographic data.

$$C_t = C_0 \times \exp(-k \times t) \quad (1.1)$$

Figure 1.3 demonstrates the use of the total ion chromatograms for diesel at different levels of evaporation to determine the rate constants for individual compounds.

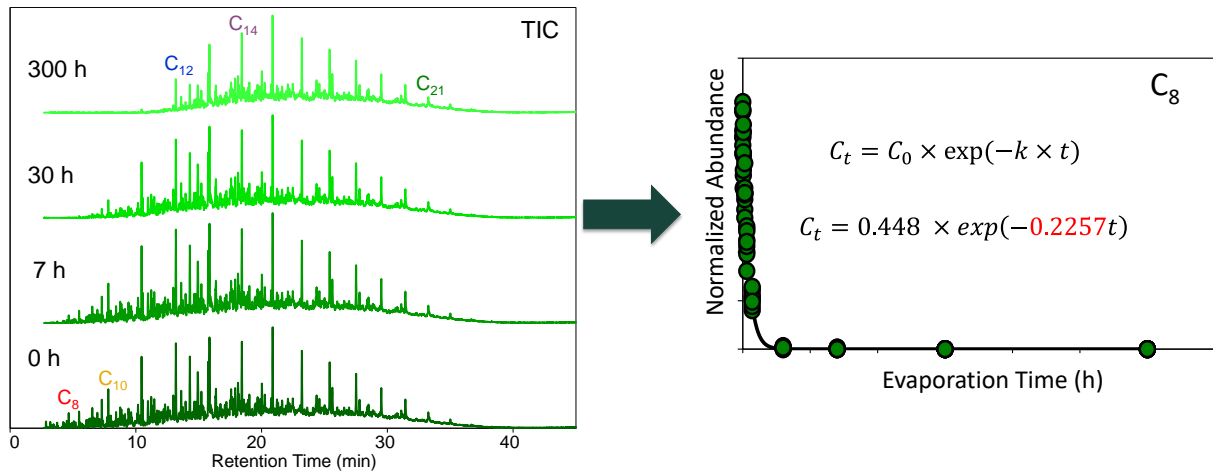


Figure 1.3. Total ion chromatograms of diesel evaporated to 0, 7, 30, and 300 h and the resultant decay curve for octane where the rate constant (k) is represented in red [21]

The natural logarithm of the experimentally determined rate constants was then plotted *versus* retention index across the range $I^T = 800 - 1400$, and linear regression was performed to define the kinetic model (Eq. 1.2).

$$\ln(k) = -1.05 \times 10^{-2} I^T + 6.71 \quad (1.2)$$

The evaporation rate constant of any compound in an unknown ignitable liquid is determined by calculating retention index from the retention time and using Eq. 1.2. The kinetic model was validated by comparing experimental values of k for compounds not used in the development of the model to predict values calculated by the model. Unlike the previous models that used boiling point and vapor pressure, the compound identity is not required in this kinetic model, as the rate constant is determined as a function of retention index.

McIlroy *et al.* demonstrated the application of the model for environmental spills to predict the fraction remaining (F_{I^T}) of compounds in diesel after a given time [21]. To determine F_{I^T} , Eq. 1.1 is rearranged to be expressed as F_{I^T} and Eq. 1.2 is rearranged to solve for k . The rearranged Eq. 1.2 can then be substituted into the rearranged Eq. 1.1 to yield Eq. 1.3, which represents the fraction remaining at a particular retention index at a particular time.

$$F_{I^T} = \frac{C_t}{C_0} = \exp(-kt) = (-(\exp(-1.05 \times 10^{-2}I^T + 6.71) \times t)) \quad (1.3)$$

From Eq. 1.3, the fraction remaining of any compound at a given time can be determined as a function of I^T , meaning that the identity of the particular compound does not need to be known.

Although developed for diesel and initially demonstrated for environmental applications, the model has potential for forensic fire debris applications. As fraction remaining is related to evaporation, the kinetic model can be used to generate chromatograms corresponding to evaporated ignitable liquids for reference libraries [22]. To do this, the fraction remaining is plotted against retention index to create fraction remaining curves corresponding to different total fraction remaining (F_{Total}) levels (Figure 1.4). The F_{Total} of the liquid is determined using Eq. 1.4, where F_j is the fraction remaining at a particular I^T and C_j is the concentration, or chromatographic abundance, at that I^T value.

$$F_{Total} = \frac{\sum_{j=I_i^T}^{I_f^T} F_j C_j}{\sum_{j=I_i^T}^{I_f^T} C_j} \quad (1.4)$$

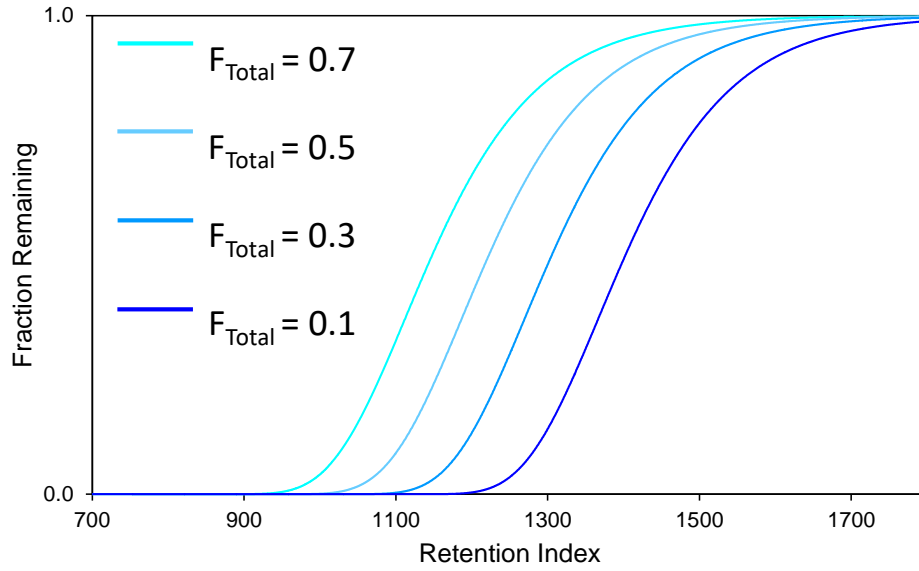


Figure 1.4. Fraction remaining curves corresponding to a total fraction remaining of 0.7, 0.5, 0.3, and 0.1 [22]

The fraction remaining curve is multiplied by the chromatogram of the corresponding unevaporated ignitable liquid to yield the predicted chromatogram for a given F_{Total} , or level of evaporation (Figure 1.5).

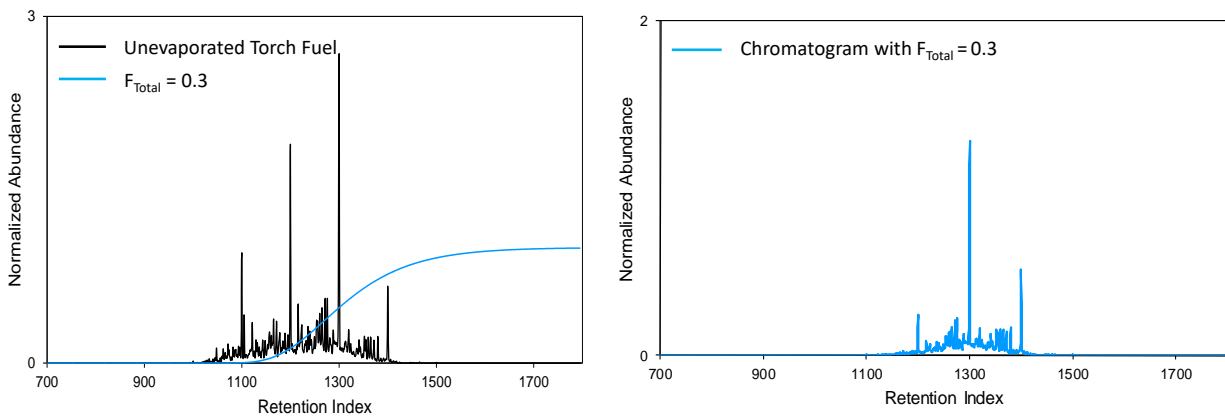


Figure 1.5. Chromatogram of unevaporated torch fuel multiplied by a F_{Total} curve of 0.3 to yield a predicted chromatogram of 70% evaporated torch fuel [22]

This kinetic model was used to successfully predict chromatograms for evaporated petroleum distillates, with Pearson product-moment correlation (PPMC) coefficients ranging from 0.920 to 0.998 for evaporation levels ranging from 90% to 30%. However, for gasoline, which contains more volatile compounds, the predictive accuracy of the model was lower, with PPMC coefficients ranging from 0.772 to 0.949 for evaporation levels ranging from 90% to 30% [22]. In later work, the GC method was optimized for the more volatile compounds and the F_{Total} was calculated based on area under the chromatogram rather than mass loss [23]. The GC method was adapted by subtracting background interferences and eliminating the solvent delay, which allowed for the identification of compounds with $I^T < 800$ (Figure 1.6).

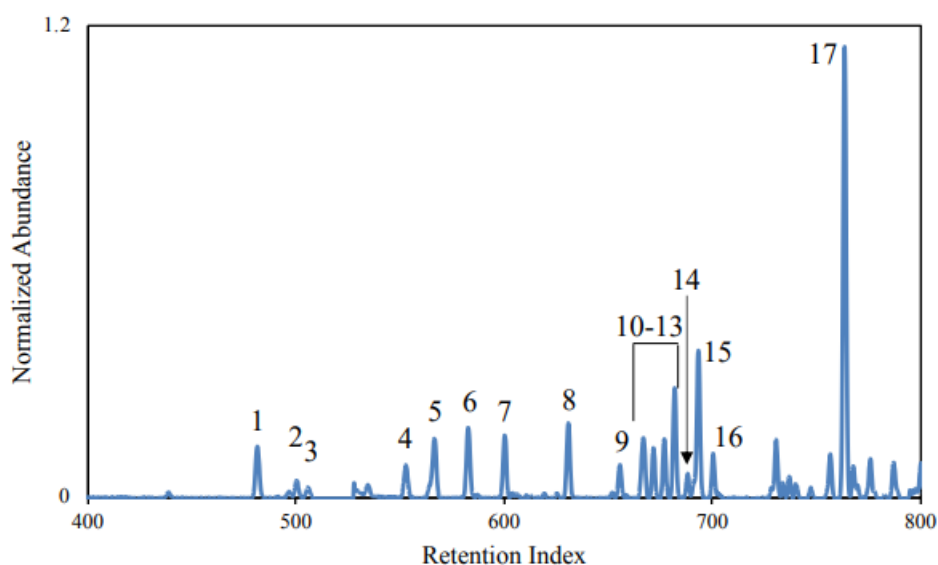


Figure 1.6. Chromatogram of gasoline in range I^T 400 – 800. Compounds identified as (1) methylbutane, (2) *n*-pentane, (3) methylbutene, (4) dichloroethylene, (5) methylpentane isomer, (6) methylpentane isomer, (7) *n*-hexane, (8) methylcyclopentane, (9) benzene, (10) cyclohexane, (11) dimethylpentane, (12) methylhexane, (13) cyclohexene, (14) dimethylcyclopentane, (15) tetramethylbutane, (16) *n*-heptane, and (17) toluene [23]

With the modifications made, PPMC coefficients across the same evaporation range improved to 0.937 to 0.991 [23]. Despite the improvement in performance, the model was extrapolated below the range over which it was originally developed (*i.e.*, $I^T = 800 - 1400$) to predict evaporation of the more volatile compounds in gasoline.

1.4.1 Development of a Variable-Temperature Model

Temperature has a significant effect on the extent of evaporation, especially for more volatile compounds. As temperature is increased, the kinetic energy of the molecules increases, and more molecules overcome the intermolecular forces of attraction and evaporate. Figure 1.7 represents diesel evaporated for 300 h at six different temperatures. At 300 h, compounds eluting before *n*-decane ($I^T > 1000$) are entirely evaporated at temperatures ranging from 5 – 20 °C. However, at temperatures over 20 °C, compounds with $I^T < 1200$ are largely evaporated [24].

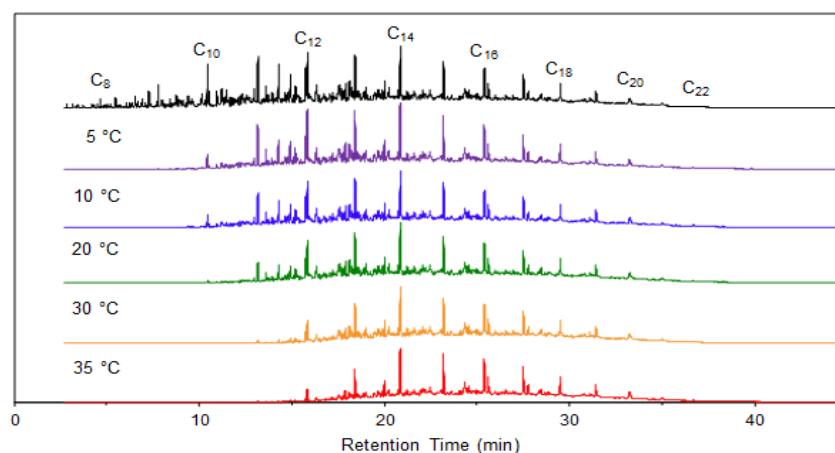


Figure 1.7. Chromatogram of unevaporated diesel (black) and diesel evaporated for 300 h at 5°C (purple), 10°C (blue), 20°C (green), 30°C (yellow), and 35°C (red) [24]

A temperature-dependent model was created to account for the effect of temperature on the evaporation of ignitable liquids [24]. The same evaporation procedure was followed but at temperatures varying from 5 to 35°C. Decay curves were generated for the same compounds used in the previous model ($I^T = 800 - 1400$) at each temperature such that a rate constant could

be determined for that compound at five temperatures. Temperature is inversely related to the evaporation rate constant by the Arrhenius equation (Eq. 1.5), where k is the evaporation rate constant, A is the pre-exponential factor, E_A is the activation energy, R is the universal gas constant, and T is absolute temperature.

$$\ln(k) = \ln A - \frac{E_A}{RT} \quad (1.5)$$

Given this inverse relationship of temperature and rate constant, multiple linear regression was performed to yield the variable temperature model demonstrated by Eq. 1.6.

$$\ln(k) = m_1 I^T + m_2 \left(\frac{1}{T}\right) + b = -0.0103 I^T - 6410 \left(\frac{1}{T}\right) + 28.7 \quad (1.6)$$

Eq. 1.5 was substituted into Eq. 1.1 to yield Eq. 1.7, which represents the fraction remaining at a given retention index as a function of both retention index and absolute temperature.

$$F_{I,t} = \exp\left(-\left(\exp\left(-0.0103 I^T - 6410 \left(\frac{1}{T}\right) + 28.7\right) \times t\right)\right) \quad (1.7)$$

Using the temperature-dependent model, predicted chromatograms can be generated that represent different ignitable liquids at various temperatures and evaporation levels. However, this variable-temperature model was developed using diesel and does not extend to retention indices relevant in gasoline samples, specifically the more volatile compounds. The work presented in this dissertation aims to extend both the fixed- and variable-temperature models to a lower I^T range and evaluate the performance of the refined models to predict evaporation of more volatile compounds.

1.5 Effect of Interface on Evaporation

While mixtures introduce a new set of intermolecular interactions compared to neat liquids, the interface at which a liquid evaporates presents additional possible interactions which can affect the rate of evaporation. Much of the current literature focuses on the kinetics of evaporation for colloidal droplets on different surfaces [25]. Few studies have explored the effect of the chemical and physical properties of the interface on the evaporation of ignitable liquids, which exhibit increased wetting of surfaces and therefore evaporate as a thin film rather than droplets. Many interfaces are expected to be present at the scene of a suspicious fire including, but not limited to, wood, tile, and textile substrates. Ignitable liquids used as an ignition source can be spread across any of these surfaces, necessitating an understanding of how interactions with the interface affect the evaporation of liquids from those interfaces.

Adsorption is a chemical process in which molecular interactions occur between a liquid and a solid substrate. The interactions can either be dispersive (*i.e.*, London or van der Waals forces) or specific, such as those occurring from Lewis acid-base interactions or hydrogen bonding [26]. As with interactions between molecules in a mixture, the strength of the interaction energy between a molecule and interface depends on many factors (*i.e.*, polarizability, ionization energy, dipole moment, separation distance) [10]. Stronger interactions lead to stronger adsorption of a molecule to a substrate which may lead to a decrease in the evaporation rate.

Aqel *et al.* measured the adsorption and assessed the extent of evaporation of both gasoline and diesel fuel on four common textiles: wool, silk, polyester, and cotton [27]. The textiles were saturated in the fuel, burned for 2 min, extinguished under a beaker, and placed in a nylon bag. A solid-phase microextraction (SPME) fiber with a polydimethylsiloxane coating was inserted into the bag and the extract was analyzed by GC-MS. The abundance of target

compounds, including *n*-alkanes and aromatic compounds, in both gasoline and diesel was measured by GC-MS following extraction from each substrate.

The target compounds persisted longer on wool and silk than on cotton and polyester, which was due to differences in sorption characteristics among the textiles. A larger discrepancy in the percentage evaporated was observed for *n*-pentadecane between wool and the other three fabrics compared to 1,3,5-trimethylbenzene. Three hours after extinguishing the fire, *n*-pentadecane was only 58% evaporated on the wool compared to 75 – 85% evaporated from the silk, cotton, and polyester. In contrast, 1,3,5-trimethylbenzene was 47% evaporated from the wool and 55 – 65% evaporated from the other three textiles [27]. This suggests that the *n*-alkane had stronger interactions with the wool when compared to the other fabrics, while the interactions between the aromatic compound and fabrics were more similar across the four fabrics. While this study highlights the significance of substrate identity on the persistence of ignitable liquids in fire debris, the authors only identified trends in the absence or presence of various target compounds. A method to quantify these differences (*e.g.*, based on evaporation rate constants) was not established. Additionally, the surface characteristics of the fabrics were not determined, making conclusions about the molecular interactions between the target compounds and the substrates impossible.

With a similar goal to study the adsorption of target compounds on household materials, Fraunhofer *et al.* measured the molar enthalpy of adsorption (ΔH_m) of hydrocarbons present in gasoline using inverse gas chromatography [26]. ΔH_m reflects the magnitude of interactions between target compounds and solid substrates by measuring the energy released or absorbed when a molecule adsorbs to a surface. A small volume of each probe compound (*n*-heptane, *n*-octane, *n*-nonane, toluene, *p*-xylene, and 1,2,4-trimethylbenzene) was injected into a column

packed with a stationary phase of either polyester carpet fibers, cotton fabric, or cardboard. The retention time, which was dependent on the interaction of the compound with the given stationary phase, was monitored for each compound at temperatures ranging from 40 – 70 °C, in 10 °C increments. Retention time was then used to calculate the specific retention volume (V_g°) of the compound and the natural logarithm of V_g° was plotted versus $1/T$. The slope of this regression was used to calculate ΔH_m for each probe compound on each substrate and the values were compared.

For the hydrophobic polyester carpet fibers, ΔH_m became more negative as hydrocarbon sized increased. This was due to the addition of CH_2 groups, which led to an increase in the dispersive components of the molecular interactions. The ΔH_m values of *n*-alkanes were generally more exothermic than for aromatic compounds with similar carbon number. For example, the molar enthalpy of adsorption for *n*-heptane on the carpet fibers was -23.4 kJ/mol while it was only -18.4 kJ/mol for toluene [26]. The ΔH_m for the probe compounds on the cotton and cardboard were more exothermic than those for the polyester fibers, owing to an increased contribution of dispersive components. Overall, the findings demonstrated that adsorption of hydrocarbons depends largely on the chemical composition and porosity of the substrate, as well as the size and polarity of the hydrocarbon. However, the porosity of the substrates was not quantified and the contributions from either chemistry or porosity were not differentiated.

While the work by Aqel *et al.* and Frauenhofer *et al.* measured the adsorption of compounds commonly found in gasoline and diesel to different substrates, Wensel looked more directly at the effect of substrate on evaporation [26-28]. Using the thermodynamic model developed by Jackson and coworkers and discussed in Section 1.2, a nine-component mixture was evaporated from four substrates: nylon carpet, cotton, pinewood, and plywood [28]. The

penetration depth of the mixture was observed, and weathering was monitored based on the fractional composition of each component in the mixture. When the mixture reached 50% weathered, the fractional composition of each component ceased to change, indicating that the substrates slowed down the evaporation due to the penetration of the compounds into the substrate. At these points, the error in prediction for the mathematical model was poorer because the evaporation rates of the components deviated from those predicted based on native vapor pressures. However, the deviations were less for the nylon carpet and cotton fabric compared to the two wood samples, which suggests that these substrates have less effect on the evaporation of compounds found in gasoline. The authors postulated that this difference may be due to the increased porosity of the wood and thus deeper penetration of the liquids.

Each of the studies described in this section demonstrate the significance of the interface in the adsorption and persistence of ignitable liquids. However, thermodynamic measurements such as molar enthalpy of adsorption were utilized. The kinetic model developed by McIlroy *et al.* measured evaporation rate constants of hydrocarbons using a thin film of diesel on water [21]. The model has since been used to predict reference collections of liquids evaporated to different levels. Chromatograms of fire debris extracts, which can consist of many different types of substrates commonly found at crime scenes, can then be compared to the predicted reference collection to identify the liquid present. For this reason, a study of the direct effect of the interface between ignitable liquid and substrate on the evaporation rate constant of compounds from different classes is necessary to validate the full use of the model for application in fire debris analysis.

1.6 Objectives and Aims

The first objective in this work is to extend the kinetic model to a lower I^T range, which requires the experimental determination of evaporation rate constants for compounds eluting in this range. However, several problems arise when experimentally measuring the rate constants of volatile compounds. Their high volatility results in rapid generation of vapor, which poses the risk of fire or explosion. Additionally, the vapor must be efficiently removed from the system to approximate an open system and prevent condensation. Finally, rapid sample preparation and analysis are necessary to minimize additional evaporation. The objective in this work is to measure evaporation rate constants for volatile compounds, addressing the problems discussed above. In order to accomplish this objective, the following aims were outlined:

Aim 1: Perform theoretical calculations for a series of n -alkanes in the range $I^T = 400 - 800$ to determine a set of evaporation parameters that ensures the volume of vapor remains below the explosion limit.

Aim 2: Experimentally determine rate constants for selected volatile compounds of interest in the range $I^T = 400 - 800$ at temperatures of 10, 20, and 30 °C and develop a method to correct for condensation.

Aim 3: Validate the refined fixed- and variable-temperature models.

In this work, compound standards were purchased and evaporated as binary mixtures to reduce the vapor load in the evaporation chamber and, thereby, ensure safe evaporations. A method to correct the rate constants for condensation was established to quantify the amount of vapor condensing during the experimental evaporations. A corrected rate constant was then determined by refitting the curve to the first-order kinetic rate equation. A validation mixture was prepared, evaporated, and analyzed by GC-MS. The refined models both uncorrected and corrected for

condensation, as well as the original model developed by McIlroy *et al.* [21, 24], were used to predict chromatograms corresponding to the evaporated validation mixture. The predictive performance of each model was assessed first through PPMC coefficients and then using the percent error in predicting the abundance of each individual peak in the chromatogram.

The second objective in this work is to study the effect of interface on the evaporation of compounds commonly found in ignitable liquids. The original model was developed by evaporating diesel from a thin layer of water and the refined model demonstrated in this work evaporated binary mixtures directly from the surface of glass dishes. At the scene of fire, many different substrates would exist from which ignitable liquids evaporate. To determine the effect of interface on evaporation, three aims were outlined:

Aim 1: Perform experimental evaporations of diesel from the two interfaces previously studied (water and glass petri dish) and two additional common household substrates (cotton and polyester fabric).

Aim 2: Determine evaporation rate constants for compounds in three identified homologous series that represent different compounds classes (normal alkanes, alkylbenzenes, and alkyl cyclohexanes).

Aim 3: Develop predictive models for each homologous series on each interface.

In this work, diesel was purchased from a local gas station and evaporated from each of the four interfaces. Decay curves were generated for the selected compounds in the three homologous series for each interface and the evaporation rate constants were compared. Regression models were then developed for each compound class for each interface and compared to determine the effect of the interface on the relationship between retention index and evaporation rate constant. This would determine the necessity of substrate-specific models when applying the kinetic model

to forensic fire debris analysis and provide the basis for several models developed from textiles commonly found in household materials.

REFERENCES

REFERENCES

- [1] United States Bomb Data Center. *Arson Incident Report*; Department of Justice: 2018.
- [2] FBI National Press Office, Overview of Preliminary Uniform Crime Report, January-June, 2020. 202 ed.; Washington, D.C.
- [3] ASTM E1412-16: Standard practice for separation of ignitable liquid residues from fire debris samples by passive headspace concentration with activated charcoal. ASTM International, West Conshohocken, PA, 2016.
- [4] ASTM E1413-13: Standard practice for separation of ignitable liquid residues from fire debris samples by dynamic headspace concentration. ASTM International, West Conshohocken, PA, 2013.
- [5] ASTM E1386-15: Standard practice for separation of ignitable liquid residues from fire debris samples by solvent extraction. ASTM International, West Conshohocken, PA, 2015.
- [6] ASTM E2154-15a: Standard practice for separation and concentration of ignitable liquid residues from fire debris samples by passive headspace concentration with solid phase microextraction (SPME). ASTM International, West Conshohocken, PA, 2015.
- [7] ASTM 1618-14: Standard test method for ignitable liquid residues in extracts from fire debris samples by gas chromatography-mass spectrometry. ASTM International, West Conshohocken, PA, 2014.
- [8] D.A. Turner, J.V. Goodpaster, Comparing the effects of weathering and microbial degradation on gasoline using principal components analysis. *Journal of Forensic Sciences* **2012**, 57 (1), 64-69.
- [9] D.L. Reger, S.R. Goode, D.W. Ball, *Chemistry: Principles and Practice*. Third Edition ed.; Brooks/Cole: Belmont, CA, 2010.
- [10] V.L. McGuffin, Theory of Chromatography. In *Chromatography, 6th Edition*, Heftmann, E., Ed. Elsevier: Amsterdam, Netherlands, 2004; Vol. 69A, pp 1-94.
- [11] K. Okamoto, N. Watanabe, Y. Hagimoto, K. Miwa, H. Ohtani, Evaporation characteristics of multi-component liquid. *Journal of Loss Prevention in the Process Industries* **2010**, 23, 89-97.
- [12] M.F. Fingas, Studies on the evaporation of crude oil and petroleum products. II. Boundary layer regulation. *Journal of Hazardous Materials* **1998**, 57, 41-58.
- [13] Z.R. Regnier, B.F. Scott, Evaporation rates of oil components. *Environmental Science Technology* **1975**, 9, 469-472.

- [14] J.N. Butler, Evaporative weathering of petroleum residues: the age of pelagic tar. *Marine Chemistry* **1975**, *3*, 9-21.
- [15] T.J. Bruno, T.M. Lovestead, M.L. Huber, Prediction and preliminary standardization of fire debris constituents with the advanced distillation curve method. *Journal of Forensic Science* **2011**, *56*, S192-S202.
- [16] K. Okamoto, N. Watanabe, Y. Hagimoto, K. Miwa, H. Ohtani, Changes in evaporation rate and vapor pressure of gasoline with progress of evaporation. *Fire Safety Journal* **2009**, *44*, 756-763.
- [17] K. Okamoto, M. Hiramatsu, H. Miyamoto, T. Hino, M. Honma, N. Watanabe, Y. Hagimoto, K. Miwa, H. Ohtani, Evaporation and diffusion behavior of fuel mixtures of gasoline and kerosene. *Fire Safety Journal* **2012**, *44*, 47-61.
- [18] H.L. Birks, A.R. Cochran, T.J. Williams, G.P. Jackson, The surprising effect of temperature on the weathering of gasoline. *Forensic Chemistry* **2017**, *4*, 32-40.
- [19] I.C. Willis, Z. Fan, J.T. Davidson, G.P. Jackson, Weathering of ignitable liquids at elevated temperatures: A thermodynamic model, based on laws of ideal solutions, to predict weathering in structure fires. *Forensic Chemistry* **2020**, *18*, 100215.
- [20] V.L. McGuffin, R. Waddell Smith, A unified kinetic and thermodynamic model of evaporation for forensic applications. *Forensic Chemistry* **2021**, *23*, 100304.
- [21] J.W. McIlroy, A.D. Jones, V.L. McGuffin, Gas chromatographic retention index as a basis for predicting evaporation rates of complex mixtures. *Analytica Chimica Acta* **2014**, *852*, 257-266.
- [22] R. Waddell Smith, R.J. Brehe, J.W. McIlroy, V.L. McGuffin, Mathematically modeling chromatograms of evaporated ignitable liquids for fire debris applications. *Forensic Chemistry* **2016**, *2*, 37-45.
- [23] N.K. Eklund, B.A. Capistran, V.L. McGuffin, R. Waddell Smith, Improvements in a kinetic-based model to predict evaporation of gasoline. *Forensic Chemistry* **2020**, *17*, 100194.
- [24] J.W. McIlroy, R. Waddell Smith, V.L. McGuffin, Fixed- and variable-temperature kinetic models to predict evaporation of petroleum distillates for fire debris applications. *Separations* **2018**, *5* (47), 1-19.
- [25] Y. Zhang, X. Chen, F. Liu, L. Li, J. Dai, T. Liu, Enhanced coffee-ring effect via substrate roughness in evaporation of colloidal droplets. *Advances in Condensed Matter Physics* **2018**, *2018*, 1-9.

- [26] E. Fraunhofer, J. Cho, J. Yu, Z. Y. Al-Saigh, J. Kim, Adsorption of hydrocarbons commonly found in gasoline residues on household materials studied by inverse gas chromatography. *Journal of Chromatography A* **2019**, *1594*, 149-159.
- [27] A. Aqel, A. M. Dhabbah, K. Yusuf, N. M. Al-Harbi, Z. A. Al Othman, A. Y. Badjah-Hadj-Ahmed, Determination of gasoline and diesel residues on wool, silk, polyester, and cotton materials by SPME-GC-MS. *Journal of Analytical Chemistry* **2016**, *71* (7), 730-736.
- [28] Wensel, C. The Effects of Household Substrates on the Evaporation of Ignitable Liquids at Temperatures up to 210 C. [Master's Thesis]. Morgantown, WV: West Virginia University, 2020.

II. Theoretical Calculations of Vapor Load

2.1 Introduction

In previous work, diesel fuel was evaporated directly to determine experimental rate constants for compounds spanning various compound classes, such as *n*-alkanes, branched alkanes, and aromatics [1,2]. Predicting the evaporation of more volatile ignitable liquids, such as gasoline, that are significant for fire debris analysis requires the determination of experimental rate constants for more volatile compounds. However, it is not safe to evaporate gasoline directly using the same methods described by McIlroy *et al.* [1,2], owing to its higher volatility. Accordingly, individual compounds were evaporated such that the vapor pressure and volume of each could be adjusted, as needed, to minimize the risk of fire or explosion. The lower flammability limit (LFL), also known as the lower explosive limit (LEL), represents the minimum concentration of fuel vapor (%v/v in air) at which flame ignition or explosion is possible in the presence of an ignition source.

Theoretical calculations were first performed using *n*-alkanes with retention indices in the range of interest (*e.g.*, $I^T = 400 - 800$ for *n*-butane to *n*-octane). The LFL values for these compounds range from 1.6 %v/v (*n*-butane) to 1.0 %v/v (*n*-octane) [3]. These calculations determined a safe I^T range as well as a safe set of evaporation parameters to ensure that the vapor load in any given experiment would remain below the LFL. Using the selected parameters, the theoretical calculations were repeated for the selected volatile compounds identified in gasoline with $I^T < 800$. This chapter describes the theoretical calculations performed and summarizes the vapor load for the compounds selected for evaporation given the safe set of evaporation parameters.

2.2 Theoretical Calculations of Vapor Load for Normal Alkanes

The evaporation rate constant (k) for each n -alkane was predicted for temperature (T) = 10, 20, 30, and 40 °C, converted to absolute temperature, using the variable-temperature model (Eq. 2.1) developed by McIlroy *et al.* [2]

$$\ln(k) = m_1 I^T + m_2 \left(\frac{1}{T}\right) + b \quad (2.1)$$

where the regression coefficients were determined as $m_1 = -0.0103$, $m_2 = -6410$, and $b = 28.7$ over the retention index range $I^T = 800 - 1400$ and temperature range $T = 5 - 35$ °C. From the predicted rate constant, the fraction remaining ($F_{I^T,t}$) for a compound with retention index I^T at time t was determined using a first-order rate equation (Eq. 2.2)

$$F_{I^T,t} = \frac{C_{I^T,t}}{C_{I^T,0}} = \exp(-k t) \quad (2.2)$$

where the concentration of that compound at time t and $t = 0$ ($C_{I^T,t}$ and $C_{I^T,0}$, respectively) is proportional to the chromatographic abundance. To find $F_{I^T,t}$ as a function of I^T and temperature (T), Eq. 2.1 was rearranged to solve for k and substituted into Eq. 2.2, yielding Eq. 2.3.

$$F_{I^T,t} = \frac{C_{I^T,t}}{C_{I^T,0}} = \exp\left(-\exp\left(m_1 I^T + m_2 \left(\frac{1}{T}\right) + b\right) t\right) \quad (2.3)$$

The total volume of vapor generated by each n -alkane in the gas phase (V_G) for a specific volume in the liquid phase (V_L) was determined and converted to a relative volume (% v/v), as shown in Eq. 2.4.

$$V_{G,t} = (1 - F_{I^T,t}) \frac{V_L N \rho_L \bar{V}}{M V_B} \times 100\% \quad (2.4)$$

In this equation, N is the number of evaporation dishes, ρ_L is the density and M is the molar mass of the liquid, \bar{V} is the molar volume of an ideal gas (*i.e.*, 22.4 L/mol at 0 °C and 1 atm), and V_B is the volume of the evaporation chamber box, as described in Chapter 1, Section 1.4. For these calculations, the volume of each compound per dish (V_L) was varied from 0.025 to 0.10 mL.

The first set of parameters explored the highest temperature ($T = 40\text{ }^{\circ}\text{C}$), volume per dish ($V_L = 0.10\text{ mL}$), and number of dishes ($N = 18$), as this would yield a vapor load at or near the LFL for the *n*-alkanes. The absolute volume (mL) of vapor, as well as the relative volume (% v/v) normalized to the volume of the box, are shown in Figures 2.1A and 2.1B, respectively, for *n*-butane to *n*-octane. The end of the curve for each *n*-alkane in Figure 2.1A represents the time at which $t = 5\tau$, where the characteristic lifetime $\tau = 1/k$. At this time, the fraction remaining from the first-order kinetic equation (Eq. 2.1) is $F_{I',t} = \exp(-5) = 0.007$, corresponding to an evaporation level of 99.3% (*i.e.*, nearly complete). The difference in volatility is clearly demonstrated based on the time at which 5τ is reached: for the most volatile compound (*n*-butane), 5τ is reached within six minutes, while for the least volatile compound (*n*-octane), 5τ is reached by 5 h. In a closed system, the time at which the vapor maximizes is very close to 5τ . The maximum vapor load, both in absolute and relative volume, is also indicative of volatility. Using the same parameters as above, the vapor reaches a maximum absolute volume of 400 mL for *n*-butane, which corresponds to a relative volume of 1.2 % v/v (Figures 2.1A and 2.1B). Conversely, *n*-octane exhibits a maximum absolute volume of 287 mL and a relative volume of 0.86 % v/v (Figures 2.1A and 2.1B).

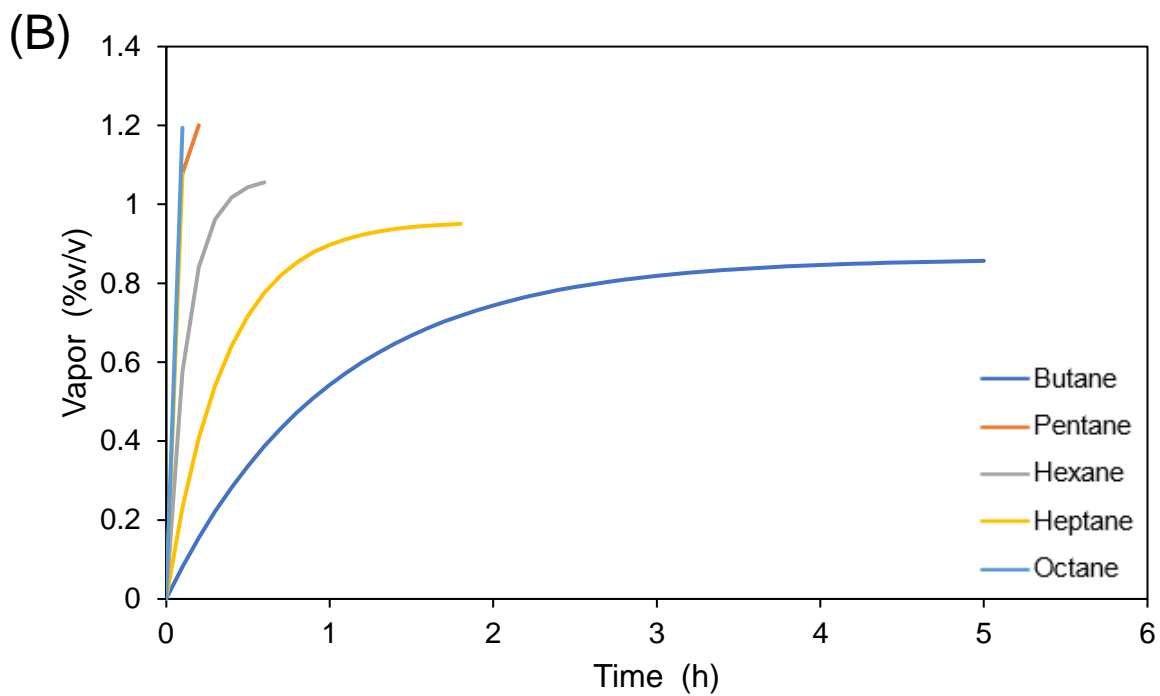
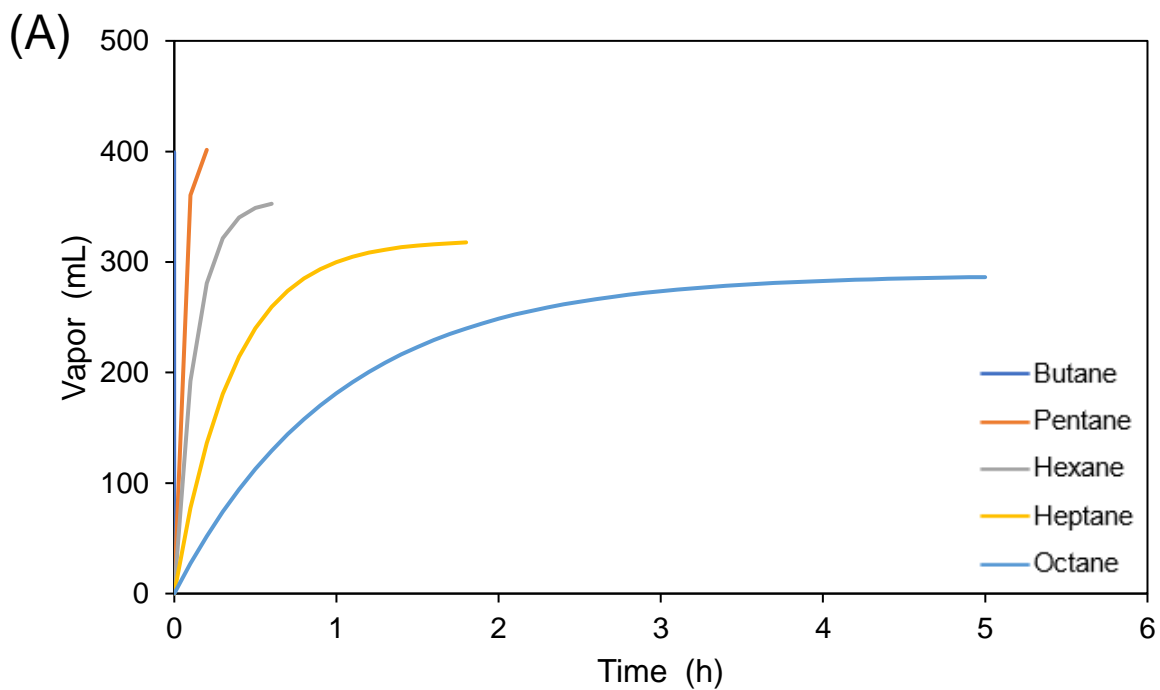
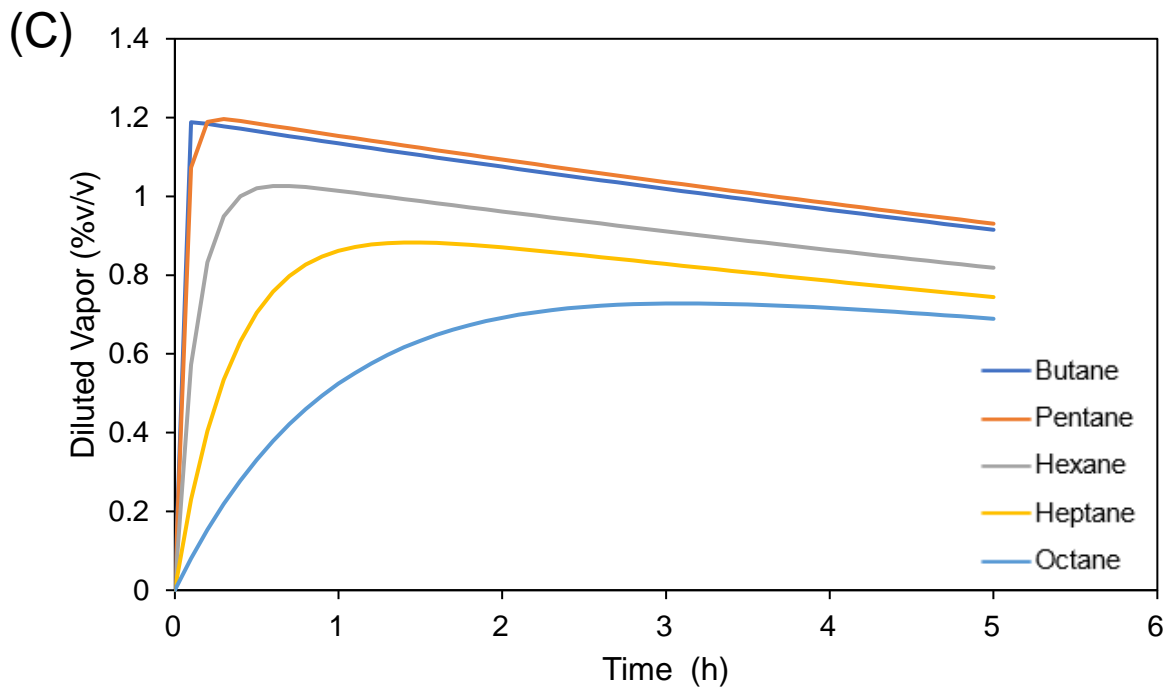


Figure 2.1. Vapor load calculations for the normal alkanes at 40 °C with a volume of 0.10 mL shown in (A) mL, (B) %v/v, and (C) %v/v when incorporating flow rate (30 mL/min)

Figure 2.1. (cont'd)



The theoretical volume of vapor calculated in Eq. 2.4 represents the absolute or relative volume of vapor that would be generated in a closed or static system. The evaporation chamber described in Chapter 1, Section 1.4 includes several sources of air flow intended to dilute and remove vapors from the system. The relative volume of vapor ($V_{G,t_{i+1}}^Q$, % v/v) was determined as a function of flow rate (Q), as shown in Eq. 2.5.

$$V_{G,t_{i+1}}^Q = \frac{V_{G,t_i}^Q + (V_{G,t_{i+1}} - V_{G,t_i})}{V_B + Q(t_{i+1} - t_i)} \times 100\% \quad (2.5)$$

For these calculations, the flow rate of air to pump vapors from the system was varied from 30 to 120 mL/min. Using the same parameters as above, the maximum relative vapor load was reduced for each of the n -alkanes at a flow rate of 30 mL/min (Figure 2.1C) compared to when flow rate was not incorporated (Figure 2.1B). The addition of flow rate also allows for the reduction of relative volume over time as the vapors are pumped out of the chamber (Figure 2.1C).

Many of the n -alkanes in the range $I^T = 400 - 800$ exhibit explosion limits of approximately 1.0 % v/v. Using the same parameters as above, n -butane, n -pentane, and n -hexane exceed this threshold (Figure 2.1C). Additionally, at many points along the curve, the % v/v for n -butane is lower than that for n -pentane, despite being substantially more volatile. This suggests that the evaporation rate constant for n -butane may not be accurately measured. Moreover, it would be difficult to collect sufficient data before n -butane reaches 5τ at six minutes. For these reasons, n -butane was eliminated from experimental evaporations in this work.

The calculations were repeated to investigate the effects of temperature ($T = 10 - 40$ °C), flow rate ($Q = 30 - 120$ mL), and volume ($V_L = 0.025 - 0.10$ mL) on the vapor load generated as a function of retention index ($I^T = 400 - 800$). Selected examples are shown in Table 2.1, with a summary of all calculations in the Appendix (Tables A 2.1 – A 2.5). As temperature (T) increases, the maximum volume of vapor for each n -alkane also increases. For example, as

temperature increases from 10 to 40 °C, maintaining a constant flow rate of 30 mL/min and volume of 0.10 mL, the maximum vapor load generated by *n*-butane increases from 1.040 to 1.188 %v/v, representing a 12.5% increase (Table 2.1). However, for the same conditions, the maximum vapor load generated for *n*-octane increases from 0.397 to 0.728 %v/v, a 45.5% increase (Table 2.1). Hence, the increase in vapor load with temperature is greater for compounds at higher I^T and, thus, with lower volatility.

As flow rate (Q) increases, the maximum volume of vapor for each *n*-alkane decreases. For example, as flow rate increases from 30 to 120 mL/min, maintaining a constant temperature of 40 °C and volume of 0.10 mL, the maximum vapor load for *n*-butane is reduced from 1.188 to 1.169 %v/v, representing a 1.6% decrease (Table 2.1). However, for the same conditions, the maximum vapor load for *n*-octane is reduced from 0.728 to 0.560 %v/v, a 23.0% decrease (Table 2.1). Hence, the decrease in vapor load with flow rate is significantly greater for compounds at higher I^T and, thus, with lower volatility.

The final parameters explored in these theoretical calculations were the volume per dish (V_L) and number of dishes (N) which, because they both appear in the numerator of Eq. 2.4, act in similar ways. An increase or decrease in either parameter results in a proportional increase or decrease in the resulting vapor volume. For example, decreasing the volume from 0.10 to 0.025 mL, a 75% decrease, will decrease the maximum vapor load by 75% for all retention indices, all temperatures, and all flow rates (Table 2.1 and Appendix).

Based on these calculations, it was determined that experimental evaporations of compounds in the range $I^T \sim 500 - 800$ could be safely and reasonably performed for temperatures between 10 and 30 °C, using a flow rate of 60 mL/min, and a compound volume of 0.025 mL in each of 18 evaporation dishes.

Table 2.1. Maximum Calculated Vapor Load for *n*-Alkanes

Compound	I^T	Temperature (°C)	Flow Rate (mL/ min)	Volume (mL)	Dishes	Maximum Vapor Load (%v/v)_{max}	Time (h) at (%v/v)_{max}
<i>n</i> -Butane	400	40	30	0.1	18	1.188	0.1
<i>n</i> -Pentane	500	40	30	0.1	18	1.196	0.3
<i>n</i> -Hexane	600	40	30	0.1	18	1.026	0.6
<i>n</i> -Heptane	700	40	30	0.1	18	0.883	1.5
<i>n</i> -Octane	800	40	30	0.1	18	0.728	3.1
<i>n</i> -Butane	400	10	30	0.1	18	1.040	0.7
<i>n</i> -Pentane	500	10	30	0.1	18	1.008	1.6
<i>n</i> -Hexane	600	10	30	0.1	18	0.802	3.4
<i>n</i> -Heptane	700	10	30	0.1	18	0.601	6.7
<i>n</i> -Octane	800	10	30	0.1	18	0.397	12.5
<i>n</i> -Butane	400	40	120	0.1	18	1.169	0.1
<i>n</i> -Pentane	500	40	120	0.1	18	1.153	0.2
<i>n</i> -Hexane	600	40	120	0.1	18	0.953	0.5
<i>n</i> -Heptane	700	40	120	0.1	18	0.765	1.0
<i>n</i> -Octane	800	40	120	0.1	18	0.560	2.0
<i>n</i> -Butane	400	40	30	0.025	18	0.297	0.1
<i>n</i> -Pentane	500	40	30	0.025	18	0.299	0.3
<i>n</i> -Hexane	600	40	30	0.025	18	0.257	0.6
<i>n</i> -Heptane	700	40	30	0.025	18	0.221	1.5
<i>n</i> -Octane	800	40	30	0.025	18	0.182	3.1

2.3 Theoretical Calculations of Vapor Load for Selected Volatile Compounds

Due to the explosion hazard associated with experimental evaporations of volatile compounds, theoretical calculations were performed prior to evaporations to verify that the vapor generated by each of the compounds of interest for the specific experimental conditions was below the corresponding LFL. Volatile compounds present in gasoline with $I^T \leq 800$ were selected based on the work of Eklund *et al.* (Figure 1.6) [4]. Similar to the calculations performed for the *n*-alkanes, the rate constant for each compound selected for evaporation was estimated using Eq. 2.1 based on its retention index. The vapor load was calculated using Eqs. 2.3 – 2.5 and then plotted, with the curves in Figure 2.2 ending at the time at which 5τ was reached. As shown in Figure 2.2A, at 10 °C, 2-methylbutane ($I^T = 487$) was the most volatile compound and required the least time to reach 5τ at 1.8 h. In contrast, *n*-octane ($I^T = 800$) was the least volatile compound and required the longest time to reach 5τ at 44 h. For all 12 compounds, toluene ($I^T = 747$) generated the greatest absolute volume of vapor (99 mL) when reaching 5τ , followed by methylcyclopentane ($I^T = 621$) which generated 94 mL at 5τ (Figure 2.2A).

When incorporating air flow at 60 mL/min to remove vapors, the maximum vapor load of 0.237 %v/v was observed for 2-methylbutane ($I^T = 487$). This maximum was reached within 1.2 h, and 5τ was reached within 1.8 h (Figure 2.2 B). In contrast, for *n*-octane ($I^T = 800$), the maximum vapor load of 0.0734 %v/v was reached around 9.1 h, while 5τ was reached close to 44 h (Figure 2.2 B). These calculations demonstrate that, when incorporating flow rate, volatile compounds generate the highest vapor load at the beginning of the evaporation process, while less volatile compounds reach their vapor load maximum later. As such, the compounds can be safely evaporated as binary mixtures, combining a more volatile compound with a less volatile

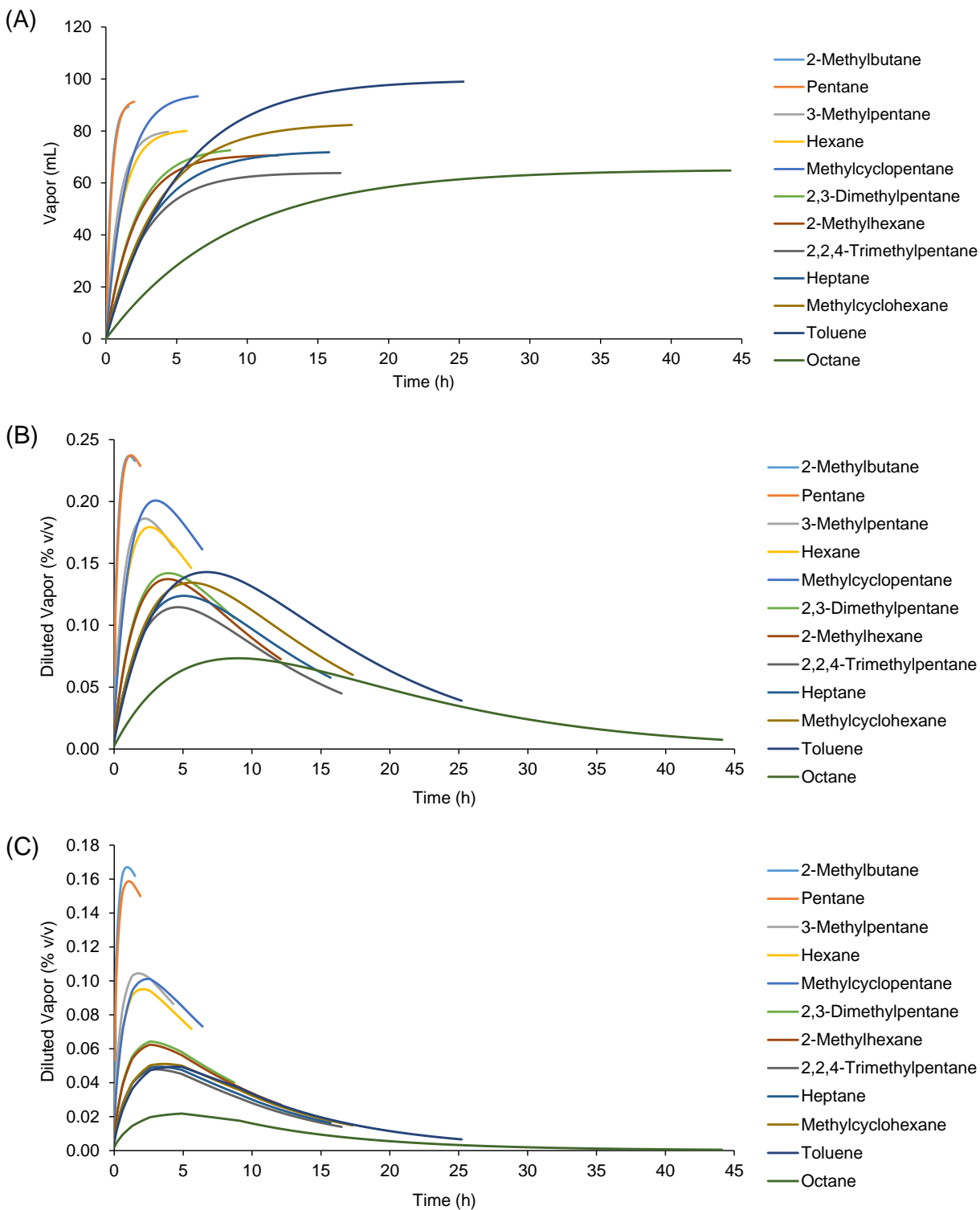


Figure 2.2. Theoretical vapor load for 12 compounds, calculated at 10 °C in (A) mL, (B) %v/v incorporating a flow rate of 60 mL/min, and (C) %v/v incorporating a flow rate of 60 mL/min and dish removal throughout evaporation

compound whose vapor load maximizes at a different time. This reduces the overall vapor generated, leading to a safer experiment with less error introduced by vapor condensation. Furthermore, any combination of two compounds should yield an additive vapor load less than 1 %v/v at all points during the evaporation, keeping the value safely below the LFL.

All of the theoretical calculations to this point incorporated the removal of vapors due to air flow through the system but did not account for the removal of petri dishes as the evaporation progressed. The previous calculations assumed that all 18 petri dishes remained in the evaporation chamber throughout the evaporation time. However, two petri dishes were removed at each of nine time points, thereby reducing the volume of compounds in the chamber, and in turn, reducing the volume of vapor generated. As such, in the final set of theoretical calculations, the number of evaporation dishes (N) in Eq. 3.4 was reduced at each time point before calculation of the vapor load in Eq. 2.5.

As expected, the maximum volume of vapor generated by each compound was reduced when dish removal was taken into account (Figure 2.2C). However, the extent of reduction was dependent on the volatility of the compound. For 2-methylbutane ($I^T = 487$), the maximum vapor load was 0.237 %v/v when accounting only for air flow (Figure 2.2B). When incorporating both air flow and the removal of dishes, the maximum vapor load was 0.167 %v/v, which represents a 30% decrease (Figure 2.2C). In contrast, for *n*-octane ($I^T = 800$), the maximum vapor load was reduced from 0.0734 to 0.0217 %v/v when accounting for dish removal, representing a 70% decrease (Figures 2.2B and C). Moreover, the time to reach the maximum vapor load was also reduced for less volatile compounds such as *n*-octane, which decreased from 9.1 h to 5.1 h when accounting for dish removal. Overall, less volatile compounds were significantly affected, while

more volatile compounds were less affected by dish removal because they reached their maximum vapor load before a significant number of dishes were removed.

2.4 Conclusions

With these calculations, the theoretical volume of vapor generated by each compound during the evaporation was determined. These calculations were necessary to identify binary combinations of compounds that could be safely evaporated. As the diluted vapor volume did not exceed 0.18 %v/v for any compound, any binary mixture of compounds would not exceed an additive diluted vapor of 0.36 %v/v. This value is well below the LFL for any two-compound combination, leading to increased confidence that these mixtures could be evaporated safely.

APPENDIX

Table A2.1. Maximum vapor load (%v/v) and time of occurrence predicted for *n*-butane as a function of temperature, flow rate, volume, and number of dishes.

I^T	Temperature (°C)	Flow Rate (mL/min)	Volume (mL)	Dishes	Maximum Vapor Load (%v/v) _{max}	Time (h) at (%v/v) _{max}
400	40	30	0.10	18	1.188	0.1
400	40	30	0.075	18	0.891	0.1
400	40	30	0.05	18	0.594	0.1
400	40	30	0.025	18	0.297	0.1
400	40	60	0.10	18	1.182	0.1
400	40	60	0.075	18	0.886	0.1
400	40	60	0.05	18	0.591	0.1
400	40	60	0.025	18	0.295	0.1
400	40	90	0.10	18	1.175	0.1
400	40	90	0.075	18	0.881	0.1
400	40	90	0.05	18	0.588	0.1
400	40	90	0.025	18	0.294	0.1
400	40	120	0.10	18	1.169	0.1
400	40	120	0.075	18	0.877	0.1
400	40	120	0.05	18	0.585	0.1
400	40	120	0.025	18	0.292	0.1
400	30	30	0.10	18	1.144	0.2
400	30	30	0.075	18	0.858	0.2
400	30	30	0.05	18	0.572	0.2
400	30	30	0.025	18	0.286	0.2
400	30	60	0.10	18	1.132	0.2
400	30	60	0.075	18	0.849	0.2
400	30	60	0.05	18	0.566	0.2
400	30	60	0.025	18	0.283	0.2
400	30	90	0.10	18	1.121	0.2
400	30	90	0.075	18	0.841	0.2
400	30	90	0.05	18	0.560	0.2
400	30	90	0.025	18	0.280	0.2
400	30	120	0.10	18	1.109	0.2
400	30	120	0.075	18	0.832	0.2
400	30	120	0.05	18	0.555	0.2
400	30	120	0.025	18	0.277	0.2
400	20	30	0.10	18	1.096	0.4

Table A2.1. (cont'd)

400	20	30	0.075	18	0.822	0.4
400	20	30	0.05	18	0.548	0.4
400	20	30	0.025	18	0.274	0.4
400	20	60	0.10	18	1.076	0.3
400	20	60	0.075	18	0.807	0.3
400	20	60	0.05	18	0.538	0.3
400	20	60	0.025	18	0.269	0.3
400	20	90	0.10	18	1.061	0.3
400	20	90	0.075	18	0.795	0.3
400	20	90	0.05	18	0.530	0.3
400	20	90	0.025	18	0.265	0.3
400	20	120	0.10	18	1.045	0.3
400	20	120	0.075	18	0.784	0.3
400	20	120	0.05	18	0.523	0.3
400	20	120	0.025	18	0.261	0.3
400	10	30	0.10	18	1.040	0.7
400	10	30	0.075	18	0.780	0.7
400	10	30	0.05	18	0.520	0.7
400	10	30	0.025	18	0.260	0.7
400	10	60	0.10	18	1.009	0.6
400	10	60	0.075	18	0.757	0.6
400	10	60	0.05	18	0.505	0.6
400	10	60	0.025	18	0.252	0.6
400	10	90	0.10	18	0.982	0.6
400	10	90	0.075	18	0.737	0.6
400	10	90	0.05	18	0.491	0.6
400	10	90	0.025	18	0.246	0.6
400	10	120	0.10	18	0.960	0.5
400	10	120	0.075	18	0.720	0.5
400	10	120	0.05	18	0.480	0.5
400	10	120	0.025	18	0.240	0.5

Table A2.2. Maximum vapor load (%v/v) and time of occurrence predicted for *n*-pentane as a function of temperature, flow rate, volume, and number of dishes.

I^T	Temperature (°C)	Flow Rate (mL/min)	Volume (mL)	Dishes	Maximum Vapor Load (%v/v) _{max}	Time (h) at (%v/v) _{max}
500	40	30	0.10	18	1.196	0.3
500	40	30	0.075	18	0.897	0.3
500	40	30	0.05	18	0.598	0.3
500	40	30	0.025	18	0.299	0.3
500	40	60	0.10	18	1.178	0.3
500	40	60	0.075	18	0.883	0.3
500	40	60	0.05	18	0.589	0.3
500	40	60	0.025	18	0.294	0.3
500	40	90	0.10	18	1.165	0.2
500	40	90	0.075	18	0.874	0.2
500	40	90	0.05	18	0.582	0.2
500	40	90	0.025	18	0.291	0.2
500	40	120	0.10	18	1.153	0.2
500	40	120	0.075	18	0.865	0.2
500	40	120	0.05	18	0.577	0.2
500	40	120	0.025	18	0.288	0.2
500	30	30	0.10	18	1.145	0.5
500	30	30	0.075	18	0.859	0.5
500	30	30	0.05	18	0.572	0.5
500	30	30	0.025	18	0.286	0.5
500	30	60	0.10	18	1.120	0.4
500	30	60	0.075	18	0.840	0.4
500	30	60	0.05	18	0.560	0.4
500	30	60	0.025	18	0.280	0.4
500	30	90	0.10	18	1.099	0.4
500	30	90	0.075	18	0.824	0.4
500	30	90	0.05	18	0.550	0.4
500	30	90	0.025	18	0.275	0.4
500	30	120	0.10	18	1.079	0.4
500	30	120	0.075	18	0.809	0.4
500	30	120	0.05	18	0.539	0.4
500	30	120	0.025	18	0.270	0.4
500	20	30	0.10	18	1.084	0.9
500	20	30	0.075	18	0.813	0.9

Table A2.2. (cont'd)

500	20	30	0.05	18	0.542	0.9
500	20	30	0.025	18	0.271	0.9
500	20	60	0.10	18	1.046	0.7
500	20	60	0.075	18	0.784	0.7
500	20	60	0.05	18	0.523	0.7
500	20	60	0.025	18	0.261	0.7
500	20	90	0.10	18	1.015	0.7
500	20	90	0.075	18	0.761	0.7
500	20	90	0.05	18	0.507	0.7
500	20	90	0.025	18	0.254	0.7
500	20	120	0.10	18	0.987	0.6
500	20	120	0.075	18	0.740	0.6
500	20	120	0.05	18	0.493	0.6
500	20	120	0.025	18	0.247	0.6
500	10	30	0.10	18	1.008	1.6
500	10	30	0.075	18	0.756	1.6
500	10	30	0.05	18	0.504	1.6
500	10	30	0.025	18	0.252	1.6
500	10	60	0.10	18	0.950	1.3
500	10	60	0.075	18	0.712	1.3
500	10	60	0.05	18	0.475	1.3
500	10	60	0.025	18	0.237	1.3
500	10	90	0.10	18	0.904	1.2
500	10	90	0.075	18	0.678	1.2
500	10	90	0.05	18	0.452	1.2
500	10	90	0.025	18	0.226	1.2
500	10	120	0.10	18	0.865	1.1
500	10	120	0.075	18	0.649	1.1
500	10	120	0.05	18	0.432	1.1
500	10	120	0.025	18	0.216	1.1

Table A2.3. Maximum vapor load (%v/v) and time of occurrence predicted for *n*-hexane as a function of temperature, flow rate, volume, and number of dishes.

I^r	Temperature (°C)	Flow Rate (mL/min)	Volume (mL)	Dishes	Maximum Vapor Load (%v/v) _{max}	Time (h) at (%v/v) _{max}
600	40	30	0.10	18	1.026	0.6
600	40	30	0.075	18	0.770	0.6
600	40	30	0.05	18	0.513	0.6
600	40	30	0.025	18	0.257	0.6
600	40	60	0.10	18	0.998	0.6
600	40	60	0.075	18	0.749	0.6
600	40	60	0.05	18	0.499	0.6
600	40	60	0.025	18	0.250	0.6
600	40	90	0.10	18	0.975	0.5
600	40	90	0.075	18	0.731	0.5
600	40	90	0.05	18	0.488	0.5
600	40	90	0.025	18	0.244	0.5
600	40	120	0.10	18	0.953	0.5
600	40	120	0.075	18	0.715	0.5
600	40	120	0.05	18	0.477	0.5
600	40	120	0.025	18	0.238	0.5
600	30	30	0.10	18	0.970	1.1
600	30	30	0.075	18	0.727	1.1
600	30	30	0.05	18	0.485	1.1
600	30	30	0.025	18	0.242	1.1
600	30	60	0.10	18	0.928	0.9
600	30	60	0.075	18	0.696	0.9
600	30	60	0.05	18	0.464	0.9
600	30	60	0.025	18	0.232	0.9
600	30	90	0.10	18	0.894	0.8
600	30	90	0.075	18	0.670	0.8
600	30	90	0.05	18	0.447	0.8
600	30	90	0.025	18	0.223	0.8
600	30	120	0.10	18	0.865	0.8
600	30	120	0.075	18	0.648	0.8
600	30	120	0.05	18	0.432	0.8
600	30	120	0.025	18	0.216	0.8
600	20	30	0.10	18	0.898	1.9
600	20	30	0.075	18	0.673	1.9

Table A2.3. (cont'd)

600	20	30	0.05	18	0.449	1.9
600	20	30	0.025	18	0.224	1.9
600	20	60	0.10	18	0.837	1.6
600	20	60	0.075	18	0.628	1.6
600	20	60	0.05	18	0.418	1.6
600	20	60	0.025	18	0.209	1.6
600	20	90	0.10	18	0.790	1.4
600	20	90	0.075	18	0.592	1.4
600	20	90	0.05	18	0.395	1.4
600	20	90	0.025	18	0.197	1.4
600	20	120	0.10	18	0.750	1.3
600	20	120	0.075	18	0.563	1.3
600	20	120	0.05	18	0.375	1.3
600	20	120	0.025	18	0.188	1.3
600	10	30	0.10	18	0.802	3.4
600	10	30	0.075	18	0.602	3.4
600	10	30	0.05	18	0.401	3.4
600	10	30	0.025	18	0.201	3.4
600	10	60	0.10	18	0.717	2.7
600	10	60	0.075	18	0.538	2.7
600	10	60	0.05	18	0.359	2.7
600	10	60	0.025	18	0.179	2.7
600	10	90	0.10	18	0.656	2.4
600	10	90	0.075	18	0.492	2.4
600	10	90	0.05	18	0.328	2.4
600	10	90	0.025	18	0.164	2.4
600	10	120	0.10	18	0.608	2.1
600	10	120	0.075	18	0.456	2.1
600	10	120	0.05	18	0.304	2.1
600	10	120	0.025	18	0.152	2.1

Table A2.4. Maximum vapor load (%v/v) and time of occurrence predicted for *n*-heptane as a function of temperature, flow rate, volume, and number of dishes.

I^r	Temperature (°C)	Flow Rate (mL/min)	Volume (mL)	Dishes	Maximum Vapor Load (%v/v) _{max}	Time (h) at (%v/v) _{max}
700	40	30	0.10	18	0.883	1.5
700	40	30	0.075	18	0.662	1.5
700	40	30	0.05	18	0.441	1.5
700	40	30	0.025	18	0.221	1.5
700	40	60	0.10	18	0.835	1.2
700	40	60	0.075	18	0.627	1.2
700	40	60	0.05	18	0.418	1.2
700	40	60	0.025	18	0.209	1.2
700	40	90	0.10	18	0.797	1.1
700	40	90	0.075	18	0.598	1.1
700	40	90	0.05	18	0.399	1.1
700	40	90	0.025	18	0.199	1.1
700	40	120	0.10	18	0.765	1.0
700	40	120	0.075	18	0.574	1.0
700	40	120	0.05	18	0.383	1.0
700	40	120	0.025	18	0.191	1.0
700	30	30	0.10	18	0.812	2.4
700	30	30	0.075	18	0.609	2.4
700	30	30	0.05	18	0.406	2.4
700	30	30	0.025	18	0.203	2.4
700	30	60	0.10	18	0.746	2.0
700	30	60	0.075	18	0.559	2.0
700	30	60	0.05	18	0.373	2.0
700	30	60	0.025	18	0.186	2.0
700	30	90	0.10	18	0.696	1.7
700	30	90	0.075	18	0.522	1.7
700	30	90	0.05	18	0.348	1.7
700	30	90	0.025	18	0.174	1.7
700	30	120	0.10	18	0.655	1.6
700	30	120	0.075	18	0.491	1.6
700	30	120	0.05	18	0.328	1.6
700	30	120	0.025	18	0.164	1.6
700	20	30	0.10	18	0.720	4.0
700	20	30	0.075	18	0.540	4.0

Table A2.4. (cont'd)

700	20	30	0.05	18	0.360	4.0
700	20	30	0.025	18	0.180	4.0
700	20	60	0.10	18	0.632	3.2
700	20	60	0.075	18	0.474	3.2
700	20	60	0.05	18	0.316	3.2
700	20	60	0.025	18	0.158	3.2
700	20	90	0.10	18	0.571	2.8
700	20	90	0.075	18	0.428	2.8
700	20	90	0.05	18	0.285	2.8
700	20	90	0.025	18	0.143	2.8
700	20	120	0.10	18	0.524	2.5
700	20	120	0.075	18	0.393	2.5
700	20	120	0.05	18	0.262	2.5
700	20	120	0.025	18	0.131	2.5
700	10	30	0.10	18	0.601	6.7
700	10	30	0.075	18	0.451	6.7
700	10	30	0.05	18	0.300	6.7
700	10	30	0.025	18	0.150	6.7
700	10	60	0.10	18	0.495	5.2
700	10	60	0.075	18	0.371	5.2
700	10	60	0.05	18	0.247	5.2
700	10	60	0.025	18	0.124	5.2
700	10	90	0.10	18	0.427	4.4
700	10	90	0.075	18	0.321	4.4
700	10	90	0.05	18	0.214	4.4
700	10	90	0.025	18	0.107	4.4
700	10	120	0.10	18	0.379	3.8
700	10	120	0.075	18	0.284	3.8
700	10	120	0.05	18	0.190	3.8
700	10	120	0.025	18	0.095	3.8

Table A2.5. Maximum vapor load (%v/v) and time of occurrence predicted for *n*-octane as a function of temperature, flow rate, volume, and number of dishes.

I^T	Temperature (°C)	Flow Rate (mL/min)	Volume (mL)	Dishes	Maximum Vapor Load (%v/v) _{max}	Time (h) at (%v/v) _{max}
800	40	30	0.10	18	0.728	3.1
800	40	30	0.075	18	0.546	3.1
800	40	30	0.05	18	0.364	3.1
800	40	30	0.025	18	0.182	3.1
800	40	60	0.10	18	0.655	2.5
800	40	60	0.075	18	0.492	2.5
800	40	60	0.05	18	0.328	2.5
800	40	60	0.025	18	0.164	2.5
800	40	90	0.10	18	0.602	2.2
800	40	90	0.075	18	0.452	2.2
800	40	90	0.05	18	0.301	2.2
800	40	90	0.025	18	0.151	2.2
800	40	120	0.10	18	0.560	2.0
800	40	120	0.075	18	0.420	2.0
800	40	120	0.05	18	0.280	2.0
800	40	120	0.025	18	0.140	2.0
800	30	30	0.10	18	0.638	5.0
800	30	30	0.075	18	0.478	5.0
800	30	30	0.05	18	0.319	5.0
800	30	30	0.025	18	0.159	5.0
800	30	60	0.10	18	0.547	3.9
800	30	60	0.075	18	0.410	3.9
800	30	60	0.05	18	0.274	3.9
800	30	60	0.025	18	0.137	3.9
800	30	90	0.10	18	0.486	3.3
800	30	90	0.075	18	0.364	3.3
800	30	90	0.05	18	0.243	3.3
800	30	90	0.025	18	0.121	3.3
800	30	120	0.10	18	0.440	3.0
800	30	120	0.075	18	0.330	3.0
800	30	120	0.05	18	0.220	3.0
800	30	120	0.025	18	0.110	3.0
800	20	30	0.10	18	0.526	7.9
800	20	30	0.075	18	0.395	7.9

Table A2.5. (cont'd)

800	20	30	0.05	18	0.263	7.9
800	20	30	0.025	18	0.132	7.9
800	20	60	0.10	18	0.423	6.0
800	20	60	0.075	18	0.317	6.0
800	20	60	0.05	18	0.211	6.0
800	20	60	0.025	18	0.106	6.0
800	20	90	0.10	18	0.359	5.0
800	20	90	0.075	18	0.269	5.0
800	20	90	0.05	18	0.180	5.0
800	20	90	0.025	18	0.090	5.0
800	20	120	0.10	18	0.315	4.4
800	20	120	0.075	18	0.236	4.4
800	20	120	0.05	18	0.157	4.4
800	20	120	0.025	18	0.079	4.4
800	10	30	0.10	18	0.397	12.5
800	10	30	0.075	18	0.298	12.5
800	10	30	0.05	18	0.198	12.5
800	10	30	0.025	18	0.099	12.5
800	10	60	0.10	18	0.293	9.1
800	10	60	0.075	18	0.220	9.1
800	10	60	0.05	18	0.147	9.1
800	10	60	0.025	18	0.073	9.1
800	10	90	0.10	18	0.237	7.4
800	10	90	0.075	18	0.178	7.4
800	10	90	0.05	18	0.118	7.4
800	10	90	0.025	18	0.059	7.4
800	10	120	0.10	18	0.200	6.3
800	10	120	0.075	18	0.150	6.3
800	10	120	0.05	18	0.100	6.3
800	10	120	0.025	18	0.050	6.3

REFERENCES

REFERENCES

- [1] J.W. McIlroy, A.D. Jones, V.L. McGuffin, Gas chromatographic retention index as a basis for predicting evaporation rates of complex mixtures. *Analytica Chimica Acta* **2014**, *852*, 257-266.
- [2] J.W. McIlroy, R. Waddell Smith, V.L. McGuffin, Fixed- and variable-temperature kinetic models to predict evaporation of petroleum distillates for fire debris applications. *Separations* **2018**, *5* (47), 1-19.
- [3] C.J.R. Coronado, J.A. Carvalho Jr., J.C. Andrade, E.V. Cortez, F.S. Carvalho, J.C. Santos, A.Z. Mendiburu. Flammability limits: A review with emphasis on ethanol for aeronautical applications and description of the experimental procedure, *Journal of Hazardous Materials* **2012**, 241-242, 32-54.
- [4] N.K. Eklund, B.A. Capistran, V.L. McGuffin, R. Waddell Smith, Improvements in a kinetic-based model to predict evaporation of gasoline. *Forensic Chemistry* **2020**, *17*, 100194.

III. Measuring Evaporation Rate Constants of Highly Volatile Compounds for Kinetic Models

3.1 Introduction

The kinetic model was previously developed using diesel with a retention index (I^T) range that began with 800 (*n*-octane) and spanned to around 1200 (*n*-dodecane) or 1400 (*n*-tetradecane), depending on the given temperature [1,2]. While this I^T range was appropriate for the environmental applications for which the model was designed, the forensic application to fire debris analysis requires that the model be extended to include lower I^T values, corresponding to more volatile compounds. For example, gasoline is a common accelerant used in intentional fires and includes compounds as volatile as butane ($I^T = 400$). For this reason, the aim in this chapter is to describe the extension and refinement of the kinetic model to include more volatile compounds, specifically over the range $I^T = 486 - 800$.

In Chapter 2, theoretical calculations were performed to ensure that the vapor generated during the evaporative process remained below the lower flammability limit for any given compound. However, in addition to maintaining safety, there are other experimental considerations when measuring evaporation rate constants of volatile compounds. First, because evaporation occurs rapidly, samples must be collected at early and frequent time points. Whereas the evaporations in the original development of the model by McIlroy *et al.* included nine time points over the span of 300 h [1], most of the volatile compounds of interest in this work require less than 9 h to fully evaporate. For this reason, the early time points must be close together, requiring rapid sample preparation methods to minimize additional evaporation.

The second issue to overcome in this work is the efficient removal of vapors from the chamber during the evaporation. Because of the closeness of time points and the short evaporation time, vapors can condense back into the evaporation dishes if not properly removed

from the chamber. This introduces error because the measured quantity of compound in any given dish is equal to the sum of the true fraction remaining due to evaporation and the fraction of vapor condensing after evaporation. This chapter explores ways to quantify this problem and employs a correction method to account for condensation.

3.2 Materials and Methods

3.2.1 Standard Preparation

A total of 12 compounds eluting in the range $I^T = 400 - 800$ were selected for this study and included normal, branched, and cyclic alkanes, as well as aromatic compounds. Reference standards for the 12 compounds (2-methylbutane, *n*-pentane, 3-methylpentane, *n*-hexane, methylcyclopentane, 2,3-dimethylpentane, 2-methylhexane, *n*-heptane, 2,2,4-trimethylpentane, methylcyclohexane, toluene, and *n*-octane) were purchased from Sigma-Aldrich (St. Louis, MO, USA) for experimental evaporations. Upon receiving, each standard was analyzed individually by gas chromatography-mass spectrometry (GC-MS) to determine the retention time of the compound and to generate the mass spectrum.

Based on the theoretical calculations in Chapter 2, the compounds were prepared as binary mixtures, rather than a multi-component mixture, to reduce overall compound volume when evaporated. To prepare each mixture, 0.625 mL of each of the two compounds were diluted to 25 mL with *n*-tetradecane (C₁₄, Sigma-Aldrich), with 1 mL of *n*-tridecane (C₁₃, Sigma-Aldrich) added as an internal standard.

A validation mixture containing nine compounds (six new compounds and three compounds included in model development) was used to assess the predictive accuracy of the model. The validation mixture was prepared by adding 2-methylpentane (2 mL), 2,4-dimethylpentane (1 mL), cyclohexane (2 mL), 3-methylhexane (1 mL), *n*-heptane (2 mL), 2,3,4-

trimethylpentane (1 mL), toluene (2 mL), cycloheptane (1 mL), and *n*-octane (2 mL) into a mixture containing *n*-decane (3 mL) as the solvent and *n*-tridecane (3 mL) as the internal standard (all Sigma-Aldrich).

To calculate retention indices, an alkane ladder was prepared by diluting *n*-pentane, *n*-hexane, *n*-heptane, and *n*-octane (Sigma-Aldrich, all 300:1 v/v) in dichloromethane (CH₂Cl₂, ACS grade, Macron Fine Chemicals, Darmstadt, Germany).

3.2.2 Experimental Evaporations

An evaporation chamber previously built in-house and described in detail by McIlroy *et al.* [1] was utilized for all evaporations. Briefly, the chamber consisted of an internal box (total volume 33.4 L) in which the evaporation dishes were placed. This box isolated the flammable vapors from electronic and heating/cooling components, which could serve as an ignition source. The box was housed within an Ambi-Hi-Lo incubator (Model 3550DT, Lab-Line, Melrose Park, IL, USA) with temperatures recorded using a temperature probe data logger (Model TR-74Ui, T&D Corp., Matsumoto, Japan). High-purity air (Airgas, Radnor Township, PA, USA) was sparged through distilled water to provide constant humidity and then flowed into the chamber from beneath the evaporation dishes to carry vapors upward towards the outlet. A peristaltic pump (Masterflex L/S drive, model 07555-00, with L/S Easy Load pump head, model 77200-62, Cole-Parmer, Vernon Hills, IL, USA) with viton tubing (Cole-Parmer) circulated air throughout the chamber. The exiting vapor flowed through a copper tube (12 in x 0.5 in OD x 0.37 in ID) filled with activated carbon (6 – 14 mesh, Fisher Scientific, Waltham, MA, USA) to adsorb and, thereby, remove volatiles before being recirculated back into the chamber.

For model development, each binary mixture was evaporated in duplicate at three different temperatures (10, 20, and 30 °C). A 1-mL aliquot of the mixture was added to each of

18 petri dishes (60 mm ID x 15 mm) using a gas-tight syringe (Hamilton Company, Reno, NV, USA). Throughout the evaporation, petri dishes were removed at nine specific time points. The selection of time points was based on the time at which τ would be achieved for the least volatile compound, *n*-octane (*i.e.*, $\tau = 9.3 \text{ h} = 558 \text{ min}$ at $10 \text{ }^\circ\text{C}$), which became the final time point. The other eight time points were calculated such that they increased exponentially (*i.e.*, 5, 8, 15, 28, 51, 92, 168, and 306 min at $10 \text{ }^\circ\text{C}$) until reaching the final time point. This approach ensured that all compounds achieved at least time τ in their kinetic decay curve (Eq. 2.2) during the given time frame at each temperature. On removal from the chamber, a series of 1-mL aliquots of CH_2Cl_2 was pipetted into the petri dish, the mixture was transferred into a 5-mL volumetric flask, and further diluted to the mark with CH_2Cl_2 . Evaporated samples were then transferred to GC vials and analyzed in triplicate by GC-MS.

For the validation study, the validation mixture was evaporated to three F_{Total} levels at $10 \text{ }^\circ\text{C}$ and five F_{Total} levels at 20 and $30 \text{ }^\circ\text{C}$. A 1-mL aliquot of the validation mixture was delivered into three separate petri dishes using a gas-tight syringe. The petri dishes were placed in the evaporation chamber and removed at time points corresponding to $F_{Total} = 0.3$ to 0.8 . A level of $F_{Total} = 0.3$ corresponds to 70% evaporation, whereas $F_{Total} = 0.8$ corresponds to 20% evaporation. These relatively high levels were necessary to ensure that the validation compounds remained present at sufficient abundance to evaluate the predictive accuracy of the model. On removal from the chamber, the evaporated samples were diluted 50:1 (v/v) with CH_2Cl_2 , transferred to GC vials, and analyzed in triplicate by GC-MS.

3.2.3 Gas Chromatography-Mass Spectrometry Analysis

The GC-MS system consisted of an Agilent 6890N gas chromatograph coupled to an Agilent 5975C mass spectrometer with an Agilent 7683A injector (Agilent Technologies, Santa

Clara, CA, USA). The GC contained a 100%-dimethylpolysiloxane column (30 m x 0.25 mm ID x 0.25 μm film thickness, Agilent Technologies). The injection temperature was 250 $^{\circ}\text{C}$ and 1 μL of sample was injected in pulsed split mode (15 psi for 0.25 min, 50:1 split). Ultra-high purity helium (Airgas) was used as the carrier gas with a nominal flow rate of 1 mL/min. The oven temperature program was as follows: initial temperature 35 $^{\circ}\text{C}$ with linear ramp at 5 $^{\circ}\text{C}/\text{min}$ to 175 $^{\circ}\text{C}$. The transfer line was maintained at 280 $^{\circ}\text{C}$. Electron ionization was employed at 70 eV and the mass spectral scan range was m/z 40 – 550, with a scan rate of 2.83 scans/s. The temperature of the ion source was 230 $^{\circ}\text{C}$, while the temperature of the quadrupole mass analyzer was 150 $^{\circ}\text{C}$. To detect the early eluting volatile compounds, no solvent delay was used but the detector was turned off during elution of CH_2Cl_2 (1.62 – 1.80 min).

3.2.4 Retention Index Calculations

The retention index for each compound was determined by comparing the retention time of the compound when injected individually to the retention times of n -alkanes in an alkane ladder. To calculate the retention index under temperature-programmed conditions (I^T), Eq. 3.1 was used

$$I^T = 100 \left[\frac{t_{R,i}^T - t_{R,z}^T}{t_{R,z+1}^T - t_{R,z}^T} + z \right] \quad (3.1)$$

where $t_{R,i}^T$ is the retention time of the compound of interest, and $t_{R,z}^T$ and $t_{R,z+1}^T$ are the retention times of the n -alkanes of carbon number, z , eluting before and after the compound of interest.

3.2.5 Data Analysis

The identity of each compound in the binary mixtures was confirmed through retention time comparison to chromatograms of individual reference compounds, as well as through the comparison of mass spectra. The chromatographic data were exported from ChemStation

(version E.01.00.237, Agilent Technologies) into Microsoft Excel (version 16.20, Microsoft Corp., Redmond, WA, USA) for further processing.

The peak abundance of each compound in the evaporated binary mixtures was first normalized to the peak abundance of the internal standard. For each compound, the normalized abundance was then plotted *versus* evaporation time to generate a decay curve. Each decay curve was fit to the first-order rate equation (Eq. 2.2) by non-linear regression (TableCurve 2D, version 5.01, Jandel Scientific, San Rafael, CA, USA), from which k was determined for each compound. The natural logarithm of k was then plotted as a function of I^T and combined with data from the original model [1, 2] to generate a regression model (Eq. 3.2).

$$\ln(k) = m_1 I^T + b \quad (3.2)$$

This procedure was repeated for the evaporations conducted at each temperature to generate fixed-temperature models at 10, 20, and 30 °C.

The models were then used to predict chromatograms corresponding to each F_{Total} level of the validation mixture. To do so, the experimental F_{Total} of each evaporated validation mixture was calculated by dividing the area of the chromatogram in the range $I^T = 500 - 800$ by the area of the chromatogram of the unevaporated validation mixture over the same I^T range. Then, Eq. 3.2 was combined with Eq. 2.2 and t was varied to generate the fraction-remaining curve corresponding to the same experimental F_{Total} level. Finally, the fraction-remaining curve was multiplied by the chromatogram of the unevaporated validation mixture to generate the predicted chromatogram at the same F_{Total} level.

To assess similarity between the predicted and experimental chromatograms, Pearson product-moment correlation (PPMC) coefficients (r) were calculated across the range $I^T = 500 - 800$, according to Eq. 3.3

$$r = \frac{\sum[(A_{I^T,pred} - \bar{A}_{pred})(A_{I^T,exp} - \bar{A}_{exp})]}{\sqrt{\sum(A_{I^T,pred} - \bar{A}_{pred})^2 \sum(A_{I^T,exp} - \bar{A}_{exp})^2}} \quad (3.3)$$

where $A_{I^T,pred}$ and $A_{I^T,exp}$ are the predicted and experimental abundances at each I^T value, and \bar{A}_{pred} and \bar{A}_{exp} are the average predicted and experimental abundances. PPMC coefficients range from -1 to +1, where -1 indicates a perfect negative correlation and +1 indicates a perfect positive correlation. The strength of the correlation is then defined as follows: $|r| \geq 0.8$ indicates strong correlation, $0.8 > |r| \geq 0.5$ indicates moderate correlation, $|r| < 0.5$ indicates weak correlation, and r close to zero indicates no correlation [3].

To evaluate the predictive accuracy of the model, the predicted and experimental peak abundances were compared for individual compounds in the validation mixture and the percent error (E) was calculated.

$$E = \frac{A_{I^T,pred} - A_{I^T,exp}}{A_{I^T,exp}} \times 100 \quad (3.4)$$

When calculated this way, the sign in the error indicates whether the model overpredicted (positive) or underpredicted (negative) the abundance of each compound in the validation mixture. Following the percent error calculations for individual compounds, the mean absolute percent error (MAPE or \bar{E}) was calculated

$$\bar{E} = \frac{\sum_1^n \left| \frac{A_{I^T,pred} - A_{I^T,exp}}{A_{I^T,exp}} \right|}{n} \times 100 \quad (3.5)$$

where n is the total number of compounds.

3.3 Results

3.3.1 Refinement and Validation of the Fixed-Temperature Model at 10 °C

Six binary mixtures of volatile compounds were evaporated in the chamber to experimentally determine the evaporation rate constants. For each mixture, 18 petri dishes

containing the mixture were placed in the chamber and two dishes were removed at each of nine time points during the nine-hour evaporation. Representative decay curves for the *n*-alkanes in the range $T = 500 - 800$ (*n*-pentane, *n*-hexane, *n*-heptane, and *n*-octane) are shown in Figure 3.1, with the experimentally determined evaporation rate constants underlined in the figure legend. The most volatile *n*-alkane studied, *n*-pentane, exhibited the poorest quality of fit to the first-order kinetic rate equation with $R^2 = 0.8793$. For this compound, all data points after 0.5 h fall above the line of fit. While the quality of fit is improved for *n*-hexane ($R^2 = 0.9485$), all data points after 1 h still fall above the line of fit for the first-order kinetic equation. The quality of fit is improved as volatility decreases, as demonstrated by the spread of data points around the regression line for *n*-heptane and *n*-octane. At nearly every time point, there are data points both above and below the line of fit, indicating a better-quality regression.

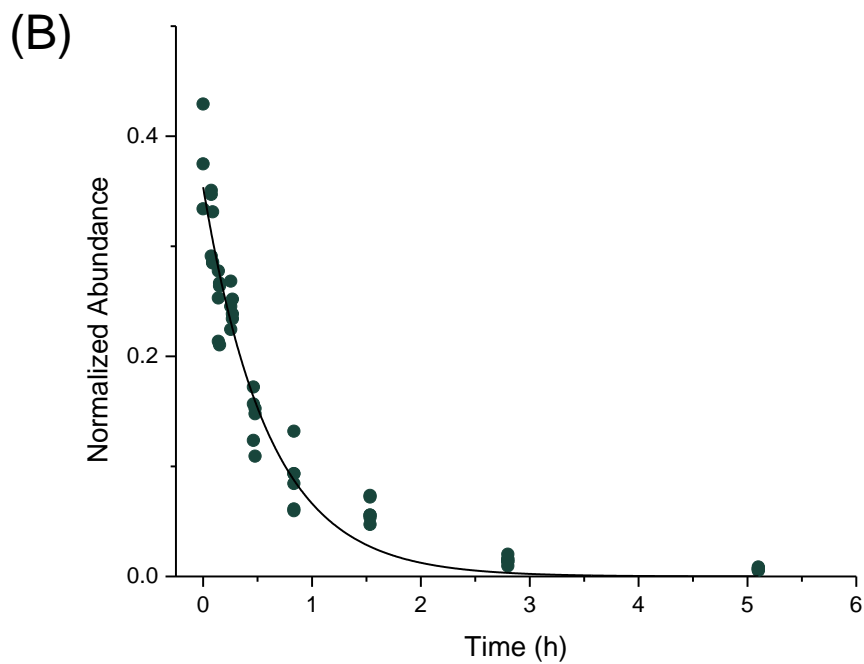
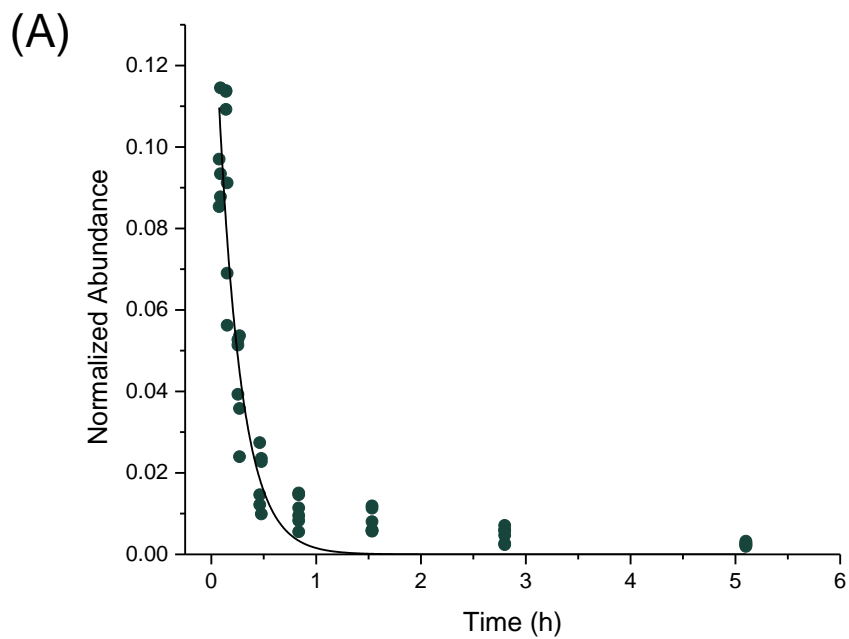
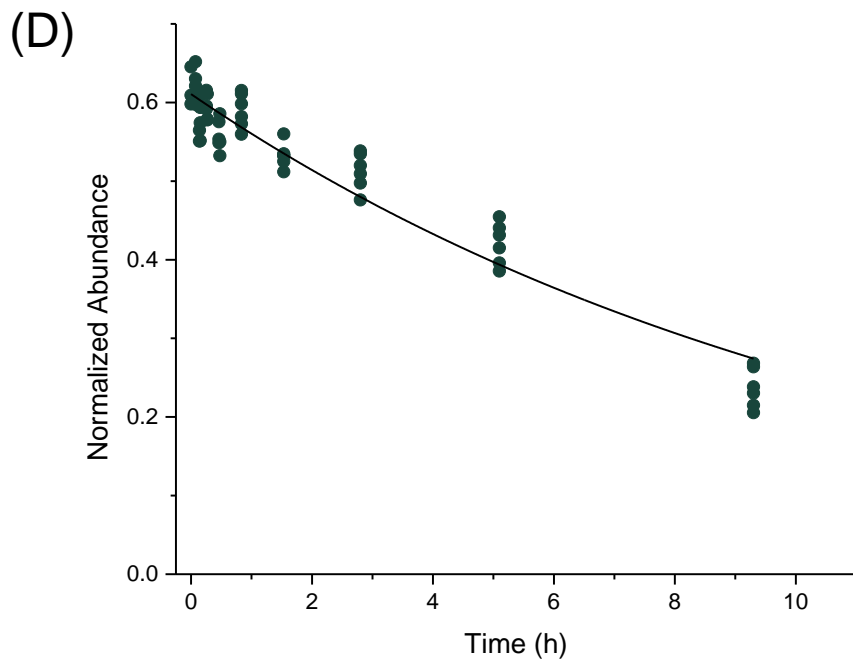
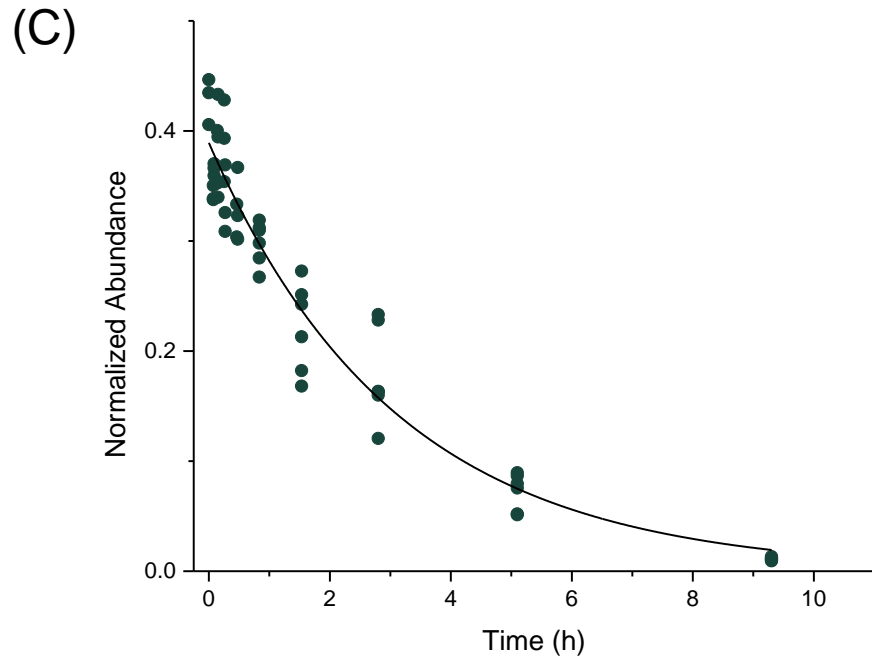


Figure 3.1. Normalized abundances of (A) *n*-pentane, (B) *n*-hexane, (C) *n*-heptane, and (D) *n*-octane as a function of evaporation time. Linear regression equations: *n*-pentane: $C_t = 0.155 * \exp(-4.602 * t)$, $R^2 = 0.8793$; *n*-hexane: $C_t = 0.354 * \exp(-1.674 * t)$, $R^2 = 0.9485$; *n*-heptane: $C_t = 0.389 * \exp(-0.323 * t)$, $R^2 = 0.9437$; *n*-octane: $C_t = 0.611 * \exp(-0.0861 * t)$, $R^2 = 0.9250$

Figure 3.1. (cont'd)



The evaporation rate constants in the range $I^T = 500 - 800$ for the *n*-alkanes spanned several orders of magnitude. For the most volatile *n*-alkane investigated, *n*-pentane ($I^T = 500$), the experimentally determined evaporation rate constant was 4.602 h^{-1} . The measured rate constant for the *n*-alkane with a difference in I^T of 200 (*n*-heptane, $I^T = 700$) was 0.323 h^{-1} . This represents approximately a one order-of-magnitude difference in evaporation rate constant with the addition of two methylene groups, consistent with the previous findings of McIlroy *et al.* [1,2]. While McIlroy *et al.* experimentally determined k for a different set of compounds, the consistency in the rate constants can be evaluated based on the difference in rate constant as a function of retention index difference.

Given the demonstrated consistency in measurements, the retention indices and the experimentally determined evaporation rate constants for the compounds in this study (Table 3.1) were combined with those determined previously for 46 compounds spanning the retention index range $I^T = 800 - 1200$ at $10 \text{ }^\circ\text{C}$ [2].

Table 3.1. Evaporation Rate Constants for Selected Compounds at $10 \text{ }^\circ\text{C}$

Compound	I^T	Evaporation Rate Constant (h^{-1})	R^2
2-Methylbutane	487	8.999	0.8605
<i>n</i> -Pentane	500	4.602	0.8793
3-Methylpentane	578	1.744	0.9682
<i>n</i> -Hexane	600	1.674	0.9485
Methylcyclopentane	621	1.255	0.9317
2-Methylhexane	659	0.584	0.9588
2,3-Dimethylpentane	661	0.539	0.9498
2,2,4-Trimethylpentane	686	0.414	0.9584
<i>n</i> -Heptane	700	0.323	0.9477
Methylcyclohexane	716	0.351	0.9584
Toluene	747	0.246	0.9707
<i>n</i> -Octane	800	0.0861	0.9250

The natural logarithm of the rate constant was plotted *versus* I^T for each compound (Figure 3.2) and linear regression was performed to define the kinetic model, as shown in Eq. 3.6.

$$\ln(k) = -1.12 \times 10^{-2}I^T + 6.93 \quad (3.6)$$

The extended model in Eq. 3.6 now spans the range $I^T = 500 - 1200$ and the high quality of fit is demonstrated with the square of the correlation coefficient (R^2) of 0.9889. Most compounds are close to the regression line (Figure 3.2), with the exception of two compounds that have larger residuals: 2-methylbutane ($I^T = 487$) and *n*-octane ($I^T = 800$). While the mean absolute percent error (MAPE) in predicting the rate constants of compounds with $I^T \leq 800$ for the refined model is 24%, the individual errors for 2-methylbutane and *n*-octane are -106% and 35%, respectively. When comparing the predicted and experimental rate constants using Eq. 3.4, a negative sign indicates underprediction, whereas a positive sign indicates overprediction. Omitting these two compounds, the MAPE is 15%, which is close to the MAPE of 10.8% reported by McIlroy *et al.* for the fixed-temperature model at 10 °C [2]. Thus, the most and least volatile compounds investigated here are the sources of greatest error in the model.

For 2-methylbutane ($I^T = 487$, boiling point = 27.8 °C), the evaporation rate constant predicted from Eq. 3.6 is 4.374 h⁻¹, while the experimentally determined rate constant was 8.999 h⁻¹, yielding the error of -106%. The quality of fit ($R^2=0.8605$) of the first-order decay curve for this compound was the poorest of the 12 compounds studied. Additionally, the retention index for 2-methylbutane was determined *via* extrapolation, as the alkane ladder was defined across the range $I^T = 500 - 800$. These factors likely contribute to the large error in prediction observed for this compound.

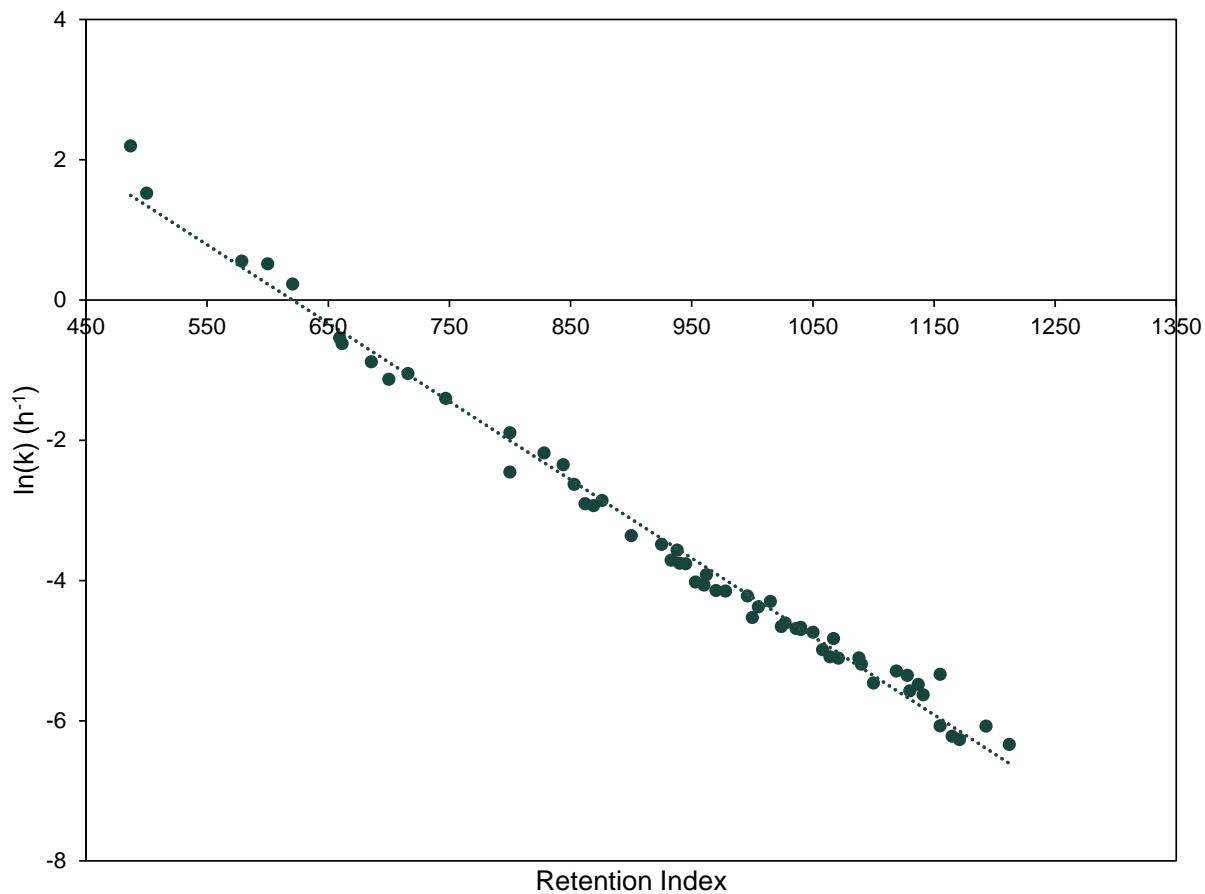


Figure 3.2. Natural logarithm of the evaporation rate constant (k) versus retention index (I^T) for previously collected data ($I^T = 800 - 1200$) [2] combined with rate constants for 12 additional volatile compounds ($I^T = 500 - 800$) at 10°C . Linear regression equation: $y = -0.0112 x + 6.93$ ($R^2 = 0.9889$).

n-Octane was the only compound studied that was also present in the set of compounds investigated by McIlroy *et al.* [2]. At 10 °C, McIlroy *et al.* reported an experimental evaporation rate constant of 0.151 h⁻¹, compared to 0.0861 h⁻¹ as experimentally determined in this work. Further, using the model defined in Eq. 3.6, the predicted evaporation rate constant for *n*-octane is 0.131 h⁻¹. When the predicted and experimental rate constant of *n*-octane are compared, a residual of +0.020 and an error of -15% is observed in the work of McIlroy *et al.* [2], while a residual of -0.065 and an error of +35% is observed in this work. Thus, in this work, the error in rate constant is more than double that determined by McIlroy *et al.* [2]. Moreover, the negative residual in this work indicates a slower rate of evaporation for *n*-octane compared to that determined by McIlroy *et al.*, which will be discussed further in Section 3.3.2.

To evaluate predictive accuracy, the refined kinetic model (Eq. 3.6) was used to predict chromatograms corresponding to each F_{Total} level of the validation mixture (Figure 3.3). For all three F_{Total} levels, Pearson product-moment correlation (PPMC) coefficients are greater than 0.99, indicating strong correlation between the predicted and experimental chromatograms (Table 3.2). Specific compounds were then compared by calculating the error between the peak abundance in the predicted and experimental chromatograms, which were then averaged to determine the MAPE for each F_{Total} level as well as for each compound across all F_{Total} levels (Table 3.2 and 3.3). Despite the observed strong correlation demonstrated by PPMC coefficients, the refined model typically predicts higher abundance for most compounds at all three F_{Total} levels, especially for compounds with $I^T < 700$. The MAPE in predicting peak abundance was 12.6%, 5.65%, and 6.13% for $F_{Total} = 0.54, 0.65,$ and $0.82,$ respectively (Table 3.2). At $F_{Total} = 0.54$ and $0.65,$ the highest error was associated with cyclohexane ($I^T = 650$), for which the error

was 47.6 and 15.3%, respectively (Table 3.3). At $F_{Total} = 0.82$, the greatest error was observed for 2-methylpentane ($I^T = 561$), for which the error was 17.9%.

The MAPE for all three fraction remaining levels was less than 13% and the PPMC coefficients were greater than 0.99, indicating a strong correlation between the predicted and experimental chromatograms (Table 3.2). This indicates that the refined model can accurately predict chromatograms for compounds with $I^T < 800$.

Table 3.2. Error in Prediction of Chromatograms for Refined Model at 10 °C

F_{Total}	PPMC	MAPE (%)
0.54	0.9908	12.6
0.65	0.9968	5.65
0.82	0.9943	6.13

PPMC = Pearson product-moment correlation coefficient

MAPE = mean absolute percent error

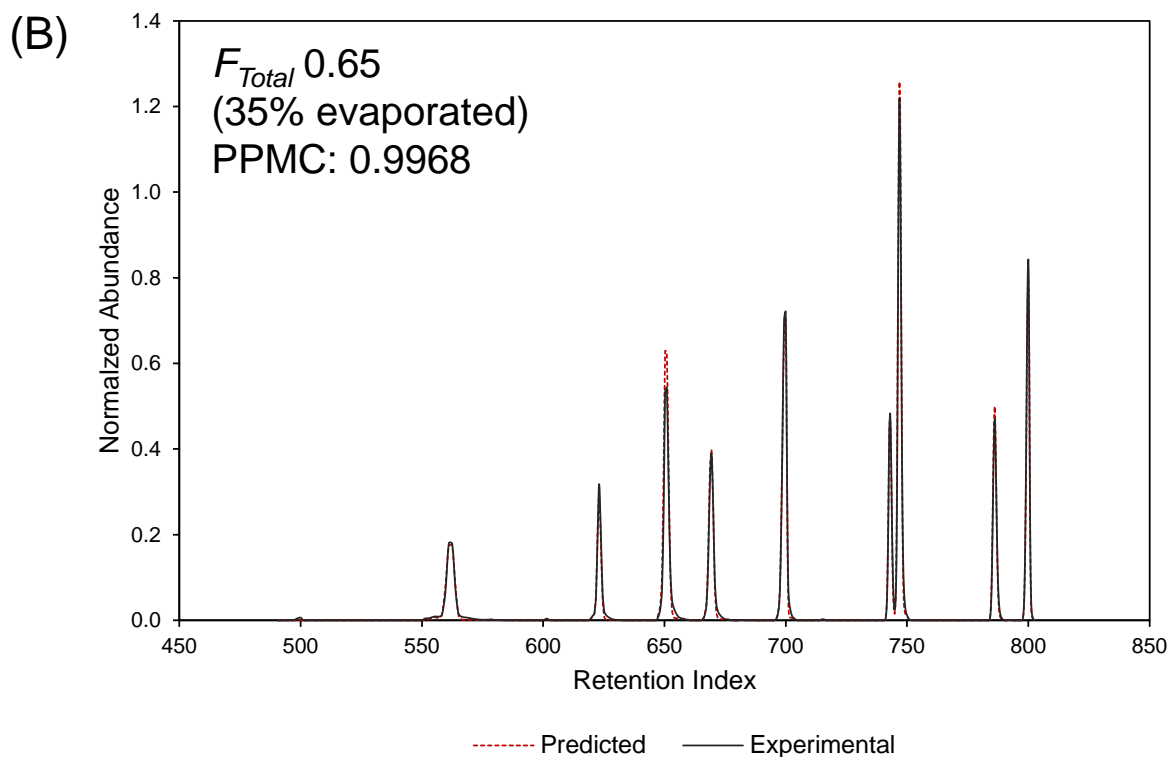
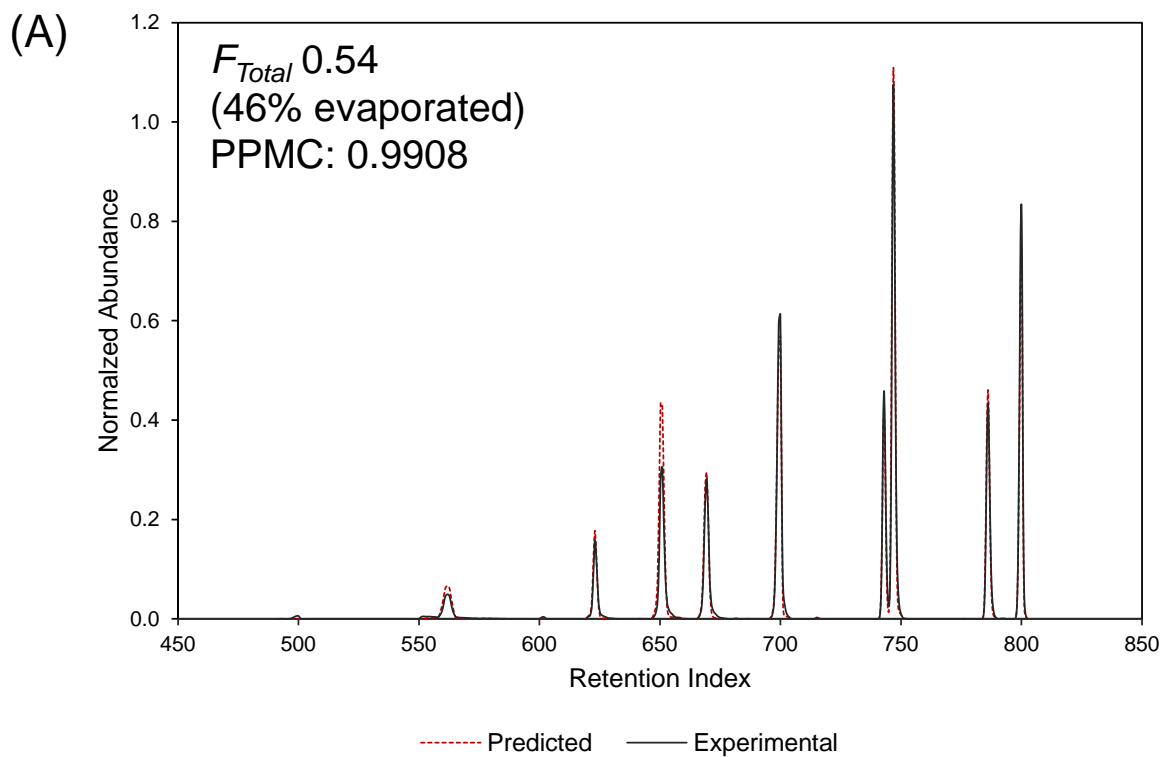


Figure 3.3. Experimental (black) *versus* predicted (red) chromatograms using the refined model (Eq. 3.6) for the validation mixture evaporated to (A) $F_{Total} = 0.54$, (B) $F_{Total} = 0.65$, and (C) $F_{Total} = 0.82$ at 10 °C

Figure 3.3. (cont'd)

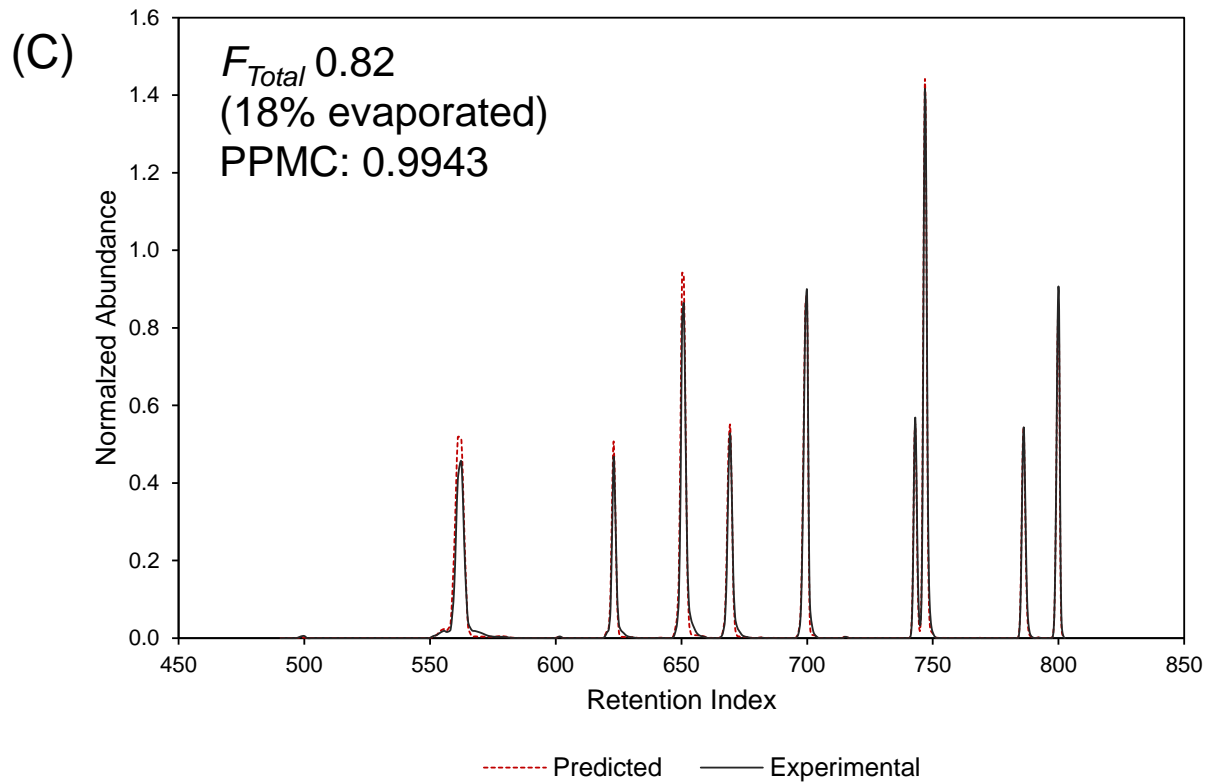


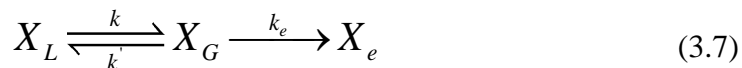
Table 3.3. Predictive Accuracy of the Refined Model at 10 °C for Individual Compounds in the Validation Mixture

Compound	Percent Error (%)*			MAPE
	$F_{Total} = 0.82$	$F_{Total} = 0.65$	$F_{Total} = 0.54$	
2-Methylpentane	17.9	-4.68	17.6	13.4
2,4,-Dimethylpentane	5.81	-10.1	8.07	7.99
Cyclohexane	10.1	15.3	47.6	24.3
3-Methylhexane	2.61	-0.79	2.01	1.80
<i>n</i> -Heptane	-3.79	-5.75	-9.84	6.46
2,3,4-Trimethylpentane	-3.71	-2.47	-8.41	4.86
Toluene	-0.96	3.47	5.15	3.19
Cycloheptane	-2.59	3.21	2.25	2.68
<i>n</i> -Octane	-7.69	-5.14	-12.1	8.31

* Negative error indicates underprediction of abundance, while positive error indicates overprediction

3.3.2 Correcting Rate Constants for Condensation

Due to the poor fit of the first-order kinetic decay for the more volatile compounds, additional steps were taken to improve the quality of the data. The decay curves shown in Figure 3.1 for *n*-pentane and *n*-octane exhibit a systematic departure of the data from the first-order rate equation (Eq. 2.2). As discussed previously, all data points greater than 0.5 h are above the curve for *n*-pentane (Figure 3.1A) and many data points at 3 h and 5 h are above the curve for *n*-octane (Figure 3.1D). This suggests that the simple first-order kinetic model – an irreversible phase change from liquid to vapor – is a reasonable approximation but is not quite correct. If vapor is not efficiently removed, it will accumulate in the headspace of the evaporation chamber, as shown in the theoretical calculations (Figures 2.2A and B). When this occurs, the compound in the vapor phase (X_G) can recondense back into the liquid phase (X_L), establishing an equilibrium between the two phases, as shown in Eq. 3.7



where k and k' are the rate constants for evaporation and condensation, respectively. In addition to the liquid – vapor equilibrium, the compound in the vapor phase can exit (X_e) from the chamber by means of air flow, with a rate constant of k_e .

To quantify the volume of vapor condensing, experimental evaporations were repeated as described in Section 3.2.2; however, half of the petri dishes contained the binary mixture to be evaporated, while the other half contained only the C₁₄ solvent (*i.e.*, “blank” dishes). The evaporations were conducted in duplicate, alternating the time points for collection of petri dishes containing the mixture and the solvent, such that a full set of time points were collected for each. The evaporated mixtures and solvent blanks were prepared and analyzed by GC-MS, as described previously. The normalized abundance of the evaporated mixtures was plotted as a

function of evaporation time to generate the decay curve and determine k . The normalized abundance of the solvent blanks was separately plotted as a function of evaporation time to assess the extent of condensation of the compound and to determine k' .

Exemplar plots for *n*-octane are shown in Figure 3.4. The decay curve (Figure 3.4 A) exhibits a good quality fit with $R^2 = 0.9250$. However, as noted above, the normalized abundances at 3 h and 5 h are positioned primarily above the line. The presence of *n*-octane in the solvent blanks (Figure 3.4 B) indicates that condensation has occurred. In this plot, the highest abundance of *n*-octane is observed between 3 h and 5 h, with a normalized abundance ranging from 0.12 to 0.21. As a result, the normalized abundance of *n*-octane in the decay curve (Figure 3.4 A) is higher than expected between these times due to condensation of *n*-octane back into the petri dish. To minimize this contribution, the normalized abundance in the solvent blanks at each time point (Figure 3.4 B) was subtracted from the normalized abundance in the evaporation mixtures (Figure 3.4A) at the corresponding time point to generate a corrected decay curve (Figure 3.4 C). The decay curve was then fit to the first-order rate equation to determine the corrected evaporation rate constant, which now accounts for vapor condensation. With this correction, the normalized abundances for *n*-octane at 3 h and 5 h now lie on the line for the first-order fit (Figure 3.4 C). While there may be an overcorrection at 1.5 h, the fit of the data to the decay curve is improved, with R^2 values increasing from 0.9250 (Figure 3.4 A) to 0.9652 (Figure 3.4 C).

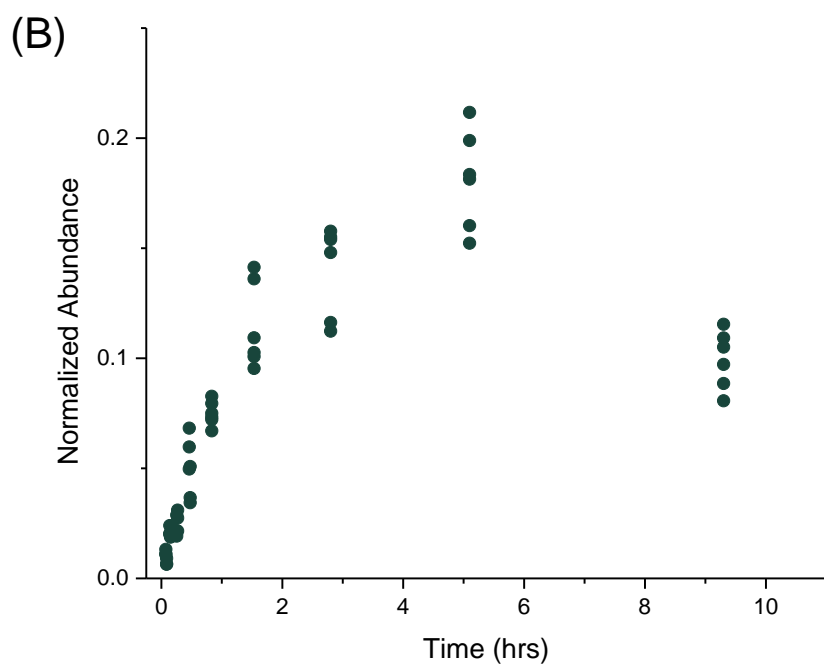
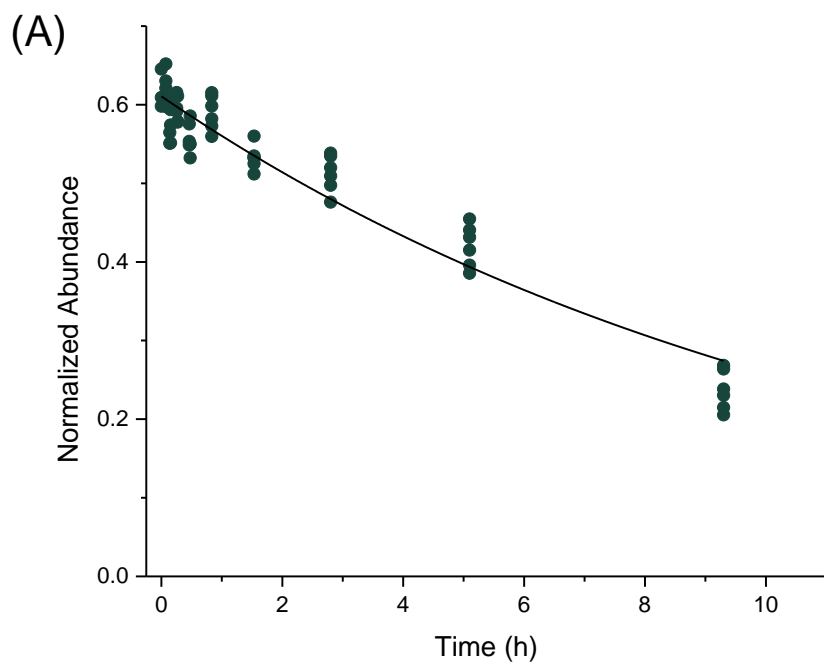
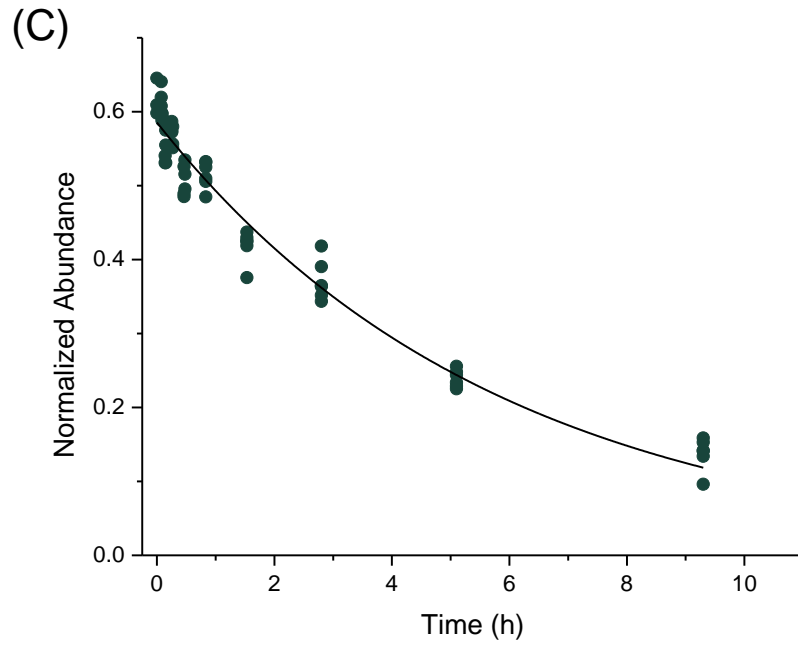


Figure 3.4. (A) Uncorrected decay curve, (B) Reverse curve, and (C) Corrected decay curve for *n*-octane ($I^T = 800$). Regression equations: Uncorrected: $C_t = 0.611 * \exp(-0.0861 * t)$, $R^2 = 0.9250$, Corrected: $C_t = 0.585 * \exp(-0.172 * t)$, $R^2 = 0.9652$.

Figure 3.4. (cont'd)



Corrected evaporation rate constants for all compounds are summarized in Table 3.4, alongside the previously reported uncorrected rate constants for comparison. The uncorrected rate constant for 2-methylbutane was 8.999 h⁻¹; however, after accounting for vapor condensation, the corrected rate constant for this compound was 17.96 h⁻¹, corresponding to a factor of two increase. Likewise, the rate constant for *n*-octane increased from 0.0861 h⁻¹ to 0.172 h⁻¹, also a factor of two increase, and is now more consistent with the rate constant previously reported by McIlroy *et al.* (0.151 h⁻¹) [2].

Table 3.4. Comparison of Uncorrected and Corrected Evaporation Rate Constants for Compounds at 10 °C

Compound	I^T	Uncorrected		Corrected	
		Evaporation Rate Constant (h ⁻¹)	R^2	Evaporation Rate Constant (h ⁻¹)	R^2
2-Methylbutane	487	8.999	0.8605	17.96	0.9565
<i>n</i> -Pentane	500	4.602	0.8793	5.713	0.8646
3-Methylpentane	578	1.744	0.9682	2.831	0.9712
<i>n</i> -Hexane	600	1.674	0.9485	3.010	0.9588
Methylcyclopentane	621	1.255	0.9317	2.552	0.9444
2-Methylhexane	659	0.584	0.9588	1.105	0.9555
2,3-Dimethylpentane	661	0.539	0.9498	1.062	0.9466
2,2,4-Trimethylpentane	686	0.414	0.9584	0.751	0.9504
<i>n</i> -Heptane	700	0.323	0.9477	0.625	0.9358
Methylcyclohexane	716	0.351	0.9584	0.658	0.9523
Toluene	747	0.246	0.9707	0.521	0.9626
<i>n</i> -Octane	800	0.0861	0.9250	0.172	0.9652

For all 12 compounds, the R^2 value for the fit of the data to the first-order rate equation changed negligibly or improved after correcting for condensation (Table 3.4). The most notable increases in quality of fit were observed for 2-methylbutane and *n*-octane, the two compounds that previously exhibited the greatest error in prediction. For compounds with $I^T < 600$, the quality of fit improved for time points occurring after 2 h in the corrected decay curves, as these

points deviated most significantly from the first-order kinetic model in the uncorrected decay curves. Even in cases where the R^2 value decreased slightly with correction, the later time points deviated less from the regression in the corrected curves, indicating a more accurate evaporation rate constant.

The corrected evaporation rate constants were combined with those determined previously by McIlroy *et al.* [2] and plotted as a function of retention index (Figure 3.5, corrected). Linear regression was then used to re-define the model, as shown in Eq. 3.8.

$$\ln(k) = -1.22 \times 10^{-2}I^T + 8.07 \quad (3.8)$$

The corrected model (Eq. 3.8) yielded both a steeper slope and a higher y-intercept than the uncorrected model (Eq. 3.6). The correlation coefficient for the linear regression decreased from $R^2 = 0.9889$ to 0.9844 when correcting for vapor condensation.

The corrected model (Eq. 3.8) was subsequently used to predict chromatograms of the validation mixture corresponding to the same F_{Total} levels as the experimental evaporations. When comparing the predicted and experimental chromatograms using the corrected model (Table 3.5), the PPMC coefficients exceeded 0.99 for all three F_{Total} levels. These values are indicative of strong correlation and were similar to or slightly greater than those using the uncorrected model.

Table 3.5. Comparison of Uncorrected and Corrected Models for Error in Prediction of Chromatograms at 10 °C

F_{Total}	Uncorrected		Corrected	
	PPMC	MAPE (%)	PPMC	MAPE (%)
0.54	0.9908	12.6	0.9919	11.2
0.65	0.9968	5.65	0.9968	7.62
0.82	0.9943	6.13	0.9948	4.88

PPMC = Pearson product-moment correlation coefficient

MAPE = mean absolute percent error

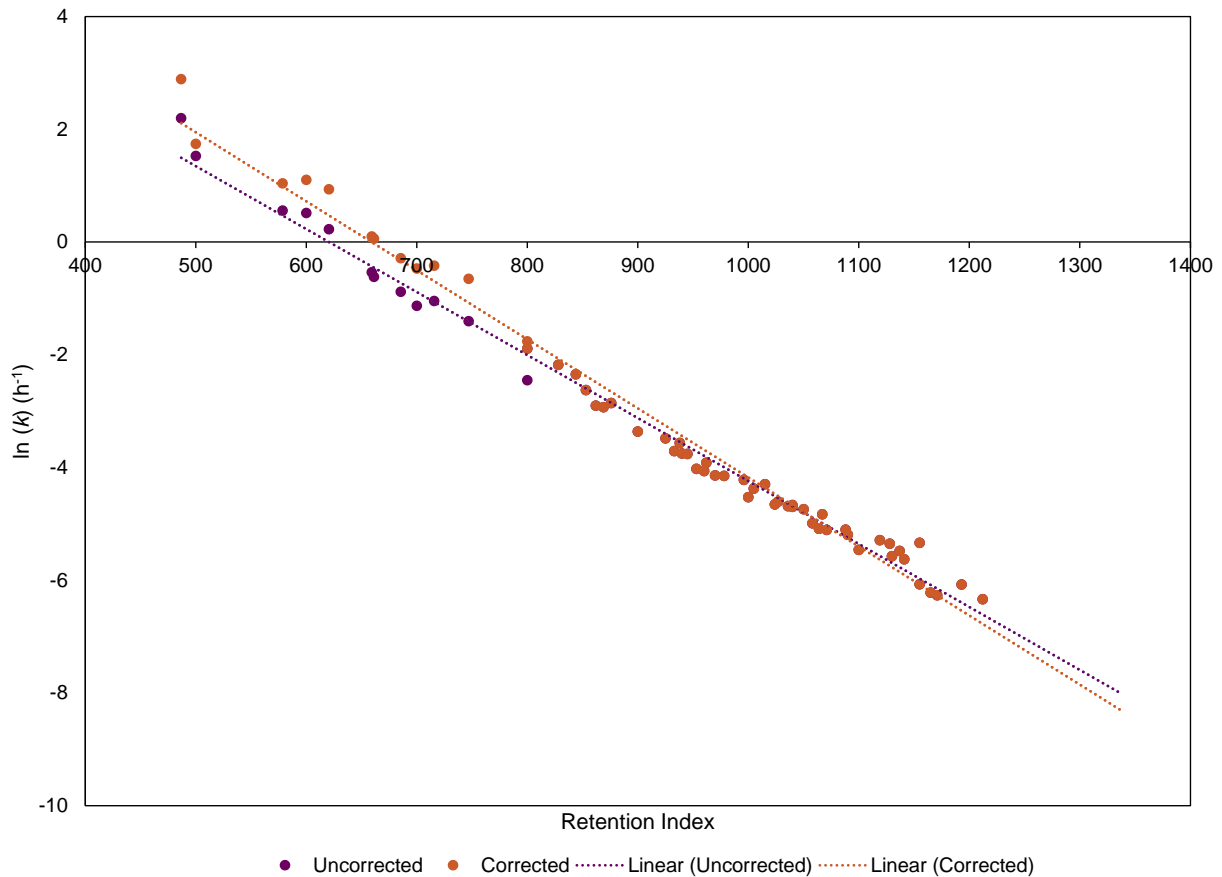


Figure 3.5. Natural logarithm of the evaporation rate constant (k) versus retention index (I^T) for previously collected data ($I^T = 800 - 1200$) [2] combined with rate constants for 12 additional volatile compounds ($I^T = 500 - 800$) at 10 °C. Linear regression equations: Uncorrected: $y = -0.0112 x + 6.93$ ($R^2 = 0.9889$), Corrected: $y = -0.0122 x + 8.07$ ($R^2 = 0.9844$).

The error in predicted abundance was calculated for individual compounds in the validation mixture (Table 3.6), as well as the MAPE for all compounds at each F_{Total} level (Table 3.5). At $F_{Total} = 0.54$, corresponding to the greatest extent of evaporation, the MAPE for the validation mixture was improved from 12.6% to 11.2% when vapor condensation was taken into account (Table 3.5). At $F_{Total} = 0.65$, the MAPE increased from 5.65% to 7.62% using the corrected model. Finally, at $F_{Total} = 0.82$, the MAPE improved from 6.13% to 4.88% using the corrected model. The predictive accuracy over all three F_{Total} levels was 7.89% for the corrected model, compared with 8.11% for the uncorrected model, with seven of nine compounds in the validation mixture showing improvement.

The uncorrected and corrected models consistently underpredicted the abundance of *n*-heptane and *n*-octane at all three F_{Total} levels. However, the MAPE for *n*-heptane over all three F_{Total} levels was improved from 6.46% to 5.40% when using the corrected model. Similarly, the MAPE for *n*-octane was improved from 8.31% to 6.90% (Table 3.3 and 3.6).

The uncorrected and corrected models exhibited the poorest predictive accuracy for cyclohexane. The errors for cyclohexane were 47.6% and 42.6% for the uncorrected and corrected models, respectively, at $F_{Total} = 0.54$ (Table 3.3 and 3.6). While the error was lower with the corrected model, it was still more than twice the error for all other compounds in the validation mixture. Of the 12 compounds used to develop the refined model, only two were cyclic compounds: methylcyclopentane ($I^T = 621$) and methylcyclohexane ($I^T = 716$). When linear regression was performed on the data from the corrected decay curves (Figure 3.5), both compounds were above the line of fit. Therefore, the model predicts that these compounds evaporate more slowly than observed experimentally. Ultimately, this leads to overprediction of the abundance for the cyclic compounds in the validation mixture (Table 3.6).

Table 3.6. Predictive Accuracy of the Corrected Model at 10 °C for Individual Compounds in the Validation Mixture

Compound	Percent Error (%)*			MAPE (%)
	$F_{Total} = 0.82$	$F_{Total} = 0.65$	$F_{Total} = 0.54$	
2-Methylpentane	10.8	-21.5	-18.4	16.9
2,4,-Dimethylpentane	5.09	-13.3	-1.09	6.49
Cyclohexane	10.4	14.4	42.6	22.5
3-Methylhexane	3.27	-0.38	0.80	1.48
<i>n</i> -Heptane	-2.90	-4.36	-8.94	5.40
2,3,4-Trimethylpentane	-2.77	-0.60	-6.39	3.25
Toluene	0	5.45	7.51	4.32
Cycloheptane	-1.77	5.04	4.59	3.80
<i>n</i> -Octane	-6.96	-3.55	-10.2	6.90

* Negative error indicates underprediction of abundance, while positive error indicates overprediction

Overall, these data demonstrate improvements in predictive accuracy when the experimental rate constants are corrected for condensation. The original model developed by McIlroy *et al.* [1,2] used less volatile compounds ($I^T = 800 - 1400$) and, as such, no condensation correction was necessary. However, with substantially more volatile compounds ($I^T = 487 - 800$), condensation becomes more important, and correction is necessary to accurately measure the rate constants.

3.3.3 Refinement and Validation of the Fixed-Temperature Models at 20 and 30 °C

The binary mixtures were evaporated at temperatures of 20 °C and 30 °C, and kinetic models corrected for condensation were developed following the procedures described in Sections 3.2.2 and 3.3.2. The corrected evaporation rate constants for the fixed-temperature models at 20 and 30 °C are shown in Table 3.7 and plotted as a function of I^T , alongside the fixed-temperature model at 10 °C (Figure 3.6).

Table 3.7. Corrected Evaporation Rate Constants for the Fixed Temperature Models at 20 and 30 °C

Compound	I^T	Evaporation Rate Constant (h^{-1})	
		20 °C	30 °C
2-Methylbutane	487	23.46	32.14
<i>n</i> -Pentane	500	18.56	33.09
3-Methylpentane	578	4.287	5.805
<i>n</i> -Hexane	600	3.863	4.731
Methylcyclopentane	621	2.975	4.037
2-Methylhexane	659	0.749	2.145
2,3-Dimethylpentane	661	1.413	2.095
2,2,4-Trimethylpentane	686	1.011	1.507
<i>n</i> -Heptane	700	0.823	1.476
Methylcyclohexane	716	0.749	1.275
Toluene	747	0.644	1.093
<i>n</i> -Octane	800	0.240	0.416

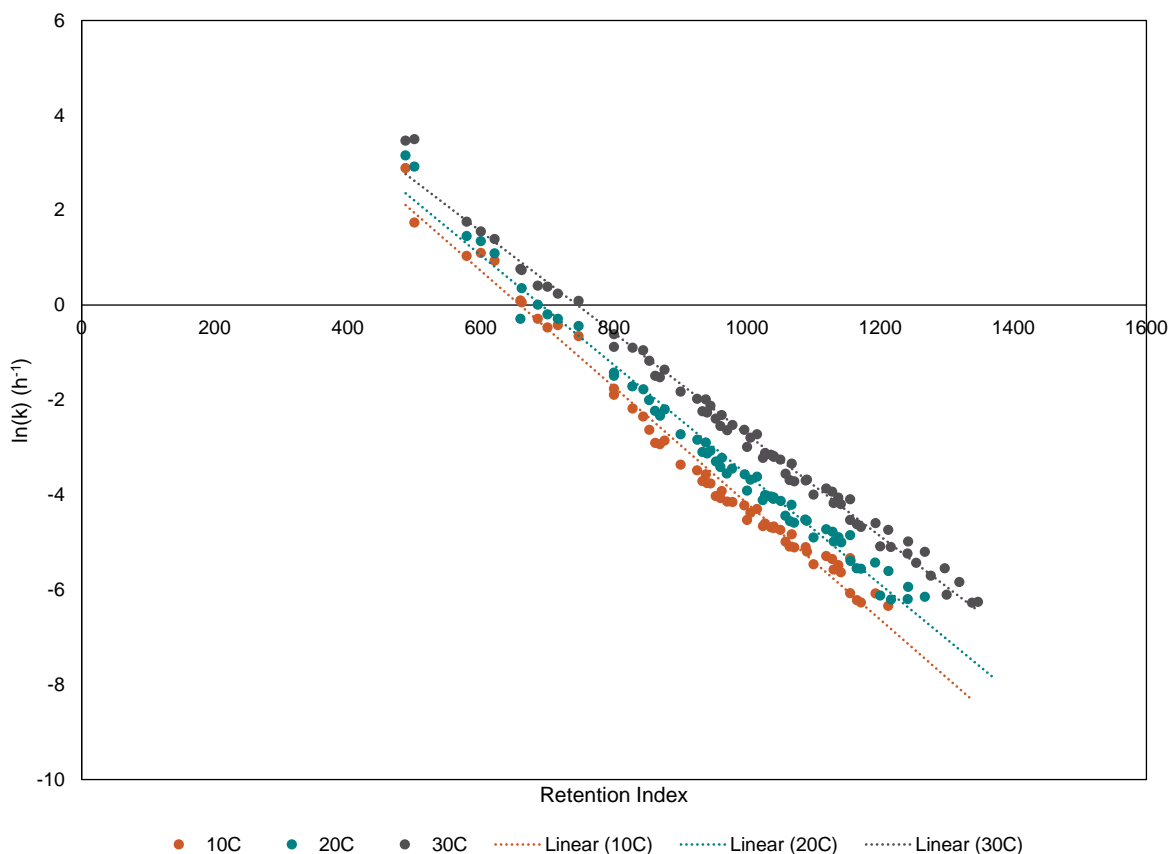


Figure 3.6. Natural logarithm of the corrected evaporation rate constant (k) versus retention index (I^T) for 12 volatile compounds ($I^T = 500 - 800$) with previously collected data ($I^T = 800 - 1200$) [1,2] at 10, 20, and 30 °C

The corrected models at 20 °C and 30 °C are shown in Eq. 3.9 and Eq. 3.10, respectively.

$$\ln(k) = -1.16 \times 10^{-2}I^T + 7.99 \quad (3.9)$$

$$\ln(k) = -1.07 \times 10^{-2}I^T + 7.97 \quad (3.10)$$

The fit of the data to the regression lines yielded R^2 values of 0.9859 and 0.9911 for temperatures of 20 °C and 30 °C, respectively. With increasing temperature, the slope and intercepts decreased while the R^2 values were improved.

The validation mixture was experimentally evaporated at 20 °C to levels of $F_{Total} = 0.36$, 0.42, 0.53, 0.66, and 0.81. For all five F_{Total} levels, the corrected model at 20 °C (Eq. 3.9) predicted the chromatograms with high accuracy, as demonstrated by PPMC coefficients greater than 0.97 (Table 3.8). As the F_{Total} level increased, both the PPMC coefficients and the error for predicting the abundance of individual compounds were improved. At the highest level of $F_{Total} = 0.81$, the MAPE for all validation compounds was 2.97%, as compared to 26.9% at the lowest level of $F_{Total} = 0.36$. The corrected model overpredicted the abundance of the two cyclic compounds (cyclohexane and cycloheptane) as well as toluene. The MAPE in predicting abundance across the five F_{Total} levels was 11.9%, 9.68%, and 12.5%, respectively, for cyclohexane, cycloheptane, and toluene (Table 3.9). As the F_{Total} level decreased for these compounds, the error increased because the model overpredicted the abundance more substantially.

Table 3.8. Predictive Accuracy of the Corrected Models at 20 and 30 °C

20 °C			30 °C		
F_{Total}	PPMC	MAPE (%)	F_{Total}	PPMC	MAPE (%)
0.36	0.9799	26.9	0.25	0.9553	34.1
0.42	0.9884	22.8	0.36	0.9640	25.1
0.53	0.9869	14.6	0.55	0.9835	12.3
0.66	0.9954	8.31	0.69	0.9970	5.81
0.81	0.9963	2.97	0.83	0.9952	4.89

PPMC = Pearson product-moment correlation coefficient

MAPE = mean absolute percent error

The validation mixture was experimentally evaporated at 30 °C to levels of $F_{Total} = 0.25$, 0.36, 0.55, 0.69, and 0.83. The corrected kinetic model at 30 °C (Eq. 3.10) predicted the chromatograms corresponding to all five evaporation levels with PPMC coefficients greater than 0.95. As the F_{Total} level increased, the PPMC coefficients and the errors in predicted abundance were improved. The MAPE values range from 4.89% at the highest F_{Total} level to 34.1% at the lowest F_{Total} level (Table 3.8). As observed previously, the corrected model at 30 °C overpredicted the abundance of cyclohexane, cycloheptane, and toluene in three of the evaporations ($F_{Total} = 0.69$, 0.55, and 0.36). At the lowest level of $F_{Total} = 0.25$, the abundances of cycloheptane and toluene were overpredicted while at the highest level of $F_{Total} = 0.83$, only the abundance of cycloheptane was overpredicted (Table 3.10).

While the errors in predicted abundance for individual compounds at 20 and 30 °C were higher than those determined at 10 °C, the validation mixture was evaporated to lower F_{Total} levels at the higher temperatures. The greater extent of evaporation caused lower GC peak abundances and, therefore, contributed to the higher error observed in prediction. When comparing similar F_{Total} levels at each temperature, the resulting MAPE and PPMC coefficients were similar. For example, the MAPE and PPMC coefficient for $F_{Total} = 0.54$ at 10 °C were 11.2% and 0.9919, respectively (Table 3.5), while those for $F_{Total} = 0.53$ at 20 °C were 14.6%

and 0.9869, respectively (Table 3.8). Similarly, for $F_{Total} = 0.55$ at 30 °C, the resulting MAPE and PPMC coefficient were 12.3% and 0.9835, respectively (Table 3.8).

Despite the lower predictive accuracy at higher temperatures, the PPMC coefficients still indicate a strong correlation between predicted and experimental chromatograms at both 20 °C and 30 °C (Table 3.8). All comparisons resulted in PPMC coefficients greater than 0.95, with coefficients greater than 0.98 for levels of $F_{Total} > 0.50$. This indicates that the model performs well for volatile compounds, which addresses a limitation highlighted in earlier work.

Table 3.9. Predictive Accuracy of the Corrected Model at 20 °C for Individual Compounds in the Validation Mixture

Compound	Percent Error (%)*					MAPE (%)
	$F_{Total} = 0.81$	$F_{Total} = 0.66$	$F_{Total} = 0.53$	$F_{Total} = 0.42$	$F_{Total} = 0.36$	
2-Methylpentane	-4.63	-26.0	-46.7	-82.3	-90.6	50.0
2,4,-Dimethylpentane	-3.30	-13.0	-22.7	-35.9	-47.9	24.6
Cyclohexane	5.06	8.41	15.6	17.5	12.7	11.9
3-Methylhexane	-1.09	-5.19	-9.68	-14.7	-22.3	10.6
<i>n</i> -Heptane	-4.21	-6.53	-10.0	-13.5	-17.7	10.4
2,3,4-Trimethylpentane	1.31	-0.23	-2.84	-4.68	-6.28	3.07
Toluene	3.33	7.58	11.0	18.1	22.4	12.5
Cycloheptane	3.21	6.85	9.50	12.8	16.0	9.67
<i>n</i> -Octane	-0.60	-0.92	-3.18	-5.64	-6.25	3.32

* Negative error indicates underprediction of abundance, while positive error indicates overprediction

Table 3.10. Predictive Accuracy of the Corrected Model at 30 °C for Individual Compounds in the Validation Mixture

Compound	Percent Error (%)*					MAPE (%)
	$F_{Total} = 0.83$	$F_{Total} = 0.69$	$F_{Total} = 0.55$	$F_{Total} = 0.36$	$F_{Total} = 0.25$	
2-Methylpentane	-11.4	-17.5	-28.0	-75.8	-96.0	45.7
2,4,-Dimethylpentane	-5.68	-6.45	-17.9	-40.6	-62.4	26.6
Cyclohexane	-2.98	4.11	6.53	11.2	-4.31	5.83
3-Methylhexane	-5.88	-2.71	-13.7	-21.2	-34.1	15.5
<i>n</i> -Heptane	-8.74	-7.53	-18.4	-21.7	-27.7	16.8
2,3,4-Trimethylpentane	-1.85	-1.97	-11.1	-14.4	-17.1	9.28
Toluene	-2.89	3.42	3.07	20.4	32.0	12.4
Cycloheptane	0.77	6.22	3.46	12.7	22.2	9.07
<i>n</i> -Octane	-3.88	-2.41	-8.50	-8.03	-11.2	6.80

* Negative error indicates underprediction of abundance, while positive error indicates overprediction

3.3.4 Comparison to the Original Fixed-Temperature Kinetic Models

The original kinetic model of McIlroy *et al.* [1, 2] was developed by measuring evaporation rate constants for compounds with $I^T \geq 800$. However, the model has been applied to predict evaporation of gasoline, which required predicting rate constants for compounds with $I^T \leq 800$ [4,5]. The performance of the extended model developed in Sections 3.3.2 and 3.3.3 was compared to that of the original model, focusing specifically on accuracy in predicting chromatograms of the volatile compounds in the validation mixture at each evaporation level.

The original model was used to predict the chromatograms of the validation mixture evaporated to the three F_{Total} levels (0.54, 0.65, and 0.82) at 10 °C and compared to the predictions described in Sections 3.3.2 and 3.3.3. For all three F_{Total} levels, the PPMC coefficient was improved when using the refined corrected model, as compared to the original model (Table 3.11). The predictive accuracy was then assessed for each individual compound in the validation mixture by calculating the percent error in peak abundance at each F_{Total} level (Tables 3.12-3.14).

Table 3.11. Comparison of the Original Model to the Refined Corrected Model at 10 °C

F_{Total}	PPMC Coefficient	
	Original Model	Refined Corrected Model
0.54	0.9892	0.9919
0.65	0.9962	0.9968
0.82	0.9936	0.9948

Table 3.12. Comparison of the Predicted Accuracy of the Original Model *versus* the Refined Corrected Model at 10 °C with $F_{Total} = 0.54$

Compound	Percent Error (%)*	
	Original Model	Refined Corrected Model
2-Methylpentane	57.2	-18.4
2,4-Dimethylpentane	18.2	-1.07
Cyclohexane	54.7	42.6
3-Methylhexane	4.83	0.80
<i>n</i> -Heptane	-9.23	-8.94
2,3,4-Trimethylpentane	-9.07	-6.39
Toluene	4.32	7.51
Cycloheptane	1.06	4.59
<i>n</i> -Octane	-13.2	-10.2
MAPE	19.1	11.2

* Negative error indicates underprediction of abundance, while positive error indicates overprediction

Table 3.13. Comparison of the Predicted Accuracy of the Original Model *versus* the Refined Corrected Model at 10 °C with $F_{Total} = 0.65$

Compound	Percent Error (%)*	
	Original Model	Refined Corrected Model
2-Methylpentane	14.3	-21.5
2,4-Dimethylpentane	-5.03	-13.3
Cyclohexane	18.5	14.4
3-Methylhexane	0.723	-0.375
<i>n</i> -Heptane	-5.49	-4.36
2,3,4-Trimethylpentane	-3.03	-0.604
Toluene	2.84	5.45
Cycloheptane	2.37	5.04
<i>n</i> -Octane	-5.93	-3.55
MAPE	6.47	7.62

* Negative error indicates underprediction of abundance, while positive error indicates overprediction

Table 3.14. Comparison of the Predicted Accuracy of the Original Model *versus* the Refined Corrected Model at 10 °C with $F_{Total} = 0.82$

Compound	Percent Error (%)*	
	Original Model	Refined Corrected Model
2-Methylpentane	25.3	10.8
2,4-Dimethylpentane	7.40	5.09
Cyclohexane	10.7	10.4
3-Methylhexane	2.79	3.27
<i>n</i> -Heptane	-4.01	-2.90
2,3,4-Trimethylpentane	-4.14	-2.77
Toluene	-1.41	0
Cycloheptane	-3.05	-1.77
<i>n</i> -Octane	-8.11	-6.96
MAPE	7.43	4.88

* Negative error indicates underprediction of abundance, while positive error indicates overprediction

The MAPE was improved when using the refined corrected model over the original model at the lowest and highest F_{Total} levels, 0.54 and 0.82, respectively (Table 3.12 and 3.14). At the lowest F_{Total} level (0.54), the error was improved for all individual compounds except toluene and cycloheptane. The original model predicted the abundance of toluene with an error of 4.32%, while the refined corrected model exhibited a higher error of 7.51%. Similarly, for cycloheptane, the error increased from 1.06% to 4.59% using the refined corrected model. In both models, the abundance was overpredicted, as demonstrated by the positive error. The original model also overpredicted the abundance of the three most volatile compounds. The error for the three most volatile compounds in the validation mixture, 2-methylpentane ($I^T = 563$), 2,4-dimethylpentane ($I^T = 623$), and cyclohexane ($I^T = 650$), when predicting using the original model were 57.2%, 18.2%, and 54.7%, respectively. The error in prediction was improved for all three compounds when using the refined corrected model with errors of -18.4%, -1.09%, and 42.6%, respectively. The abundance of the two most volatile compounds, 2-methylpentane and 2,4-dimethylpentane, was now underpredicted using the refined corrected model, but the overall

error was reduced by 68% and 94%, respectively. Both models overpredicted the abundance of cyclohexane, but the error was reduced by 22% when using the refined corrected model.

The error in prediction was also improved for the highest F_{Total} level in the validation study at 10 °C when using the refined corrected model as opposed to the original model, with an improvement in MAPE from 7.43% to 4.88% (Table 3.14). At this F_{Total} level, the error in prediction was improved for all compounds except 3-methylhexane when using the refined corrected model compared to the original model. However, the error only increased from 2.79% to 3.27%, indicating a marginal decrease in model performance. Similar to the trend observed for the lowest F_{Total} level, the error for each of the three most volatile compounds was improved slightly. The error in prediction was improved from 25.3% to 10.8% for 2-methylpentane (57% decrease), 7.40% to 5.09% for 2,4-dimethylpentane (31% decrease), and 10.7% to 10.4% for cyclohexane (2.8% decrease). At $F_{Total} = 0.82$, both models overpredicted the abundance of these compounds.

At the intermediate F_{Total} level (0.65), the PPMC coefficient between the predicted and experimental chromatogram improved from 0.9962 to 0.9968 using the original model and the refined model, respectively (Table 3.11). However, the MAPE in predicting compound abundance was slightly higher when using the refined corrected model (7.62%) compared to the original model (6.47%) (Table 3.13). At $F_{Total} = 0.65$, the refined model predicted more than half of the validation compounds with better accuracy, including cyclohexane, 3-methylhexane, *n*-heptane, 2,3,4-trimethylpentane, and *n*-octane. However, the abundance of the two most volatile compounds, 2-methylpentane ($I^T = 563$) and 2,4-dimethylpentane ($I^T = 623$), was underpredicted with a substantially higher error than observed using the original model (Table 3.13). When the two most volatile compounds were omitted from the error calculation, the MAPE for the

remaining seven compounds was 5.55% and 4.83% for the original and refined corrected models, respectively. This marked improvement, combined with the improvement in the PPMC coefficient, indicates that the refined corrected model does predict the chromatogram of the validation mixture at $F_{Total} = 0.65$ with better accuracy overall.

The original fixed-temperature model was used to predict chromatograms of the validation mixture evaporated to the five F_{Total} levels (0.36, 0.42, 0.53, 0.66, and 0.81) at 20 °C. For all five F_{Total} levels, the original model and the refined corrected model predicted the chromatograms with high accuracy (Table 3.15). At $F_{Total} = 0.81$, the PPMC coefficient was improved when predicting using the refined model. For all other F_{Total} levels, the PPMC coefficient was either equivalent between the original model and the refined model or marginally lower for the refined model. Regardless, even for the most evaporated mixture ($F_{Total} = 0.36$), the PPMC coefficient was greater than 0.9799, indicating a strong correlation between the predicted and experimental chromatograms.

Table 3.15. Comparison of the Original Model to the Refined Corrected Model at 20 °C

F_{Total}	PPMC Coefficient	
	Original Model	Refined Corrected Model
0.36	0.9801	0.9799
0.42	0.9884	0.9884
0.53	0.9871	0.9968
0.66	0.9958	0.9954
0.81	0.9960	0.9963

The predictive accuracy for the individual compounds was then determined by calculating the error in abundance using both the original model and the refined corrected model at 20 °C (Table A3.1 – A3.5). Because the validation mixture was evaporated to lower F_{Total} levels at 20 °C than at 10 °C, the most volatile compounds in the mixture were almost completely evaporated at the lower F_{Total} levels. For this reason, the error associated with these

compounds when predicting abundance was high (*i.e.*, 2-methylpentane at $F_{Total} = 0.36$ and 0.42 , Table A3.1 and A3.2). To assess overall error more accurately, the error for any compound with a normalized abundance less than 5% of the normalized abundance in the chromatogram of the unevaporated mixture was omitted from the MAPE calculation for that F_{Total} level (denoted by asterisk in Appendix tables).

At four of the five F_{Total} levels for the validation mixture at 20 °C, the refined corrected model improved on the prediction of abundance for *n*-octane and 2,3,4-trimethylpentane. At all F_{Total} levels, the refined model predicted the abundance of cyclohexane more accurately. The improvement is especially notable for cyclohexane at the lower F_{Total} levels. The error in prediction was improved from 29.7% to 8.40% at $F_{Total} = 0.36$ and from 22.2% to 7.79% at $F_{Total} = 0.42$ using the refined corrected model compared to the original model. While the MAPE is only improved for one F_{Total} level (0.81) at 20 °C using the refined fixed-temperature model compared to the original model, the MAPE is below 18% for all comparisons and the average difference in MAPE between the two models is only 2.2%.

The final comparisons made for the fixed-temperature models was that between the original model and the refined models at 30 °C. Due to the similarity in regression coefficients for the original and refined fixed-temperature models, the predictive accuracy was also similar when predicting the chromatograms of the validation mixture to the five F_{Total} levels studied at 30 °C (Table 3.16).

Table 3.16. Comparison of the Original Model to the Refined Corrected Model at 30 °C

F_{Total}	PPMC Coefficient	
	Original Model	Refined Corrected Model
0.25	0.9550	0.9553
0.36	0.9640	0.9640
0.55	0.9836	0.9835
0.69	0.9971	0.9970
0.83	0.9952	0.9952

When comparing the predictive accuracy of the abundance of individual compounds, the average difference in MAPE between the original and refined corrected models at 30 °C was only 1.1% (Tables A3.6 – A3.10). The trend in prediction accuracy was similar to the fixed-temperature models at 20 °C, with *n*-octane, 2,3,4-trimethylpentane, and cyclohexane exhibiting a consistent improvement in prediction when using the refined corrected model compared to the original model. At the lowest F_{Total} level (0.25), the error for *n*-octane was improved from -12.9% to -11.2% using the refined corrected model and, at the highest F_{Total} level (0.83), the error was improved from -4.24% to -3.88% (Tables A3.6 and A3.10). Cyclohexane exhibited a more substantial improvement in prediction using the refined corrected model. At $F_{Total} = 0.25$, the error was improved from 8.46% to -4.31% (Table A3.6), a 49% improvement.

Overall, the performance of the refined fixed-temperature models was either comparable to or improved compared to the original models at corresponding temperatures, validating the use of the model to predict evaporation of compounds with $I^T < 800$. The extension of the linear range of the fixed-temperature models to encompass compounds found in gasoline enhances the forensic applicability of the kinetic model.

3.3.5 Refinement and Validation of the Variable-Temperature Model

In addition to the fixed-temperature models previously developed, McIlroy *et al.* also developed a variable-temperature model by performing multiple regression on data spanning a temperature range 5 – 35 °C (Eq. 1.6) [2]. Because only three temperatures (10, 20, and 30 °C) were studied in this work, the original variable-temperature model was redefined, omitting the additional two temperatures (5 and 35 °C). This enables a more direct comparison between the original and the refined corrected variable-temperature models. The variable-temperature model based on the original and the refined corrected rate constants at the three temperatures (10, 20, and 30 °C) are given in Eq. 3.11 and 3.12, respectively.

$$\ln(k) = -1.03 \times 10^{-2}I^T - 6444 \left(\frac{1}{T}\right) + 28.7 \quad (3.11)$$

$$\ln(k) = -1.14 \times 10^{-2}I^T - 6021 \left(\frac{1}{T}\right) + 28.5 \quad (3.12)$$

When comparing the original variable-temperature model (Eq. 1.6) to the newly defined model with only three temperatures, the slope with regards to I^T was unchanged and was similar to the slope in the previous fixed-temperature models. This indicates that rate constant exhibits a similar dependence on I^T when using the variable-temperature model. The slope with regards to temperature became marginally more negative in Eq. 3.11 compared to Eq. 1.6, from -6410 to -6444 (1% difference). When extending to the lower I^T range (Eq. 3.12), the quality of fit for the linear regression was improved from $R^2 = 0.9819$ for the original variable-temperature model to $R^2 = 0.9834$ for the refined corrected variable-temperature model.

To test the predictive accuracy of the original variable-temperature model (Eq. 3.11) compared to the refined corrected variable-temperature model (Eq. 3.12), the chromatograms of the validation mixture at each temperature and each F_{Total} level were predicted. Tables 3.17 – 3.19 summarize the PPMC coefficients for the comparisons.

Table 3.17. Comparison of the Original Variable-Temperature Model to the Refined Corrected Model at 10 °C

F_{Total}	PPMC Coefficient	
	Original Variable-Temperature Model	Refined Corrected Variable-Temperature Model
0.54	0.9887	0.9908
0.65	0.9961	0.9967
0.82	0.9933	0.9943

Table 3.18. Comparison of the Original Variable-Temperature Model to the Refined Corrected Model at 20 °C

F_{Total}	PPMC Coefficient	
	Original Variable-Temperature Model	Refined Corrected Variable-Temperature Model
0.36	0.9800	0.9800
0.42	0.9884	0.9885
0.53	0.9870	0.9869
0.66	0.9958	0.9955
0.81	0.9960	0.9962

Table 3.19. Comparison of the Original Variable-Temperature Model to the Refined Corrected Model at 30 °C

F_{Total}	PPMC Coefficient	
	Original Variable-Temperature Model	Refined Corrected Variable-Temperature Model
0.25	0.9551	0.9554
0.36	0.9640	0.9638
0.55	0.9836	0.9833
0.69	0.9971	0.9967
0.83	0.9952	0.9950

The validation mixture experimentally evaporated at 10 °C to three F_{Total} levels (0.54, 0.65, and 0.82) was predicted better when using the corrected refined model *versus* the original model (Table 3.17). The error in predicting the abundance of each individual compound was also determined (Tables A3.11 – A3.13). At all three F_{Total} levels, the corrected refined model consistently predicted compound abundance more accurately, with the exception of toluene and cycloheptane. The MAPE for the original model ranged from 6.72 – 23.4% for the three F_{Total}

levels, while the MAPE for the refined corrected model ranged from 5.34 – 13.9% (Tables A3.11 – A3.13). For both toluene and cycloheptane, the refined model overpredicted the abundance to a greater extent than the original model. However, the error in prediction was still below 8% for both compounds at all F_{Total} levels, indicating an accurate prediction of evaporation.

For 20 and 30 °C, the refined corrected models predicted the chromatograms of the validation mixture similarly to the original model, with either no change or a small increase or decrease in the PPMC coefficient (Tables 3.18 and 3.19). Similar to 10 °C model, the original variable-temperature model consistently predicts the abundance of toluene and cycloheptane more accurately at 20 and 30°C (Tables A3.14 – A3.23). Meanwhile, the refined corrected variable-temperature model consistently predicts the abundance of 2,3,4-trimethylpentane and *n*-octane more accurately at 20 and 30 °C. The most significant observation in the predictions at these two higher temperatures, however, is the poorer performance of the refined model when predicting the two most volatile compounds, 2-methylpentane and 2,4-dimethylpentane. The refined model is extended to include compounds with retention indices as low as 487, which should lead to a better prediction of compounds in this lower I^T range. Further investigation is necessary of the lower end of this I^T region to determine a reason for the discrepancy in performance of the refined models at higher temperatures. Regardless, the overall performance of the extended variable-temperature model demonstrates the ability to predict in an I^T range for which evaporation rate constants had not previously been measured

3.4 Conclusions

In this work, evaporation rate constants of volatile compounds with $I^T < 800$ were experimentally measured and incorporated in a kinetic model. The refined model was tested by predicting the evaporation of a validation mixture at 10 °C and levels of $F_{Total} = 0.54, 0.65,$ and

0.81. Strong correlation was demonstrated between the predicted and experimental chromatograms of the validation mixture, with PPMC coefficients greater than 0.99. The mean absolute percent error in predicting abundance of individual compounds was less than 13% for evaporations performed at 10 °C.

Although the model exhibited good predictive accuracy, further refinement was performed in which the evaporation rate constants were corrected to account for vapor condensation. With the condensation-corrected model, the accuracy in predicting chromatograms for the validation mixture remained high, with PPMC coefficients equal to or greater than those for the uncorrected model at 10 °C. Condensation-corrected models were also developed at 20 °C and 30 °C and the predictive accuracy demonstrated. For these models, strong correlation was again observed between predicted and experimental chromatograms of the validation mixture, with PPMC coefficients ranging from 0.99 to 0.95 for F_{Total} levels from 0.25 to 0.83.

The predictive accuracy of the refined fixed-temperature models at each of the three temperatures were then compared with the original kinetic model of McIlroy *et al* [1, 2]. At 10 °C, the refined model corrected for condensation consistently predicted the chromatograms of the validation mixture more accurately than the original model. At 20 and 30 °C, the refined models performed better at some F_{Total} levels while performing equally or marginally worse at other F_{Total} levels. Regardless, all comparisons of predicted and experimental chromatograms using either the original or refined fixed-temperature models exhibited a strong correlation, as demonstrated by PPMC coefficients greater than 0.95.

Following refinement of the fixed-temperature models to include more volatile compounds, the original variable-temperature model of McIlroy *et al.* [2] was extended to the lower T range and redefined. The chromatograms of the validation mixture experimentally

evaporated at 10, 20, and 30 °C for the fixed-temperature models were predicted using both the original and refined variable-temperature models to assess performance. For all cases, the predicted and experimental chromatograms demonstrated strong correlation with PPMC coefficients greater than 0.95 and MAPE ranging from 5.30 – 31.4% for the refined corrected model. Similar to the fixed-temperature models, the refined variable-temperature model performed better than the original model at 10 °C with variation in performance observed at 20 and 30 °C.

The measurement, correction, and validation of evaporation rate constants for volatile compounds eluting in the range $I^T = 500 - 800$ allows for the improvement of kinetic models that serve to predict evaporation of such compounds. Such predictions can be applied to forensic or environmental applications where the rate of evaporation is of interest.

APPENDIX

Table A3.1. Comparison of the Predicted Accuracy of the Original Model *versus* the Refined Corrected Model at 20 °C with $F_{Total} = 0.36$

Compound	Percent Error (%)*	
	Original Model	Refined Corrected Model
2-Methylpentane	-61.9**	-86.5**
2,4-Dimethylpentane	-26.8	-47.7
Cyclohexane	29.7	8.40
3-Methylhexane	-9.99	-19.4
<i>n</i> -Heptane	-12.0	-15.1
2,3,4-Trimethylpentane	-6.26	-4.81
Toluene	11.3	13.3
Cycloheptane	15.0	18.8
<i>n</i> -Octane	-12.8	-9.66
MAPE	15.5	17.1

* Negative error indicates underprediction of abundance, while positive error indicates overprediction

** Normalized abundance lower than 5% of abundance in unevaporated chromatogram, so error omitted from MAPE calculation

Table A3.2. Comparison of the Predicted Accuracy of the Original Model *versus* the Refined Corrected Model at 20 °C with $F_{Total} = 0.42$

Compound	Percent Error (%)*	
	Original Model	Refined Corrected Model
2-Methylpentane	-50.8**	-77.6**
2,4-Dimethylpentane	-16.4	-34.5
Cyclohexane	22.2	7.79
3-Methylhexane	-6.91	-13.5
<i>n</i> -Heptane	-13.8	-15.3
2,3,4-Trimethylpentane	-6.37	-4.54
Toluene	7.61	9.92
Cycloheptane	11.0	14.5
<i>n</i> -Octane	-11.2	-8.29
MAPE	11.9	13.5

* Negative error indicates underprediction of abundance, while positive error indicates overprediction

** Normalized abundance lower than 5% of abundance in unevaporated chromatogram, so error omitted from MAPE calculation

Table A3.3. Comparison of the Predicted Accuracy of the Original Model *versus* the Refined Corrected Model at 20 °C with $F_{Total} = 0.53$

Compound	Percent Error (%)*	
	Original Model	Refined Corrected Model
2-Methylpentane	-8.51	-43.6
2,4-Dimethylpentane	-13.9	-25.1
Cyclohexane	16.5	9.06
3-Methylhexane	-6.72	-9.87
<i>n</i> -Heptane	-10.6	-10.7
2,3,4-Trimethylpentane	-4.86	-2.94
Toluene	-0.692	1.41
Cycloheptane	6.82	9.56
<i>n</i> -Octane	-9.48	-7.16
MAPE	8.68	13.3

* Negative error indicates underprediction of abundance, while positive error indicates overprediction

Table A3.4. Comparison of the Predicted Accuracy of the Original Model *versus* the Refined Corrected Model at 20 °C with $F_{Total} = 0.66$

Compound	Percent Error (%)*	
	Original Model	Refined Corrected Model
2-Methylpentane	-9.27	-29.9
2,4-Dimethylpentane	-9.26	-15.2
Cyclohexane	3.38	0.577
3-Methylhexane	-5.12	-6.11
<i>n</i> -Heptane	-10.0	-9.45
2,3,4-Trimethylpentane	-3.08	-1.47
Toluene	-1.80	-0.126
Cycloheptane	4.88	6.79
<i>n</i> -Octane	-6.40	-4.74
MAPE	5.92	8.26

* Negative error indicates underprediction of abundance, while positive error indicates overprediction

Table A3.5. Comparison of the Predicted Accuracy of the Original Model *versus* the Refined Corrected Model at 20 °C with $F_{Total} = 0.81$

Compound	Percent Error (%)*	
	Original Model	Refined Corrected Model
2-Methylpentane	14.8	4.00
2,4-Dimethylpentane	9.81	7.53
Cyclohexane	14.3	13.7
3-Methylhexane	11.4	11.5
<i>n</i> -Heptane	5.52	6.29
2,3,4-Trimethylpentane	7.54	8.65
Toluene	4.74	5.83
Cycloheptane	9.80	10.90
<i>n</i> -Octane	2.00	2.97
MAPE	8.88	7.93

* Negative error indicates underprediction of abundance, while positive error indicates overprediction

Table A3.6. Comparison of the Predicted Accuracy of the Original Model *versus* the Refined Corrected Model at 30 °C with $F_{Total} = 0.25$

Compound	Percent Error (%)*	
	Original Model	Refined Corrected Model
2-Methylpentane	-92.4**	-95.9**
2,4-Dimethylpentane	-53.2	-62.4
Cyclohexane	8.46	-4.31
3-Methylhexane	-28.6	-34.1
<i>n</i> -Heptane	-25.3	-27.7
2,3,4-Trimethylpentane	-17.4	-17.1
Toluene	31.3	31.9
Cycloheptane	20.2	22.2
<i>n</i> -Octane	-12.9	-11.2
MAPE	24.7	26.4

* Negative error indicates underprediction of abundance, while positive error indicates overprediction

** Normalized abundance lower than 5% of abundance in unevaporated chromatogram, so error omitted from MAPE calculation

Table A3.7. Comparison of the Predicted Accuracy of the Original Model *versus* the Refined Corrected Model at 30 °C with $F_{Total} = 0.36$

Compound	Percent Error (%)*	
	Original Model	Refined Corrected Model
2-Methylpentane	-63.8**	-75.8**
2,4-Dimethylpentane	-32.1	-40.6
Cyclohexane	19.7	11.2
3-Methylhexane	-17.5	-21.2
<i>n</i> -Heptane	-20.4	-21.7
2,3,4-Trimethylpentane	-14.9	-14.4
Toluene	19.5	20.4
Cycloheptane	11.1	12.7
<i>n</i> -Octane	-9.40	-8.03
MAPE	18.1	18.8

* Negative error indicates underprediction of abundance, while positive error indicates overprediction

** Normalized abundance lower than 5% of abundance in unevaporated chromatogram, so error omitted from MAPE calculation

Table A3.8. Comparison of the Predicted Accuracy of the Original Model *versus* the Refined Corrected Model at 30 °C with $F_{Total} = 0.55$

Compound	Percent Error (%)*	
	Original Model	Refined Corrected Model
2-Methylpentane	-14.6	-28.0
2,4-Dimethylpentane	-13.8	-18.0
Cyclohexane	9.06	6.53
3-Methylhexane	-12.7	-13.7
<i>n</i> -Heptane	-18.5	-18.4
2,3,4-Trimethylpentane	-11.9	-11.1
Toluene	2.14	3.07
Cycloheptane	2.34	3.46
<i>n</i> -Octane	-9.49	-8.51
MAPE	10.5	12.3

* Negative error indicates underprediction of abundance, while positive error indicates overprediction

Table A3.9. Comparison of the Predicted Accuracy of the Original Model *versus* the Refined Corrected Model at 30 °C with $F_{Total} = 0.69$

Compound	Percent Error (%)*	
	Original Model	Refined Corrected Model
2-Methylpentane	-10.4	-17.5
2,4-Dimethylpentane	-4.49	-6.45
Cyclohexane	4.94	4.11
3-Methylhexane	-2.48	-2.71
<i>n</i> -Heptane	-7.85	-7.53
2,3,4-Trimethylpentane	-2.63	-1.97
Toluene	2.71	3.42
Cycloheptane	5.45	6.22
<i>n</i> -Octane	-3.10	-2.41
MAPE	4.90	5.81

* Negative error indicates underprediction of abundance, while positive error indicates overprediction

Table A3.10. Comparison of the Predicted Accuracy of the Original Model *versus* the Refined Corrected Model at 30 °C with $F_{Total} = 0.83$

Compound	Percent Error (%)*	
	Original Model	Refined Corrected Model
2-Methylpentane	-8.47	-11.4
2,4-Dimethylpentane	-5.07	-5.68
Cyclohexane	-2.86	-2.98
3-Methylhexane	-5.96	-5.88
<i>n</i> -Heptane	-9.02	-8.74
2,3,4-Trimethylpentane	-2.25	-1.85
Toluene	-3.28	-2.89
Cycloheptane	0.368	0.768
<i>n</i> -Octane	-4.24	-3.88
MAPE	4.61	4.89

* Negative error indicates underprediction of abundance, while positive error indicates overprediction

Table A3.11. Comparison of the Predicted Accuracy of the Original Variable-Temperature Model *versus* the Refined Corrected Model at 10 °C with $F_{Total} = 0.54$

Compound	Percent Error (%)*	
	Original Model	Refined Corrected Model
2-Methylpentane	92.9	30.5
2,4-Dimethylpentane	24.4	11.3
Cyclohexane	50.5	42.9
3-Methylhexane	7.83	5.23
<i>n</i> -Heptane	-6.82	-6.58
2,3,4-Trimethylpentane	-9.56	-7.80
Toluene	1.95	4.02
Cycloheptane	4.37	6.83
<i>n</i> -Octane	-12.0	-9.96
MAPE	23.4	13.9

* Negative error indicates underprediction of abundance, while positive error indicates overprediction

Table A3.12. Comparison of the Predicted Accuracy of the Original Variable-Temperature Model *versus* the Refined Corrected Model at 10 °C with $F_{Total} = 0.65$

Compound	Percent Error (%)*	
	Original Model	Refined Corrected Model
2-Methylpentane	20.7	-4.32
2,4-Dimethylpentane	-1.70	-7.32
Cyclohexane	19.7	16.8
3-Methylhexane	3.55	2.72
<i>n</i> -Heptane	-2.39	-1.68
2,3,4-Trimethylpentane	-1.91	-0.325
Toluene	2.25	3.93
Cycloheptane	5.30	7.13
<i>n</i> -Octane	-6.16	-4.57
MAPE	7.07	5.42

* Negative error indicates underprediction of abundance, while positive error indicates overprediction

Table A3.13. Comparison of the Predicted Accuracy of the Original Variable-Temperature Model *versus* the Refined Corrected Model at 10 °C with $F_{Total} = 0.82$

Compound	Percent Error (%)*	
	Original Model	Refined Corrected Model
2-Methylpentane	23.5	13.9
2,4-Dimethylpentane	10.3	8.58
Cyclohexane	10.2	9.79
3-Methylhexane	4.34	4.55
<i>n</i> -Heptane	-1.68	-1.01
2,3,4-Trimethylpentane	-3.63	-2.75
Toluene	1.23	2.15
Cycloheptane	-0.272	0.598
<i>n</i> -Octane	-5.44	-4.65
MAPE	6.72	5.34

* Negative error indicates underprediction of abundance, while positive error indicates overprediction

Table A3.14. Comparison of the Predicted Accuracy of the Original Variable-Temperature Model *versus* the Refined Corrected Model at 20 °C with $F_{Total} = 0.36$

Compound	Percent Error (%)*	
	Original Model	Refined Corrected Model
2-Methylpentane	-58.8**	-83.7**
2,4-Dimethylpentane	-24.9	-44.5
Cyclohexane	31.5	11.7
3-Methylhexane	-9.20	-17.9
<i>n</i> -Heptane	-11.5	-14.4
2,3,4-Trimethylpentane	-6.40	-5.07
Toluene	11.1	12.9
Cycloheptane	14.6	18.2
<i>n</i> -Octane	-13.0	-10.2
MAPE	15.3	16.9

* Negative error indicates underprediction of abundance, while positive error indicates overprediction

** Normalized abundance lower than 5% of abundance in unevaporated chromatogram, so error omitted from MAPE calculation

Table A3.15. Comparison of the Predicted Accuracy of the Original Variable-Temperature Model *versus* the Refined Corrected Model at 20 °C with $F_{Total} = 0.42$

Compound	Percent Error (%)*	
	Original Model	Refined Corrected Model
2-Methylpentane	-48.2**	-74.5**
2,4-Dimethylpentane	-15.1	-32.2
Cyclohexane	23.0	9.57
3-Methylhexane	-6.61	-12.8
<i>n</i> -Heptane	-13.8	-15.3
2,3,4-Trimethylpentane	-6.64	-5.02
Toluene	7.29	9.35
Cycloheptane	10.6	13.8
<i>n</i> -Octane	-11.5	-8.84
MAPE	11.8	13.3

* Negative error indicates underprediction of abundance, while positive error indicates overprediction

** Normalized abundance lower than 5% of abundance in unevaporated chromatogram, so error omitted from MAPE calculation

Table A3.16. Comparison of the Predicted Accuracy of the Original Variable-Temperature Model *versus* the Refined Corrected Model at 20 °C with $F_{Total} = 0.53$

Compound	Percent Error (%)*	
	Original Model	Refined Corrected Model
2-Methylpentane	-4.72	-38.5
2,4-Dimethylpentane	-12.7	-23.3
Cyclohexane	17.4	10.3
3-Methylhexane	-6.34	-9.33
<i>n</i> -Heptane	-10.5	-10.7
2,3,4-Trimethylpentane	-4.97	-3.25
Toluene	-0.815	1.07
Cycloheptane	6.63	9.12
<i>n</i> -Octane	-9.65	-7.53
MAPE	8.19	12.6

* Negative error indicates underprediction of abundance, while positive error indicates overprediction

Table A3.17. Comparison of the Predicted Accuracy of the Original Variable-Temperature Model *versus* the Refined Corrected Model at 20 °C with $F_{Total} = 0.66$

Compound	Percent Error (%)*	
	Original Model	Refined Corrected Model
2-Methylpentane	-7.82	-26.7
2,4-Dimethylpentane	-8.96	-14.2
Cyclohexane	3.45	1.03
3-Methylhexane	-5.16	-5.96
<i>n</i> -Heptane	-10.2	-9.56
2,3,4-Trimethylpentane	-3.28	-1.74
Toluene	-2.00	-0.404
Cycloheptane	4.67	6.48
<i>n</i> -Octane	-6.58	-5.00
MAPE	5.79	7.89

* Negative error indicates underprediction of abundance, while positive error indicates overprediction

Table A3.18. Comparison of the Predicted Accuracy of the Original Variable-Temperature Model *versus* the Refined Corrected Model at 20 °C with $F_{Total} = 0.81$

Compound	Percent Error (%)*	
	Original Model	Refined Corrected Model
2-Methylpentane	15.7	5.77
2,4-Dimethylpentane	9.98	7.89
Cyclohexane	14.3	13.8
3-Methylhexane	11.4	11.5
<i>n</i> -Heptane	5.44	6.15
2,3,4-Trimethylpentane	7.44	8.46
Toluene	4.64	5.65
Cycloheptane	9.70	10.7
<i>n</i> -Octane	1.90	2.81
MAPE	8.94	8.08

* Negative error indicates underprediction of abundance, while positive error indicates overprediction

Table A3.19. Comparison of the Predicted Accuracy of the Original Variable-Temperature Model *versus* the Refined Corrected Model at 30 °C with $F_{Total} = 0.25$

Compound	Percent Error (%)*	
	Original Model	Refined Corrected Model
2-Methylpentane	-93.4**	-98.6**
2,4-Dimethylpentane	-55.4	-73.3
Cyclohexane	5.40	-21.3
3-Methylhexane	-29.9	-42.0
<i>n</i> -Heptane	-26.0	-31.4
2,3,4-Trimethylpentane	-175	-17.1
Toluene	31.2	32.4
Cycloheptane	20.5	24.8
<i>n</i> -Octane	-12.6	-9.06
MAPE	24.8	31.4

* Negative error indicates underprediction of abundance, while positive error indicates overprediction

** Normalized abundance lower than 5% of abundance in unevaporated chromatogram, so error omitted from MAPE calculation

Table A3.20. Comparison of the Predicted Accuracy of the Original Variable-Temperature Model *versus* the Refined Corrected Model at 30 °C with $F_{Total} = 0.36$

Compound	Percent Error (%)*	
	Original Model	Refined Corrected Model
2-Methylpentane	-66.4**	-86.9**
2,4-Dimethylpentane	-33.7	-51.1
Cyclohexane	18.2	0.108
3-Methylhexane	-18.1	-26.1
<i>n</i> -Heptane	-20.6	-23.2
2,3,4-Trimethylpentane	-14.8	-13.6
Toluene	19.8	21.8
Cycloheptane	11.5	15.0
<i>n</i> -Octane	-9.07	-6.08
MAPE	18.2	19.6

* Negative error indicates underprediction of abundance, while positive error indicates overprediction

** Normalized abundance lower than 5% of abundance in unevaporated chromatogram, so error omitted from MAPE calculation

Table A3.21. Comparison of the Predicted Accuracy of the Original Variable-Temperature Model *versus* the Refined Corrected Model at 30 °C with $F_{Total} = 0.55$

Compound	Percent Error (%)*	
	Original Model	Refined Corrected Model
2-Methylpentane	-17.1	-44.5
2,4-Dimethylpentane	-14.5	-23.7
Cyclohexane	8.70	2.94
3-Methylhexane	-12.8	-15.2
<i>n</i> -Heptane	-18.4	-18.3
2,3,4-Trimethylpentane	-11.7	-10.1
Toluene	2.38	4.34
Cycloheptane	2.60	4.95
<i>n</i> -Octane	-9.26	-7.20
MAPE	10.8	14.6

* Negative error indicates underprediction of abundance, while positive error indicates overprediction

Table A3.22. Comparison of the Predicted Accuracy of the Original Variable-Temperature Model *versus* the Refined Corrected Model at 30 °C with $F_{Total} = 0.69$

Compound	Percent Error (%)*	
	Original Model	Refined Corrected Model
2-Methylpentane	-11.8	-27.0
2,4-Dimethylpentane	-4.83	-9.17
Cyclohexane	4.82	2.97
3-Methylhexane	-2.49	-3.00
<i>n</i> -Heptane	-7.77	-7.08
2,3,4-Trimethylpentane	-2.48	-1.06
Toluene	2.86	4.40
Cycloheptane	5.62	7.24
<i>n</i> -Octane	-2.95	-1.50
MAPE	5.06	7.05

* Negative error indicates underprediction of abundance, while positive error indicates overprediction

Table A3.23. Comparison of the Predicted Accuracy of the Original Variable-Temperature Model *versus* the Refined Corrected Model at 30 °C with $F_{Total} = 0.83$

Compound	Percent Error (%)*	
	Original Model	Refined Corrected Model
2-Methylpentane	-9.24	-15.5
2,4-Dimethylpentane	-5.30	-6.55
Cyclohexane	-2.97	-3.16
3-Methylhexane	-6.01	-5.76
<i>n</i> -Heptane	-9.01	-8.36
2,3,4-Trimethylpentane	-2.20	-1.32
Toluene	-3.24	-2.36
Cycloheptane	0.428	1.29
<i>n</i> -Octane	-4.19	-3.40
MAPE	4.73	5.30

* Negative error indicates underprediction of abundance, while positive error indicates overprediction

REFERENCES

REFERENCES

- [1] J.W. McIlroy, A.D. Jones, V.L. McGuffin, Gas chromatographic retention index as a basis for predicting evaporation rates of complex mixtures. *Analytica Chimica Acta* **2014**, 852, 257-266.
- [2] J.W. McIlroy, R. Waddell Smith, V.L. McGuffin, Fixed- and variable-temperature kinetic models to predict evaporation of petroleum distillates for fire debris applications. *Separations* **2018**, 5 (47), 1-19.
- [3] J.L. DeVore, Probability and Statistics for Engineering and the Sciences, Duxbury Press, Belmont, CA, 1990.
- [4] R. Waddell Smith, R.J. Brehe, J.W. McIlroy, V.L. McGuffin, Mathematically modeling chromatograms of evaporated ignitable liquids for fire debris applications, *Forensic Chemistry* 2016, 2, 37-45.
- [5] N.K. Eklund, B.A. Capistran, V.L. McGuffin, R. Waddell Smith, Improvements in a kinetic-based model to predict evaporation of gasoline, *Forensic Chemistry* **2020**, 17, 100194.

IV. Effect of Interface Chemistry on the Evaporation Rate Constants of Different Compound Classes in Diesel Fuel

4.1 Introduction

The importance of understanding the impact of interface when studying evaporation has been demonstrated [1-3]. The persistence through evaporation of compounds commonly found in gasoline and diesel was found to vary between different textiles [1]. Additionally, Frauenhofer *et al.* showed that the molar enthalpy of interaction between substrates and hydrocarbons found in ignitable liquids varies based on both the chemistry and porosity of the substrate as well as the chemistry of the hydrocarbon [2]. Wensel also demonstrated that the presence of a porous substrate causes a deviation in the predicted evaporation of a compound based on its native vapor pressure [3]. While these studies demonstrate that the evaporation rate of a compound is dependent upon the interface on which the evaporation takes place, none of the studies directly measure evaporation rate constants. The aim in the work presented here is to assess the effect of the interface between the liquid and the substrate on the evaporation rate constants of compounds commonly found in ignitable liquids.

Four substrates were investigated in this work: glass, water, cotton fabric, and polyester fabric. The surface chemistry of each interface is shown in Figure 4.1. Borosilicate glass petri dishes were selected because of their use in previous studies using the kinetic model developed by McIlroy *et al.* [4,5]. Additionally, water was included because many of the kinetic models in the literature, including that developed by McIlroy *et al.*, were developed for environmental applications in which evaporation from water was important [4,5]. Cotton and polyester fabric were selected due to their prevalence in typical households and, therefore, their prevalence in fire debris samples. Both fabrics are found in linens such as sheets, drapery, and clothing items. Polyester fibers are also present in some carpets.

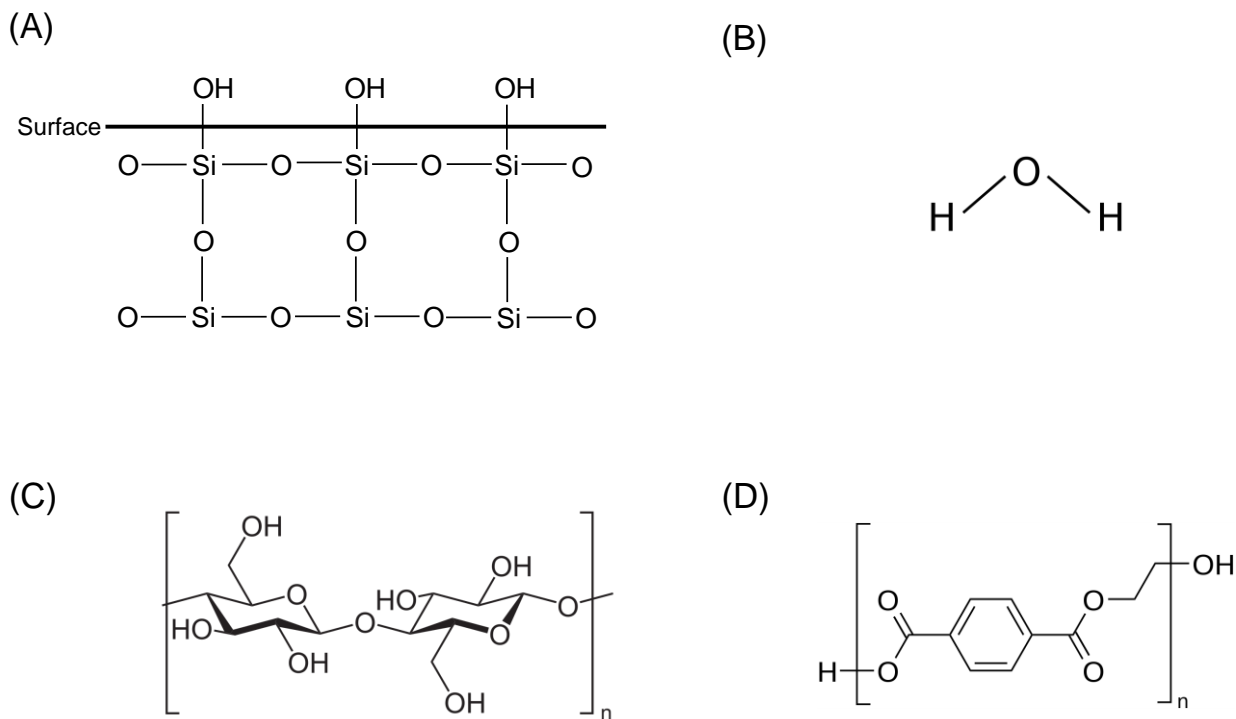


Figure 4.1. Predicted chemistry of the four interfaces under investigation: (A) silica structure at surface of glass petri dishes, (B) water, (C) cellulose present in cotton fabric, and (D) poly(ethylene terephthalate) structure of polyester fabric

Glass dishes exhibit a core structure of repeating siloxane groups with a hydrolyzed surface containing silanol functional groups. While the siloxane groups in the core of the glass are slightly basic, the silanol groups at the surface are slightly acidic and can act as electron acceptors. Silanol groups can either be free (as shown in Figure 4.1 A) or hydrogen bonded to each other ($pK_a = 5.6, 8.5$). Most Lewis acid-base interactions occur at the free silanol groups because these sites preferentially adsorb compounds with lone pairs of electrons [6]. Therefore, the level of interactions occurring is dependent on the proportion of free silanol groups compared to those hydrogen bonded to each other. The hydroxyl groups on the surface of the silica are more acidic than water ($pK_a = 14$), whose structure and behavior are well understood (Figure 4.1 B).

The composition of cotton fabric is over 90% cellulose, a polymer comprised of a chain of glucose molecules (Figure 4.1 C). The different chains of cellulose are held together by hydrogen bonds between the adjacent hydroxyl groups in the crystalline areas of the fiber [7]. In addition to holding the chains together, the hydroxyl groups can also act as sorption sites for water or other compounds with lone pairs of electrons.

Polyester is a synthetic fabric and most commonly refers to poly(ethylene terephthalate) (PET), shown in Figure 4.1 D. PET contains a repeating unit with ester functional groups and a terminal hydroxyl group. While the hydroxyl group at the end of each chain may be slightly acidic, the double bonded oxygen in the repeating unit exhibits basic character due to the lone pair of electrons and the high polarizability.

The effect of interface chemistry on evaporation rate constants was evaluated for homologous series present in diesel fuel. Compounds in a homologous series contain the same functional groups and thus exhibit similar physical properties but differ by the addition of a methylene (CH₂) group. For this study, three homologous series were selected: *n*-alkanes, alkylbenzenes, and alkyl cyclohexanes. These compound classes were chosen due to the expected differences in interactions at the interface based on the chemistry of the compounds. Normal alkanes contain carbon-hydrogen bonds and carbon-carbon single bonds so they are only capable of weak van der Waals dispersion forces and induction forces. Like the *n*-alkanes, cycloalkanes contain only single bonds but have slightly higher boiling points due to the increase in dispersion forces. Finally, the alkylbenzenes contain a conjugated pi (π) system of double bonds that allows for Lewis acid-base interactions. Within each homologous series, four to five compounds were selected, all eluting in the range $I^T = 800 - 1250$. Evaporation rate constants were measured for each compound from each substrate. This allowed a comparison within each

series (*i.e.*, effect of addition of methylene group on rate constant) as well as among substrates with different surface chemistry (*i.e.*, effect of interface interactions). Kinetic models were then developed to predict the evaporation of compounds in a compound class from the substrates investigated.

4.2 Materials and Methods

4.2.1 Sample Collection

Cotton and polyester fabric were obtained from an online source (Amazon.com, Inc., www.amazon.com). The polyester was a 100% polyester poplin fabric with a plain weave (Ben Textiles Inc., Model #EG-403, Los Angeles, CA, USA). A plain weave occurs when a single weft thread alternates over and under a single warp thread. The cotton was a 100% unbleached muslin cotton with a plain weave (Barcelonetta, Model #B08S797QXP, Los Angeles, CA, USA). All of the textiles were free of dyes. Diesel was purchased from a local Speedway gas station in East Lansing, Michigan in October 2020. The fuel was transferred to amber glass bottles and stored at approximately 5 °C until use.

4.2.2 Attenuated Total Reflectance-Fourier Transform Infrared (ATR-FTIR) Spectroscopy

The cotton and polyester fabrics were analyzed using a Perkin Elmer Spectrum One Fourier transform IR spectrometer coupled to an ATR accessory with a diamond Zn/Se one-bounce crystal (Perkin Elmer, Waltham, MA). Each spectrum was collected between 4000 and 550 cm^{-1} using an average of four scans and a resolution of 4 cm^{-1} . The crystal was cleaned with ethanol and a background scan was performed before collecting spectra on the cotton and polyester fabrics. Following data acquisition, baseline correction was performed on each spectrum using the instrument software and the baseline-corrected spectra were smoothed (Spectrum v.10.4.4, Perkin Elmer). The spectra were then compared to reference spectra of

cotton and poly(ethylene terephthalate) from the Institute of Chemistry at the University of Tartu, Estonia [8].

4.2.3 Experimental Evaporation

Diesel was evaporated from each substrate at 20 °C in the evaporation chamber described by McIlroy *et al.* and discussed in Chapter 3 [1,2]. Circular samples (2.4” diameter) of each fabric were cut to fit inside the petri dishes used for evaporation. For each evaporation, a 1-mL aliquot of diesel was added to each of 24 petri dishes (60 mm ID x 15 mm), either empty (glass substrate) or containing water (15 mL), cotton or polyester fabrics. Throughout the evaporation, petri dishes were removed at nine specific time points. The selection of time points was based on the 300 h evaporations performed by McIlroy *et al.* using diesel [1].

For the diesel evaporation from the glass dish, on removal from the chamber, a series of 1-mL aliquots of dichloromethane (CH_2Cl_2) was pipetted into the petri dish. The mixture was then transferred into a 10-mL volumetric flask, and further diluted to the mark with CH_2Cl_2 . For the diesel evaporation from water, a 1-mL aliquot of CH_2Cl_2 was pipetted into the dish and the water/diesel/ CH_2Cl_2 mixture was quantitatively transferred to a separatory funnel. The dish was then rinsed with a series of additional CH_2Cl_2 aliquots that were added to the original mixture in the separatory funnel. The organic layer was transferred to a 10-mL volumetric flask and diluted in CH_2Cl_2 . For the diesel evaporations from both cotton and polyester fabrics, a series of 1-mL aliquots of CH_2Cl_2 was pipetted onto the fabric and transferred into a 10-mL volumetric flask. The fabric was then held with forceps, rinsed further with CH_2Cl_2 , and the mixture added to the same volumetric flask, which was then diluted further with CH_2Cl_2 . All evaporated samples were then transferred to GC vials and analyzed in triplicate by GC-MS.

4.2.4 Gas Chromatography-Mass Spectrometry Analysis

The GC-MS system consisted of an Agilent 6890N gas chromatograph coupled to an Agilent 5975C mass spectrometer with an Agilent 7683A injector (Agilent Technologies, Santa Clara, CA, USA). The GC contained a 100%-dimethylpolysiloxane column (30 m x 0.25 mm ID x 0.25 μ m film thickness, Agilent Technologies). The injection temperature was 250 °C and 1 μ L of sample was injected in pulsed split mode (15 psi for 0.25 min, 50:1 split). Ultra-high purity helium (Airgas, Radnor Township, PA, USA) was used as the carrier gas with a nominal flow rate of 1 mL/min. The oven temperature program was as follows: initial temperature 50 °C ramped at 5 °C/min to 280 °C, final hold for 4 min. The transfer line to the mass spectrometer was maintained at 280 °C. Electron ionization was employed at 70 eV and the mass spectral scan range was m/z 40 – 550, with a scan rate of 2.83 scans/s. The temperature of the ion source was 230 °C, while the temperature of the quadrupole mass analyzer was 150 °C.

4.2.5 Data Analysis

The chromatographic data were exported from ChemStation (version E.01.00.237, Agilent Technologies) into Microsoft Excel (version 16.20, Microsoft Corp., Redmond, WA, USA) for further processing. Three homologous series representing separate compound classes were identified in diesel and used for this study: *n*-alkanes (*n*-octane, *n*-nonane, *n*-decane, *n*-undecane, and *n*-dodecane), alkylbenzenes (ethylbenzene, propylbenzene, butylbenzene, and pentylbenzene), and alkyl cyclohexanes (ethylcyclohexane, propylcyclohexane, butylcyclohexane, pentylcyclohexane, and hexylcyclohexane). Extracted ion chromatograms (EICs) representative of each group were used for model development. The EICs used were m/z 57, m/z 91, and m/z 83 for the *n*-alkanes, alkylbenzenes, and alkyl cyclohexanes, respectively. Retention indices were determined for each compound using Eq. 3.1 and decay curves were

generated using the same methods discussed in Chapter 3, Section 3.2.5. Class-specific regression models were then developed for each interface according to Eq. 3.2.

4.3 Results

4.3.1 ATR-FTIR Spectroscopy

The IR spectra of the cotton and polyester fabric were compared to reference spectra from the Institute of Chemistry at the University of Tartu, Estonia [8] and were consistent with cellulose and poly(ethylene terephthalate), respectively (Figure 4.1 C and D). The strong, broad peak at 3333 cm^{-1} in the IR spectrum for the cotton fabric is indicative of O-H stretch, which would be expected based on the prevalence of hydroxyl groups in cellulose (Figure 4.2). Additionally, the peaks at 1107 and 1160 cm^{-1} are consistent with the asymmetric stretching of the ether groups that link the glucose molecules. The reference spectrum for cotton is shown in the Appendix (Figure A 4.1).

The IR spectrum for polyester is consistent with poly(ethylene terephthalate), the most common type of polyester. The strong peak at 1713 cm^{-1} represents the C=O stretch in the ester functional group. Additional ester C=O stretch peaks occur at 1230 and 1090 cm^{-1} . The peaks at 1340 and 871 cm^{-1} represent the CH₂ wag and rock of the glycol functional group, respectively. The reference spectrum for polyester is shown in the Appendix (Figure A 4.2).

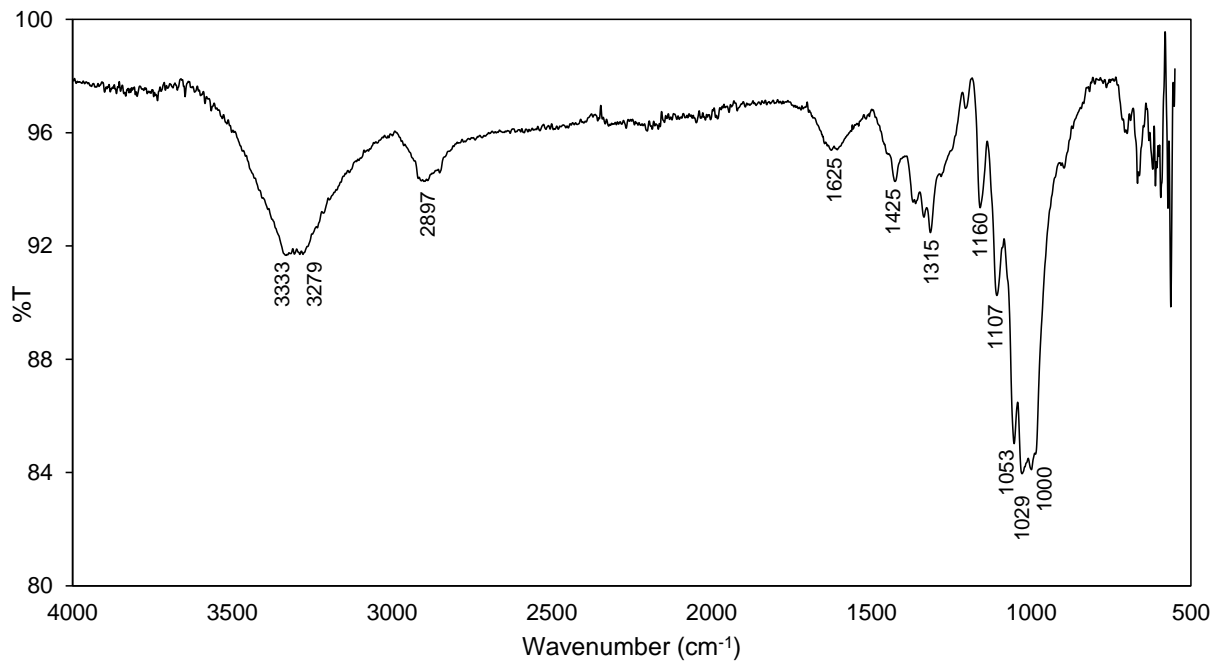


Figure 4.2. ATR-FTIR spectrum for cotton fabric

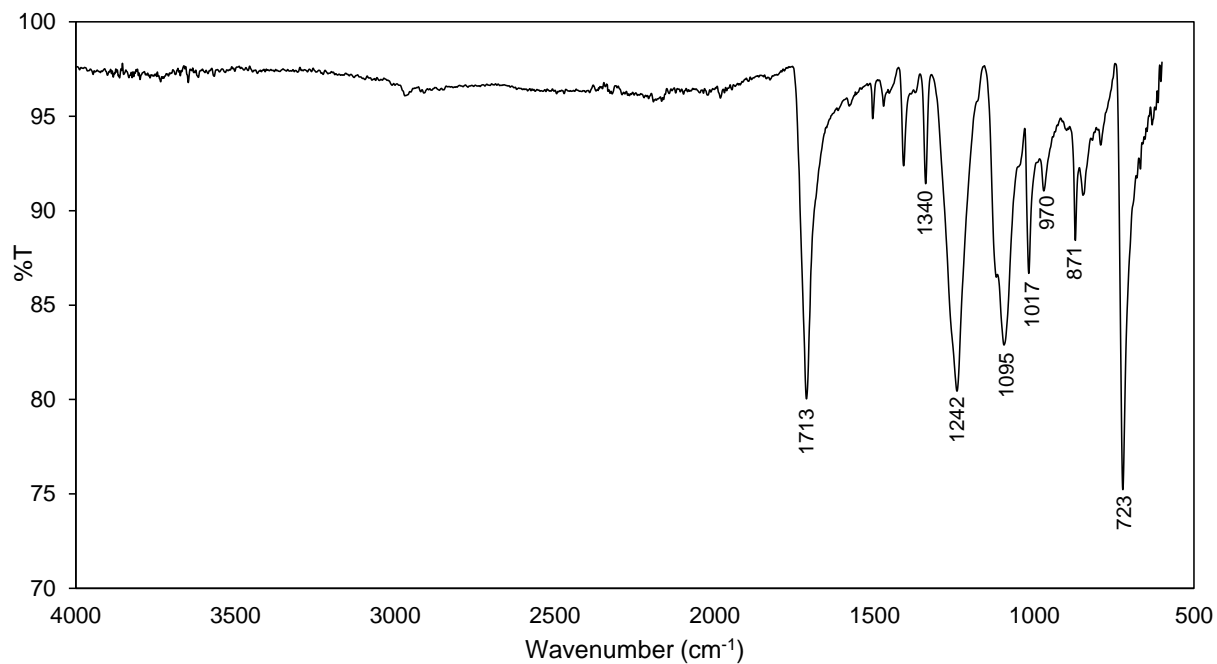


Figure 4.3. ATR-FTIR spectrum for polyester fabric

4.3.2 Development of Substrate-Specific Models based on *n*-Alkanes

The first homologous series investigated was the *n*-alkanes, ranging from *n*-octane to *n*-dodecane ($I^T = 800 - 1200$). Representative decay curves for the evaporation of the *n*-alkane of intermediate volatility in the series (*n*-decane, $I^T = 1000$) from the four interfaces are shown in Figure 4.4. The equation of the fit to a first-order kinetic decay is shown for each interface with the evaporation rate constant highlighted in red. The quality of fit for *n*-decane from each interface exceeded $R^2 = 0.9795$, indicating that the evaporation consistently behaved according to a first-order decay. The smallest evaporation rate constant was observed for *n*-decane from the petri dish, with a rate of 0.0122 h^{-1} . The evaporation rate was similar for water and polyester, with evaporation rate constants of 0.0134 and 0.0131 h^{-1} , respectively. The fastest evaporation for *n*-decane was observed from the cotton, with a rate constant of 0.0150 h^{-1} . The remaining rate constants, as well as the R^2 values, for the other *n*-alkanes from the four interfaces are listed in Table 4.1.

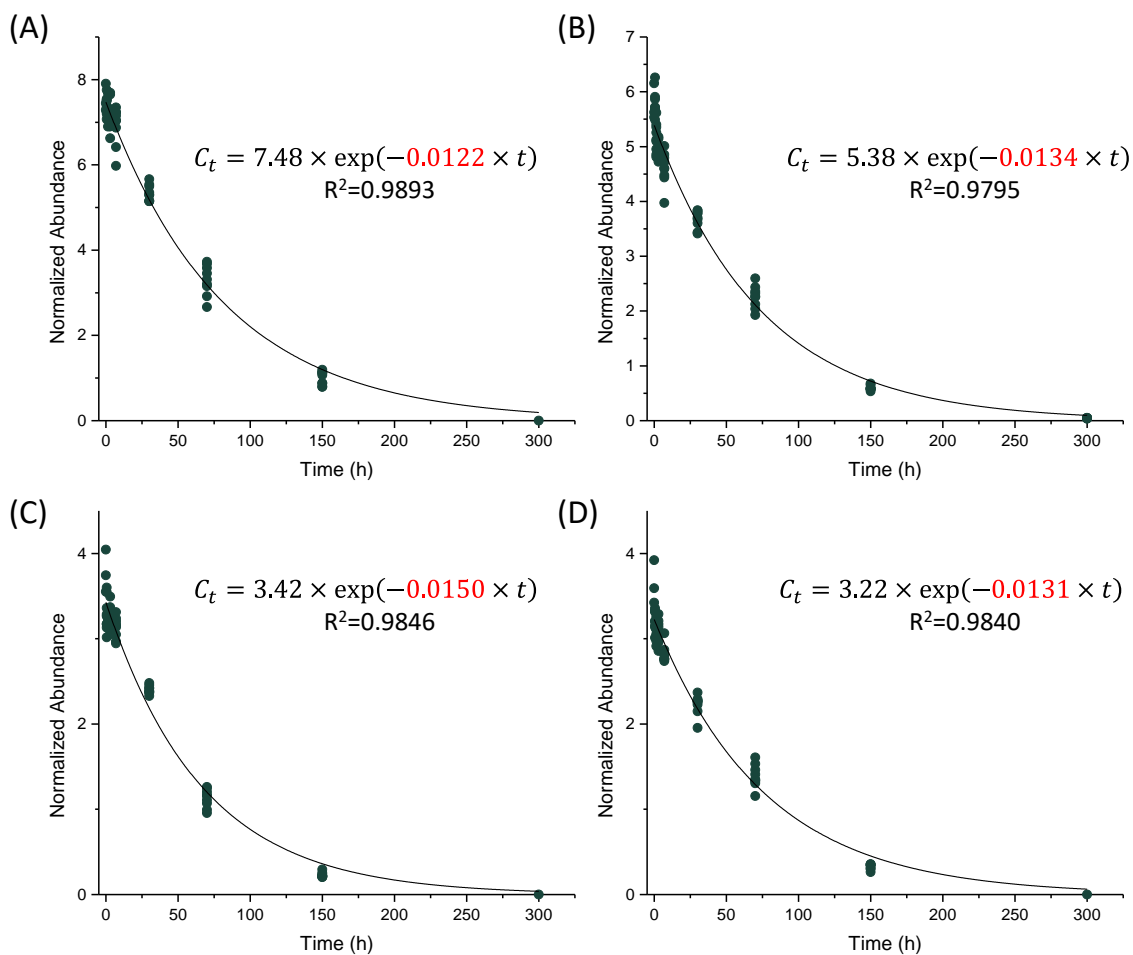


Figure 4.4. Representative decay curves for *n*-decane from (A) glass dish, (B) water, (C) cotton fabric, and (D) polyester fabric at 20 °C

Table 4.1. Comparison of the Evaporation Rate Constants of the Normal Alkanes from Various Interfaces at 20 °C

Compound	Evaporation Rate Constant (h ⁻¹)			
	Glass Dish	Water	Cotton Fabric	Polyester Fabric
<i>n</i> -Octane (<i>I</i> ^T = 800)	0.108 (<i>R</i> ² = 0.9700)	0.162 (<i>R</i> ² = 0.9411)	0.169 (<i>R</i> ² = 0.9460)	0.140 (<i>R</i> ² = 0.9343)
<i>n</i> -Nonane (<i>I</i> ^T = 900)	0.0323 (<i>R</i> ² = 0.9904)	0.0368 (<i>R</i> ² = 0.9746)	0.0443 (<i>R</i> ² = 0.9773)	0.0366 (<i>R</i> ² = 0.9830)
<i>n</i> -Decane (<i>I</i> ^T = 1000)	0.0122 (<i>R</i> ² = 0.9893)	0.0134 (<i>R</i> ² = 0.9795)	0.0150 (<i>R</i> ² = 0.9846)	0.0131 (<i>R</i> ² = 0.9840)
<i>n</i> -Undecane (<i>I</i> ^T = 1100)	0.00468 (<i>R</i> ² = 0.9680)	0.00530 (<i>R</i> ² = 0.9553)	0.00509* (<i>R</i> ² = 0.9467)	0.00516 (<i>R</i> ² = 0.9624)
<i>n</i> -Dodecane (<i>I</i> ^T = 1200)	0.00130 (<i>R</i> ² = 0.7992)	0.00151 (<i>R</i> ² = 0.7026)	0.00180* (<i>R</i> ² = 0.8219)	0.00155 (<i>R</i> ² = 0.8602)

*Denotes compounds affected by mold observed at 300-h time point. Omitting the 300-h time point, *k* for *n*-undecane and *n*-dodecane is 0.00434 and 0.000938 h⁻¹, respectively.

Consistently, the lowest evaporation rate constants for the *n*-alkanes were observed from the glass surface (Table 4.1). The dishes are comprised of borosilicate glass with basic siloxane groups throughout the bulk and hydrolyzed silanol groups at the surface that exhibit acidic behavior. The slower evaporation from the glass could be due to enhanced interactions with the silanol surface or due to the physical characteristics of the surface. The dishes are slightly concave, meaning that the center of the dish is higher than the outer edges. As the evaporation proceeds and the volume of the liquid decreases, it is possible that the liquid spreads to the outer edges of the dish. As the liquid sinks to the lower regions, the thickness of the film would increase because it is spread over a smaller surface area. This increase in film thickness may be responsible for the slower evaporation kinetics, as the mass transfer of individual compounds in the liquid is different than that in a thinner film.

The evaporation rate constants for the *n*-alkanes were very similar from water and polyester fabric with the exception of *n*-octane, which evaporated more quickly from water than polyester (0.162 h⁻¹ from water and 0.140 h⁻¹ from polyester, Table 4.1). However, *n*-octane contained the greatest uncertainty in the fit for the first-order decay due to the high volatility and, thus, low number of data points collected before full evaporation. The similarity in rate constants for the *n*-alkanes from water and polyester indicates that the interactions between the alkanes and these interfaces were also similar. Alkanes exhibit dispersion and induction forces because they are nonpolar straight-chain hydrocarbons. The dispersion forces between the *n*-alkanes and water are likely to be similar to those between the *n*-alkanes and polyester.

From cotton fabric, the evaporation rate constants were higher than any of the other three substrates for *n*-octane, *n*-nonane, and *n*-decane (Table 4.1). Between the last two time points (150 and 300 h), mold developed on the cotton fabric, likely affecting the data for the final time point. The presence of microbes has been shown to contribute to microbial degradation of hydrocarbons [9], which would cause the chromatographic abundance at the final time point to be lower than expected. This error would cause the evaporation rate constant to be higher than the true value if evaporation was the only contribution to abundance. Straight-chain alkanes have been found to be more susceptible to microbial degradation than other branched and cyclic hydrocarbons. Therefore, an evaporation rate constant was also determined for *n*-undecane and *n*-dodecane with the final 300 h time point omitted.

When omitting the final time point for *n*-undecane and *n*-dodecane from cotton, the evaporation rate constants were smaller than any of the other substrates, a trend not observed for the three most volatile *n*-alkanes from cotton. The evaporation rate constants for *n*-undecane and *n*-dodecane with the omission of the 300 h time point were 0.00434 h⁻¹ and 0.000938 h⁻¹,

respectively (Table 4.1), although only 0.65τ and 0.14τ were achieved by 150 h for these compounds, respectively. The lower rate constants suggest that the dispersion forces increased with additional methylene groups and caused a greater adsorption of larger *n*-alkanes to cotton compared to the other interfaces. This greater adsorption could also be due to a porosity difference between cotton and the other substrates. Diesel fuel forms a thin layer at the interface with water and the glass dish but can be adsorbed into the fabrics. Cotton is known to contain pores that run the length of the fiber, whereas polyester fibers contain no voids. This difference in porosity may allow for more adsorption of the *n*-alkanes to cotton compared to the polyester fabric and, therefore, lead to slower evaporation kinetics.

The evaporation rate constant for each compound on each interface was plotted as a function of I^T and linear regression was performed (Figure 4.5 and Table 4.1). Despite the observed differences in rate constant, the linear regression coefficients were similar across all four interfaces. This is unsurprising due to the presence of only dispersion and induction forces between *n*-alkanes and any particular interface. Because of the nonpolar nature of the compounds in this homologous series, no specific interactions occur, and the adsorption of the hydrocarbons is similar for all interfaces. The slope of the regression relates rate constant to I^T . The four models, as well as the original model by McIlroy *et al.* for the *n*-alkanes [4], exhibit similar slopes indicating that the relationship between evaporation rate constant and I^T is consistent across the four interfaces for the *n*-alkanes. The changes in the magnitude of the rate constants are demonstrated by the intercept. The small intercept for the regression model for the glass surface is due to the smaller measured rate constants for the *n*-alkanes from this interface. Because the rate constants from the other three substrates had similar magnitudes, the intercepts are also similar (Table 4.2).

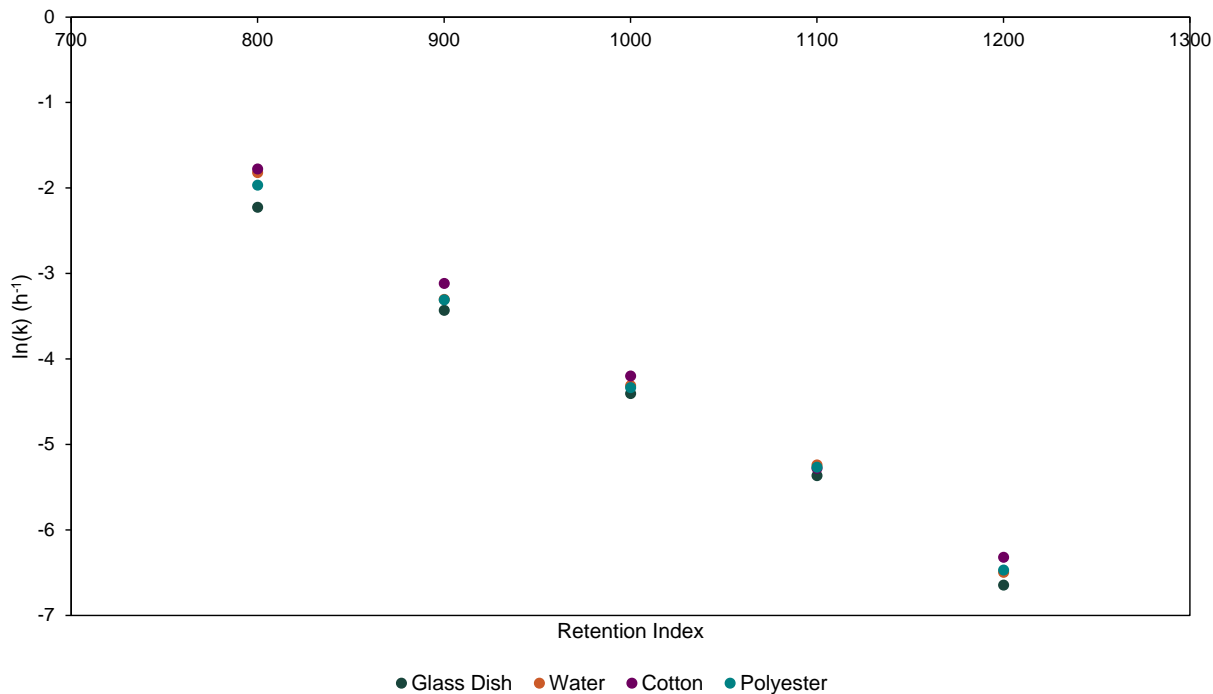


Figure 4.5. Interface-specific models for the *n*-alkanes at 20 °C. Linear regression shown in Table 4.2.

Table 4.2. Comparison of the Linear Regression Models for each Interface for the *n*-Alkanes at 20°C. For each model, the slope (*m*), intercept (*b*), and coefficient of determination (*R*²) are shown.

Model	<i>m</i>	<i>b</i>	<i>R</i>²
Glass Dish	-0.0108	6.36	0.9972
Water	-0.0113	7.05	0.9934
Cotton	-0.0112	7.11	0.9975
Polyester	-0.0110	6.70	0.9963
Original (water) [4]	-0.0114	7.61	0.9990

4.3.3 Development of Substrate-Specific Models based on Alkylbenzenes

The second homologous series investigated was the alkylbenzenes, ranging from ethylbenzene to pentylbenzene ($I^T = 844 - 1141$). Representative decay curves for the evaporation of the alkylbenzene of intermediate volatility in the series (butylbenzene, $I^T = 1040$) from the four interfaces are shown in Figure 4.6. The quality of fit for butylbenzene from each interface exceeded $R^2 = 0.9793$, indicating a consistency with the first-order kinetic decay. Like the *n*-alkanes, the smallest evaporation rate constant was observed for butylbenzene from the petri dish, with a rate of 0.0105 h^{-1} . The evaporation rate was also similar for water and polyester, with evaporation rate constants of 0.0124 and 0.0119 h^{-1} , respectively. The quickest evaporation for butylbenzene was observed from cotton, with a rate constant of 0.0132 h^{-1} , although the increase was less than that for *n*-decane from cotton compared to the other interfaces. The remaining rate constants, as well as the R^2 values, for the other alkylbenzenes from the four interfaces are listed in Table 4.3.

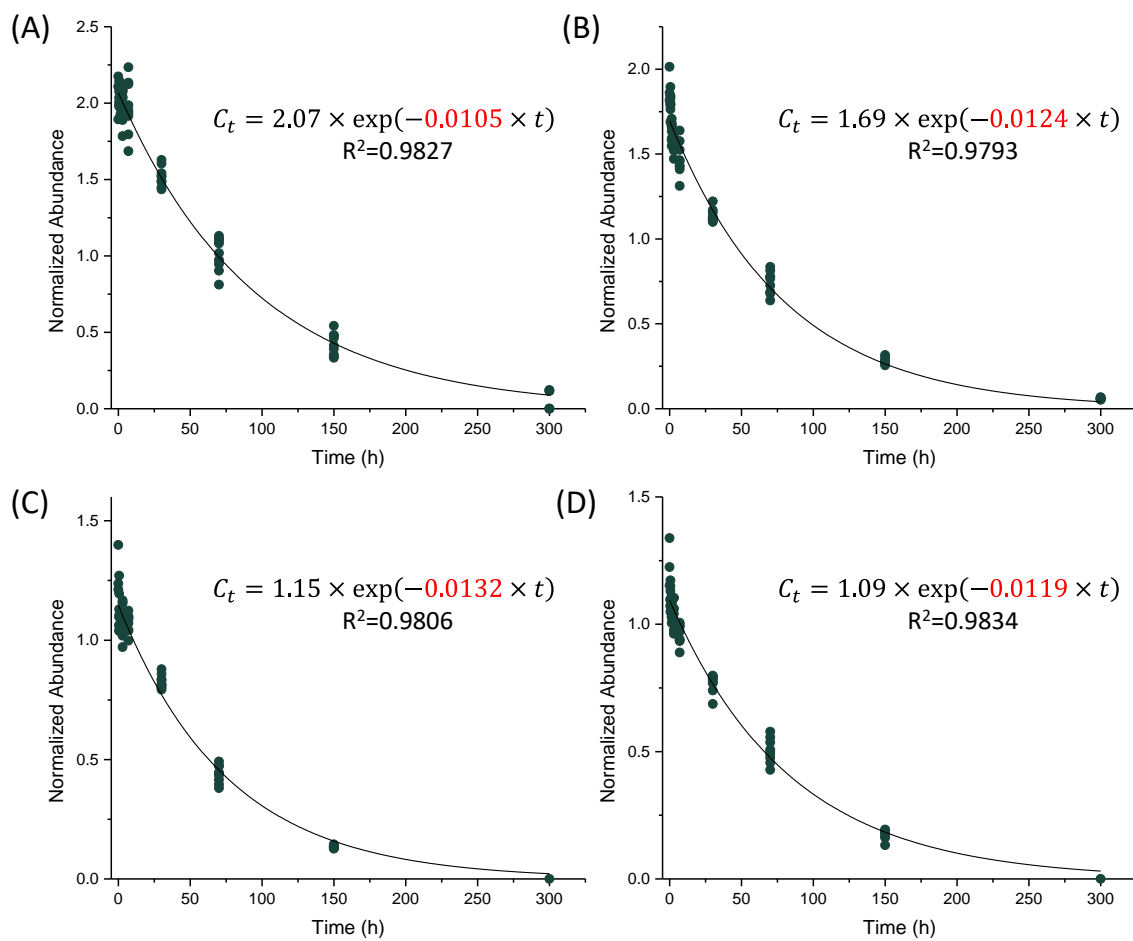


Figure 4.6. Representative decay curves for butylbenzene from (A) glass dish, (B) water, (C) cotton fabric, and (D) polyester fabric at 20 °C

Table 4.3. Comparison of the Evaporation Rate Constants of the Alkylbenzenes from Various Interfaces at 20 °C

Compound	Evaporation Rate Constant (h ⁻¹)			
	Glass Dish	Water	Cotton Fabric	Polyester Fabric
Ethylbenzene (<i>I</i> ^T = 844)	0.0685 (<i>R</i> ² = 0.9844)	0.113 (<i>R</i> ² = 0.9574)	0.111 (<i>R</i> ² = 0.9636)	0.0957 (<i>R</i> ² = 0.9630)
Propylbenzene (<i>I</i> ^T = 938)	0.0265 (<i>R</i> ² = 0.9877)	0.0324 (<i>R</i> ² = 0.9744)	0.0373 (<i>R</i> ² = 0.9813)	0.0314 (<i>R</i> ² = 0.9809)
Butylbenzene (<i>I</i> ^T = 1040)	0.0105 (<i>R</i> ² = 0.9827)	0.0124 (<i>R</i> ² = 0.9793)	0.0132 (<i>R</i> ² = 0.9806)	0.0119 (<i>R</i> ² = 0.9834)
Pentylbenzene (<i>I</i> ^T = 1141)	0.00394 (<i>R</i> ² = 0.9329)	0.00522 (<i>R</i> ² = 0.9513)	0.00502* (<i>R</i> ² = 0.9467)	0.00478 (<i>R</i> ² = 0.9649)

*Denotes compounds affected by mold observed at 300-h time point. Omitting the 300-h time point, *k* for pentylbenzene is 0.00416 h⁻¹.

Like the *n*-alkanes, the smallest evaporation rate constants for the alkylbenzenes were observed from the glass dish. The rate constant for ethylbenzene from the dish is almost half of that from the water (0.0685 h⁻¹ compared to 0.113 h⁻¹). In addition to the dispersion and induction forces exhibited by the *n*-alkanes, the alkylbenzenes also have stronger dipole – dipole interactions. The alkylbenzenes serve as electron donors with the addition of a methyl group that effects the electron density and causes increased polarizability. Subsequent addition of methylene groups will have less of an effect, as the electron density is held more tightly within the C-C single bond. The silanol groups on the surface of the glass dish are slightly more acidic than the water molecules, causing stronger specific (Lewis acid-base) interactions with the alkylbenzenes and a slower evaporation rate constant.

The alkylbenzenes exhibit very similar kinetics for evaporation from water and cotton. The similarity in acidity between the hydroxyl groups in both the water and cellulose substrates causes similar acid-base interactions with the electron-donating benzene ring [10]. Of the two

fabrics studied, the rate constants were smaller for the polyester, indicating that the benzene ring of the alkylbenzenes interacts more strongly with the polyester. Because there is only a singular terminal hydroxyl group in each PET polymer, the alkylbenzenes are likely interacting with the aromatic rings in the polymer.

The plot of evaporation rate constant versus I^T is shown in Figure 4.7 with the linear regression coefficients for each model listed in Table 4.4. The slopes are similar for all interfaces, suggesting a consistency in the relationship between evaporation rate constant and I^T . Similar to the *n*-alkanes, the smallest slope was observed for the glass dish model and the largest for the original model developed by McIlroy *et al.* [4]. The models for the water, cotton, and polyester exhibited very similar slopes.

While the biggest difference in intercept for the *n*-alkane models was 0.75 between the glass dish and cotton fabric, the difference between these two interfaces for the alkylbenzene models was 1.15. This suggests that there was a greater difference in molecular interactions between these two interfaces for the alkylbenzenes compared to the *n*-alkanes, due to the introduction of specific Lewis acid-base interactions. While the *n*-alkanes exhibited mainly dispersion forces with some induction forces, the benzene ring of the alkylbenzenes served as an electron donor. The acidity difference in the hydroxyl group between the silanol on the glass dish and cotton was more important, therefore, for the alkylbenzenes that could participate in specific interactions.

Overall, the similar slopes for the substrate-specific alkylbenzene models suggests that the dependence of I^T on the rate constant was consistent across the different substrates. However, the difference in intercepts indicates that the extent of interaction between the alkylbenzenes and

the substrates differed due to the aromatic ring allowing for more specific interactions with substrates of higher acidity or those containing benzene rings.

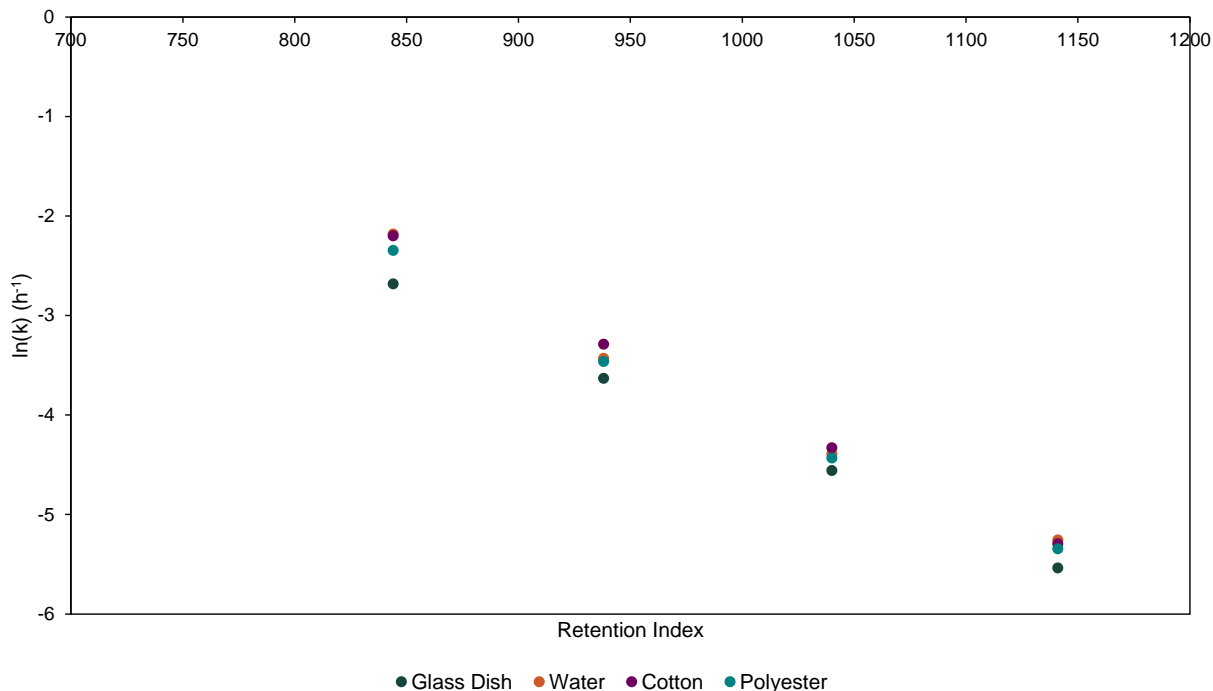


Figure 4.7. Interface-specific models for the alkylbenzenes at 20 °C. Linear regression shown in Table 4.4.

Table 4.4. Comparison of the Linear Regression Models for each Interface for the Alkylbenzenes at 20 °C. For each model, the slope (m), intercept (b), and coefficient of determination (R^2) are shown.

Model	m	b	R^2
Glass Dish	-0.00956	5.37	0.9996
Water	-0.0102	6.33	0.9893
Cotton	-0.0104	6.52	0.9981
Polyester	-0.0100	6.03	0.9960
Original (water) [4]	-0.0108	7.20	0.9920

4.3.4 Development of Substrate-Specific Models based on Alkyl Cyclohexanes

The final homologous series investigated in this work was the alkyl cyclohexanes, ranging from ethylcyclohexane to hexylcyclohexane ($I^T = 828 - 1241$). Representative decay curves for the evaporation of the alkyl cyclohexane of intermediate volatility in the series (butylcyclohexane, $I^T = 1027$) from the four interfaces is shown in Figure 4.8. The quality of fit for butylcyclohexane from each interface exceeded $R^2 = 0.975$ and, like the previous two series, the smallest evaporation rate constant was observed from the glass dish, with a rate of 0.0101 h^{-1} . The evaporation rate was also similar for water and polyester, with evaporation rate constants of 0.0121 and 0.0119 h^{-1} , respectively. The fastest evaporation for butylcyclohexane was observed from cotton, with a rate constant of 0.0137 h^{-1} . The remaining rate constants, as well as the R^2 values, for the other alkyl cyclohexanes from the four interfaces are listed in Table 4.5.

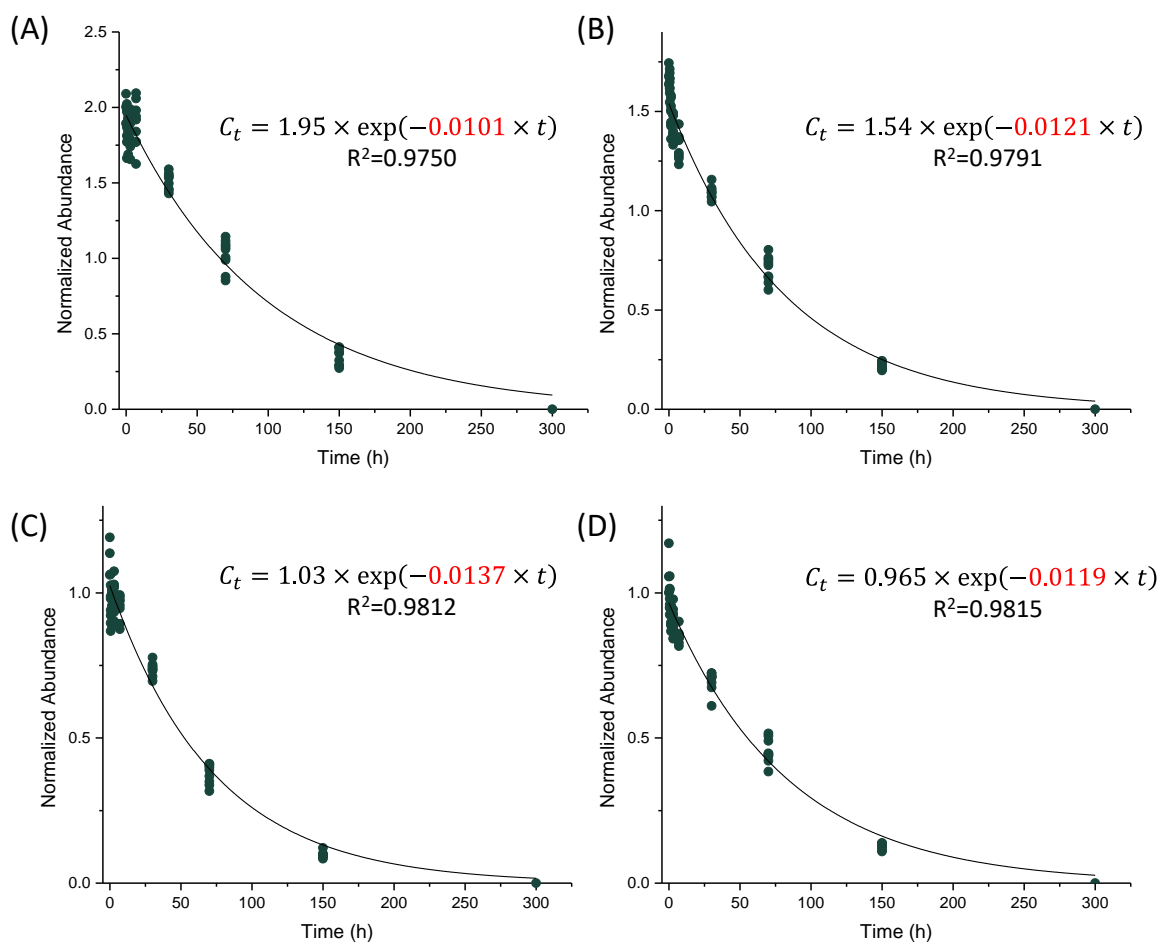


Figure 4.8. Representative decay curves for butylcyclohexane from (A) glass dish, (B) water, (C) cotton fabric, and (D) polyester fabric at 20 °C

Table 4.5. Comparison of the Evaporation Rate Constants of the Alkyl Cyclohexanes from Various Interfaces at 20 °C

Compound	Evaporation Rate Constant (h ⁻¹)			
	Glass Dish	Water	Cotton Fabric	Polyester Fabric
Ethylcyclohexane (<i>I</i> ^T = 828)	0.0755 (<i>R</i> ² = 0.9805)	0.128 (<i>R</i> ² = 0.9524)	0.117 (<i>R</i> ² = 0.9599)	0.107 (<i>R</i> ² = 0.9606)
Propylcyclohexane (<i>I</i> ^T = 925)	0.0263 (<i>R</i> ² = 0.9848)	0.0321 (<i>R</i> ² = 0.9749)	0.0396 (<i>R</i> ² = 0.9765)	0.0316 (<i>R</i> ² = 0.9804)
Butylcyclohexane (<i>I</i> ^T = 1027)	0.0101 (<i>R</i> ² = 0.9750)	0.0121 (<i>R</i> ² = 0.9791)	0.0137 (<i>R</i> ² = 0.9812)	0.0119 (<i>R</i> ² = 0.9815)
Pentylcyclohexane (<i>I</i> ^T = 1130)	0.00379 (<i>R</i> ² = 0.9295)	0.00486 (<i>R</i> ² = 0.9483)	0.00486* (<i>R</i> ² = 0.9393)	0.00470 (<i>R</i> ² = 0.9636)
Hexylcyclohexane (<i>I</i> ^T = 1241)	0.000858 (<i>R</i> ² = 0.5678)	0.00160 (<i>R</i> ² = 0.7629)	0.00186* (<i>R</i> ² = 0.8175)	0.00159 (<i>R</i> ² = 0.8813)

*Denotes compounds affected by mold found at 300-h time point. Omitting the 300-h time point, *k* for propylcyclohexane and hexylcyclohexane is 0.00378 and 0.000857 h⁻¹, respectively.

The smallest evaporation rate constants for the alkyl cyclohexanes were measured from the glass dish (Table 4.5), which was in agreement with trends observed for the *n*-alkanes and alkylbenzenes (Table 4.1 and 4.3, respectively). However, many of the rate constants were smaller for the alkyl cyclohexanes compared to the alkylbenzenes of the same carbon number. For example, the rate constant for propylcyclohexane (*I*^T = 925) from the glass dish was 0.0263 h⁻¹, whereas that for propylbenzene (*I*^T = 938) was 0.0265 h⁻¹. Given that propylcyclohexane has a lower retention index than propylbenzene, the expected rate constant would be larger. Butylcyclohexane and pentylcyclohexane also exhibited smaller rate constants than the alkylbenzenes with the same number of carbons. This suggests that the alkyl cyclohexanes either adsorb or interact more with the glass dish than the alkylbenzenes, despite the lack of aromaticity that makes the alkylbenzenes better electron donors. The alkyl cyclohexanes are expected to

exhibit dispersion forces, which should be stronger than the dispersion forces observed for the *n*-alkanes of the same carbon number, induction forces, and weak dipole – dipole interactions. However, the alkyl cyclohexanes should have weaker overall interactions than the alkylbenzenes, which exhibit all of the same interactions as the cyclohexanes in addition to Lewis acid – base interactions. The fact that the rate constants for the alkyl cyclohexanes were smaller than the alkylbenzene counterparts is an area for future study.

The evaporation rate constants for the alkyl cyclohexanes from water and polyester are similar, suggesting similar interactions between the hydrocarbons and these two interfaces. Like the other two homologous series under investigation, the rate constants for the alkyl cyclohexanes from polyester were smaller than those from cotton. This indicates that either the polyester exhibits stronger intermolecular forces with the alkyl cyclohexanes than the cotton, or there is a physical property such as porosity causing the enhanced adsorption. Unlike the results from the glass dish, the rate constants for the alkyl cyclohexanes from cotton are generally larger than those of the alkylbenzenes of the same carbon number, as expected based on I^T . This means that the alkyl cyclohexanes are interacting with the cotton surface as expected based on the predicted intermolecular forces.

The plot of evaporation rate constant versus I^T for the alkyl cyclohexanes from the four interfaces is shown in Figure 4.9 with the regression coefficients for each model listed in Table 4.6. Of the four substrates studied, the glass dish had the largest slope and the other three (water, cotton, and polyester) contained very similar slopes. The intercepts were also similar, with the polyester fabric exhibiting the smallest.

For all homologous series, evaporation from glass resulted in the smallest rate constants. For the *n*-alkanes and alkylbenzenes, the smallest slope and intercept were also observed for the

glass dish models. However, the regression for evaporation of the alkyl cyclohexanes from the glass dish exhibited the largest slope of the four interfaces investigated. Only the original model developed by McIlroy *et al.* [4] had a larger slope (Table 4.6). The larger slope for the glass dish model compared to the other three interfaces (*i.e.*, water, cotton, and polyester) indicates that there was a larger spread in the evaporation rate constants between the most and least volatile compounds. The other three interfaces, on the other hand, had a smaller spread which could be indicative of enhanced adsorption with a longer alkyl chain.

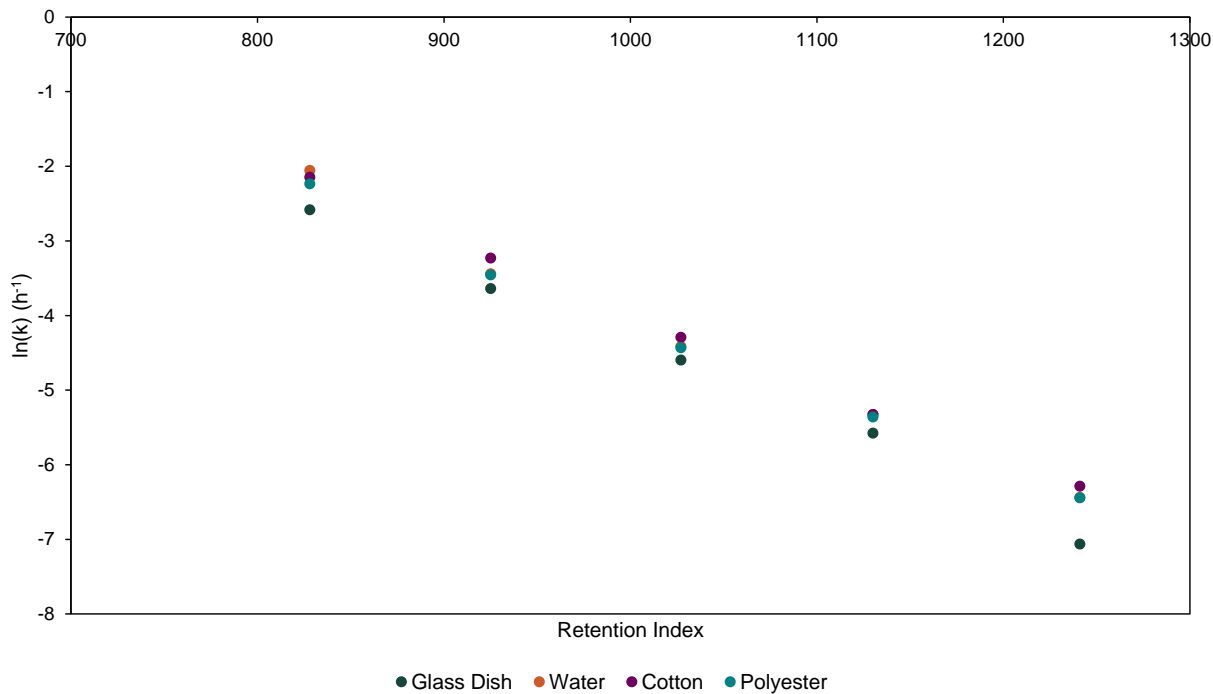


Figure 4.9. Interface-specific models for the alkyl cyclohexanes at 20 °C. Linear regression shown in Table 4.6.

Table 4.6. Comparison of the Linear Regression Models for each Interface for the Alkyl Cyclohexanes at 20 °C. For each model, the slope (m), intercept (b), and coefficient of determination (R^2) are shown.

Model	m	b	R^2
Glass Dish	-0.0106	6.21	0.9952
Water	-0.0103	6.29	0.9919
Cotton	-0.0101	6.11	0.9978
Polyester	-0.0100	5.92	0.9962
Original [4]	-0.0108	7.16	0.9989

4.4 Conclusions

In this work, evaporation rate constants were determined for compounds in three different compound classes from various interfaces. Experimental evaporations were performed at 20 °C using diesel and rate constants were measured for *n*-alkanes, alkylbenzenes, and alkyl cyclohexanes from a glass dish, water, cotton fabric, and polyester fabric. Interface-specific models were then developed for each series of compounds to determine the effect of each interface on the relationship between evaporation rate constant and retention index. Overall, the glass dish had the largest effect on the evaporation rate constants of compounds in all three classes. The measured rate constants were consistently smaller from the glass dish, suggesting either enhanced interactions between the hydrocarbons and the glass or a physical difference in the spreading of the diesel over the surface.

The evaporation rate constants from water, cotton, and polyester were similar within each of the three series of compounds. This suggests that the interactions between the compounds and interfaces did not differ substantially among the three interfaces. Consistently, the rate constants from polyester were marginally smaller than from water and cotton. Water and cotton both contain hydroxyl groups that contribute to Lewis acid-base interactions and, because the acidity of the hydroxyl groups is similar, it was expected that the interactions with the compounds were similar. The smaller rate constants from the polyester could be due to the different chemistry of the polymer, which contained basic ester groups, or could be attributed to porosity differences. Future work should explore the mechanisms of interactions and differentiate the contributions of chemistry and porosity to the adsorption of the hydrocarbons.

APPENDIX

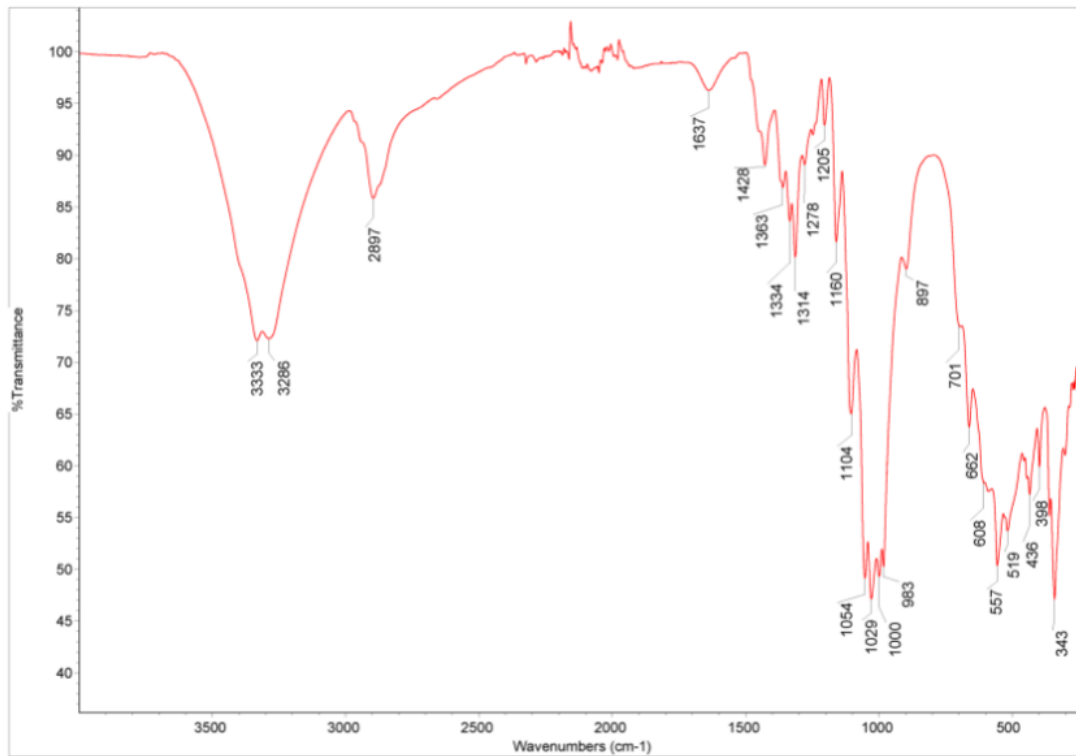


Figure A4.1. Reference ATR-FTIR spectrum for cotton [8]

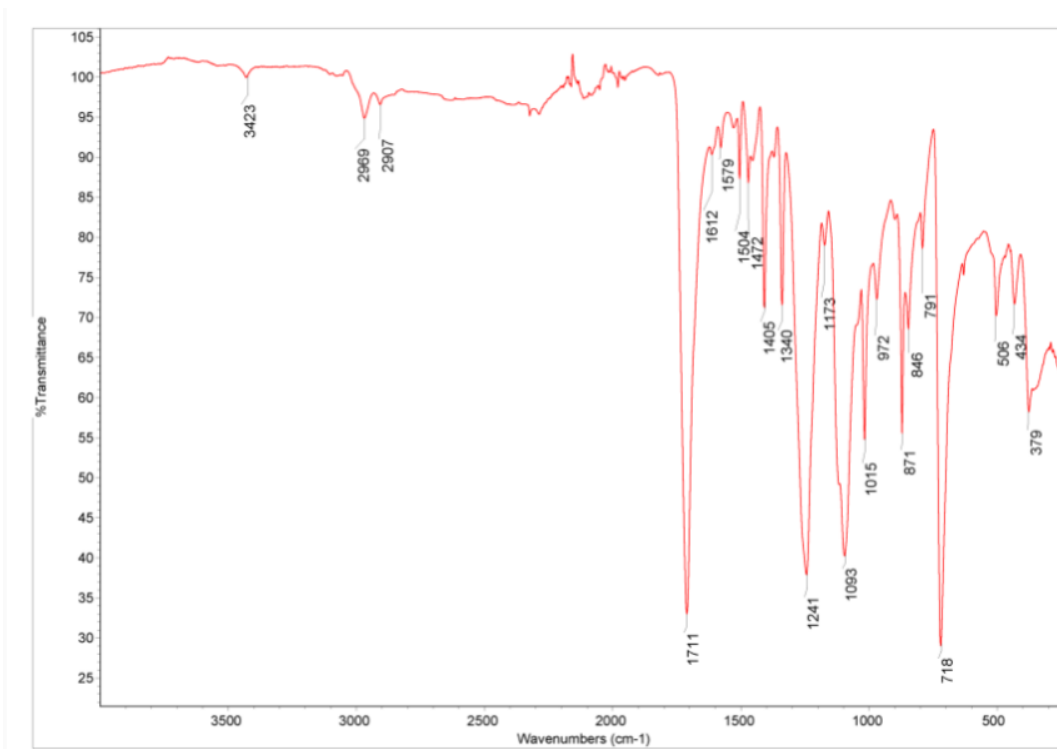


Figure A4.2. Reference ATR-FTIR spectrum for poly(ethylene terephthalate) [8]

REFERENCES

REFERENCES

- [1] A. Aqel, A. M. Dhabbah, K. Yusuf, N. M. Al-Harbi, Z. A. Al Othman, A. Y. Badjah-Hadj-Ahmed, Determination of gasoline and diesel residues on wool, silk, polyester, and cotton materials by SPME-GC-MS. *Journal of Analytical Chemistry* **2016**, 71 (7), 730-736.
- [2] E. Fraunhofer, J. Cho, J. Yu, Z. Y. Al-Saigh, J. Kim, Adsorption of hydrocarbons commonly found in gasoline residues on household materials studied by inverse gas chromatography. *Journal of Chromatography A* **2019**, 1594, 149-159.
- [3] C. Wensel. The Effects of Household Substrates on the Evaporation of Ignitable Liquids at Temperatures up to 210 °C. [Master's Thesis]. Morgantown, WV: West Virginia University, 2020.
- [4] J.W. McIlroy, A.D. Jones, V.L. McGuffin, Gas chromatographic retention index as a basis for predicting evaporation rates of complex mixtures. *Analytica Chimica Acta* **2014**, 852, 257-266.
- [5] J.W. McIlroy, R. Waddell Smith, V.L. McGuffin, Fixed- and variable-temperature kinetic models to predict evaporation of petroleum distillates for fire debris applications. *Separations* **2018**, 5 (47), 1-19.
- [6] M.L. Hair, Hydroxyl groups on silica surface. *Journal of Non-Crystalline Solids* **1975**, 19, 299-309.
- [7] M. Joseph, Introduction to Textile Science, 5th Edition, Holt, Rinehart, and Winston, New York, NY, 1986.
- [8] S. Vahur, A. Teearu, P. Peets, L. Joosu, I. Leito, ATR-FT-IR spectral collection of conservation materials in the extended region of 4000 – 80 cm⁻¹. *Analytical and Bioanalytical Chemistry* **2016**, 408, 3373 – 3379.
- [9] D.A. Turner, J.V. Goodpaster, Comparing the effects of weathering and microbial degradation on gasoline using principal components analysis. *Journal of Forensic Sciences* **2012**, 57 (1), 64-69.
- [10] K.P. Gierszal, J.G. Davis, M.D. Hands, D.S. Wilcox, L.V. Slipchenko, D. Ben-Amotz, π -Hydrogen Bonding in Liquid Water. *Journal of Physical Chemistry* **2011**. 2 (22), 2390-2933.

V. Conclusions and Future Work

5.1 Conclusions

A kinetic model capable of predicting chromatograms of evaporated liquids was developed using diesel for environmental applications [1, 2]. The goal of the model was to guide remediation following a petroleum spill on an open body of water. Since the original development, the kinetic model has been applied for forensic fire debris applications, predicting chromatograms of common ignitable liquids evaporated to different levels [3, 4]. Because the model was developed with diesel, the predictive accuracy was good for other petroleum distillates. However, the model performed less well for gasoline, a very common ignitable liquid used to set intentional fires. Modifications had been made in the gas chromatographic (GC) and data analysis methods to improve the predictive accuracy for gasoline, especially for the more volatile compounds [4]. However, the model was extrapolated to I^T ranges over which it had not been developed.

The first aim in this work was to measure evaporation rate constants for highly volatile compounds with retention index (I^T) < 800. A set of volatile compounds were selected that varied in compound class and spanned an I^T range from 487 – 800, a range over which evaporation rate constants had not been previously measured. Experimental evaporations were performed as binary mixtures at 10, 20, and 30 °C and the rate constants combined with the previous kinetic model. The refined models were tested by predicting chromatograms of a validation mixture evaporated to several levels at each temperature. The refined model at 10 °C was tested at total fraction remaining levels (F_{Total}) of 0.54, 0.65, and 0.81, and exhibited Pearson product-moment correlation (PPMC) coefficients greater than 0.99 between the predicted and experimental chromatograms.

Although the model performed well at 10 °C, a correction for condensation in the measured evaporation rate constants was necessary. A method was established by which certain dishes contained only the solvent and the abundance of compounds in these dishes was used to quantify the vapor condensing back into the dishes. The corrected model at 10 °C was then used to predict the same chromatograms of the evaporated validation mixture, with PPMC coefficients either equal to or greater than the predictions using the uncorrected model.

Corrected models were also generated at 20 and 30 °C and tested using the validation mixture. Strong correlation was observed between the predicted and experimental chromatograms, with PPMC coefficients exceeded 0.95 for F_{Total} levels from 0.25 to 0.83. The corrected models at all three temperatures were then compared to the original fixed- and variable-temperature models to ensure that the predictive performance was either maintained or improved. In all cases, the PPMC coefficients were either similar or improved, validating the use of the extended model in predicting chromatograms of liquids containing more volatile compounds.

Following the refinement of the kinetic model for the more volatile compounds present in gasoline, a study was designed to investigate the effect of interface on the evaporation of hydrocarbons found in common ignitable liquids. Diesel was evaporated from four interfaces (glass dish, water, cotton fabric, and polyester fabric) and compounds from three homologous series (*n*-alkanes, alkylbenzenes, and alkyl cyclohexanes) with range $I^T = 800 - 1250$ were monitored. The evaporation rate constants for compounds in all three series were consistently the lowest from the glass dish, suggesting a chemical or physical difference in that specific interface that decreased the rate of evaporation from the substrate. The evaporation rate constants were similar for the remaining three interfaces. Of the two fabrics studied, polyester exhibited smaller

rate constants than cotton due to an increased adsorption of the hydrocarbons with this material. The evaporation rate constants for each homologous series were plotted *versus* I^T and linear regression was performed to develop models specific to each interface. When compared to the original class-specific models developed by McIlroy *et al.*, the slopes and intercepts did not vary greatly. Given these data, the original model works well for the substrates studied here and there is no need to have specific models for these interfaces. Therefore, adapting the model for the interfaces studied here does not seem necessary.

5.2 Future Work

The original model was refined to extend to lower I^T values and then tested using a validation mixture in the range $I^T = 500 - 800$ and compared to the original model. Future work should test the predictive accuracy of the refined model for liquids in different ASTM classes, such as gasoline and petroleum distillates. PPMC coefficients should be determined across the whole chromatogram, rather than just the volatile range to ensure that the refinement still allows for accurate prediction at higher I^T as well. These predictions can then be compared to those using the original model across the same I^T range to ensure that the accuracy is comparable or better.

The interfaces studied in this work involved two that had been previously investigated (water and a glass dish) as well as two fabrics (cotton and polyester). The latter interfaces were selected due to their prevalence in a common household and, therefore, their likelihood to be found at the scene of a potential intentional fire. Fabrics were also selected because of the efficiency with which a fuel could be extracted, thereby reducing the margin for error involved with inefficient extractions. However, many additional fabrics exist, such as nylon and silk, that have different surface chemistries and may be of interest with regards to evaporation. Additional

compound classes, such as naphthalene compounds, would also be of interest because the molecular interactions may be different due to the enhanced aromaticity. Eventually, substrates of higher complexity but more applicability should also be studied. Wood substrates are common household materials as well as carpet and carpet padding. A method to efficiently extract the fuel from these materials would be necessary to ensure that the evaporation rate constants measured are indicative of true evaporative differences and not extraction inefficiency.

While the direct measurement of evaporation rate constants for compounds from various interfaces is useful in determining the robustness of the model, it is challenging to attribute the differences observed to a specific characteristic of the surface. For example, there exist both physical and chemical characteristics that can contribute to the change in the kinetics of evaporation. For the fabrics studied, it was unclear whether the differences observed were due to the change in molecular interactions between compound and interface or due to the porosity and sorption characteristics. One way to differentiate these contributions would be to create surrogate substrates that mimic common household materials. The chemical characteristics could then be held constant while changing the porosity and vice versa. This would allow for the determination of the cause of the change in evaporation rate constant as a function of interface.

Finally, after the models have been refined for interface, validation studies should be performed that test the predictive accuracy of each model from actual substrates. For instance, the original model can be used to predict chromatograms corresponding to evaporated gasoline from a cotton fabric and compared to if the chromatogram was predicting using an interface-specific model.

REFERENCES

REFERENCES

- [1] J.W. McIlroy, A.D. Jones, V.L. McGuffin, Gas chromatographic retention index as a basis for predicting evaporation rates of complex mixtures. *Analytica Chimica Acta* **2014**, 852, 257-266.
- [2] J.W. McIlroy, R. Waddell Smith, V.L. McGuffin, Fixed- and variable-temperature kinetic models to predict evaporation of petroleum distillates for fire debris applications. *Separations* **2018**, 5 (47), 1-19.
- [3] R. Waddell Smith, R.J. Brehe, J.W. McIlroy, V.L. McGuffin, Mathematically modeling chromatograms of evaporated ignitable liquids for fire debris applications. *Forensic Chemistry* **2016**, 2, 37-45.
- [4] N.K. Eklund, B.A. Capistran, V.L. McGuffin, R.Waddell Smith, Improvements in a kinetic-based model to predict evaporation of gasoline. *Forensic Chemistry* **2020**, 17, 100194.